University of Alberta

Laser based acceleration of charged particles

by

Konstantin Popov

A thesis submitted to the Faculty of Graduate Studies and Research

in partial fulfillment of the requirements for the degree of

Doctor of Philosophy

in

Physics

Department of Physics

Fall 2009

Edmonton, Alberta

Examining Committee

W. Rozmus, Department of Physics, University of Alberta

R. D. Sydora, Department of Physics, University of Alberta

S. Morsink, Department of Physics, University of Alberta

R. Fedosejevs, Department of Electrical and Computer Engineering, University of Alberta

R. Marchand, Department of Physics, University of Alberta

A. B. Langdon, Lawrence Livermore National Laboratory

Abstract

In this Thesis, two problems were studied: a direct vacuum acceleration of electrons by a tightly focused ultrashort relativistic laser pulse and ion acceleration in the process of spherical laser-heated plasma explosion.

The electromagnetic field of a tightly focused laser pulse was evaluated numerically by means of Stratton-Chu integrals. The properties of the focused field were analyzed in detail for a plane wave or a macroscopically large Gaussian beam incident onto the mirror. Free electrons moving in the tightly focused field were found to accelerate by two possible mechanisms: focal spot acceleration and capture-and-acceleration scenario. The two mechanisms were studied in detail. Comparison of the mirror-focused field with first- and fifth-order paraxial fields is performed. A 3D electromagnetic PIC code SCPIC was created for simulations of pulse interaction with targets having a finite number of particles interacting with each other by collective fields. Atto-second bunch formation was observed in the interaction with ultra-small or ultra-thin targets. Physical mechanism of bunch formation is explained.

The problem of electrostatic explosion of a nano-scale spherical plasma with initially hot electrons and cold ions was solved numerically. Expansion in a wide regime of electron temperature $0 < T \leq \infty$ was studied in detail for different initial density profiles of plasma. Favorable conditions for obtaining mono-energetic ions resulting from the explosion were specified in single and two ionic species cases. In case of a two-species explosion, the number of mono-energetic, $\delta\varepsilon/\varepsilon < 10\%$, ions can be as high as 70-80% of the total light ions for a wide range of electron temperatures.

Acknowledgements

It is a great pleasure to thank my collaborator Valery Bychenkov who has been teaching, helping and advising me during the entire term of my PhD program. Without his inspiration and ideas, most part of this work would not appear. I am also thankful to D. Romanov for his comments on the SCPIC code. Special thanks to my supervisors W. Rozmus and R. Sydora for discussions and support and to the Department of Physics of University of Alberta for opportunity to work there.

Contents

Chapter 1

Introduction

Acceleration of charged particles by electromagnetic waves has been considered back in 1950's as a mechanism of energy gain in cosmic-ray particles [1]. Later, in the early 1970's, the first works have appeared [2] dealing with particle acceleration by laser beams under laboratory conditions. With the invention of chirped laser pulse amplification in 1985 [3] and subsequent progress in high-power lasers [4, 5, 6, 7, 8, 9], laser-based charged particle acceleration has become an independent subfield of plasma physics. The contemporary laser systems are capable of producing pulses with intensities of $10^{22}\,\mathrm{W/cm^2}$ in the best focus of the system [8]. For such intensities, matter is usually fully ionized already at the very beginning of the pulse, with most of the laser pulse interacting with the resulting plasma. The intensity of $10^{22}\,\mathrm{W/cm^2}$ corresponds to electric field $E \sim 5 \cdot 10^{14}\,\mathrm{V/m}$ (as compared to the present limit of $E \sim 10^{8}\,\mathrm{V/m}$ in the conventional charged particle accelerators). Efficient application of such huge fields is a problem yet to be solved. This Thesis aims at investigating the physical processes and effectiveness of two particular schemes of electron and ion acceleration working in the high laser intensity regime.

Besides the ultimate goal to accelerate charged particles to energies of interest for high energy physics, there exist other applications of accelerated particles. The fast laser-produced electrons are the key element in the concept of fast ignition in the inertial confinement thermonuclear fusion [10, 11] where the electron beam is supposed to play the role of a spark, igniting the fusion reaction. Another important application of fast electrons is generation of hard x-rays and γ-rays [12, 13] and a compact source of coherent x-ray radiation obtained in a free electron laser [14, 15]. There are also applications of lower-energy, MeV electrons, in waste and medical products sterilization [16, 17]. Energetic ions are needed in the controlled nuclear reactions such as isotope and neutron production [18, 19, 20, 21, 22, 23, 24, 25] as well as in plasma and matter diagnostics at extremely short times [26], material engineering [27] and aforementioned fast ignition with energetic ions [28, 29, 30, 31, 32]. Cheap high-quality fast ions would be ultimately useful in medicine, for tomography [33], which employs isotopes prepared by using the fast ions, and in proton therapy [34, 35, 36].

It was shown more than four decades ago [37] that a charged particle cannot be accelerated by a pulsed plane electromagnetic wave, although the particle can be shifted by a finite distance in space as a result of the interaction. Whereas the particle is accelerated at the leading edge of the pulse by the radiation pressure (more strictly speaking, by the positive longitudinal ponderomotive force which is anti-parallel to the gradient of intensity), it is decelerated by the negative longitudinal ponderomotive force at the pulse trailing edge. For this reason, one needs to employ more complicated techniques to transfer energy from the pulse to the particle.

Due to the large difference between electron and ion masses (m_p/m_e is at least 1836, for the case of proton, where m_e is electron mass and m_p is that of

proton), laser-based methods of their acceleration can be different. The most usually discussed methods for electron acceleration are inverse free electron-laser acceleration (IFEL), plasma wave acceleration, inverse Cherenkov effect, and direct vacuum acceleration. The principles of these methods are schematically shown in Fig. 1.1. In an IFEL accelerator [38, 39], the charged particle, co-propagating with the laser wave, moves in the external magnetic field produced by undulator magnets. For the proper magnitude and structure of the external magnetic field, the electron can be shown to acquire a nonzero energy from the laser. The principle of IFEL accelerator is depicted schematically in Fig. 1.1a.

The plasma wave acceleration [40], Fig. 1.1b, is one of most commonly discussed schemes in the literature. Historically, this scheme was first proposed in 1979 by Tajima and Dawson in a seminal paper [41]. The idea is to excite plasma waves by a laser pulse and use the resulting electric fields of charge separation in the wave to accelerate the particles. It was shown [40] that the plasma waves can remain linear while supporting very high fields ($E_{th} \sim \sqrt{n_e}$, where E_{th} is the wave-breaking electric field threshold in the plasma wave and n_e is electron density in plasma; for $n_e = 10^{18}\,\mathrm{cm}^{-3}$, $E_{th} \approx 100\,\mathrm{GV/m}$). Depending on the method of plasma wave excitation, there can be, among the most popular, plasma beat-wave or laser wake-field accelerators. In a plasma beat-wave accelerator [42, 43, 44], the plasma wave is excited by two laser pulses having frequency difference equal to the plasma frequency. The resulting laser beat wave can be shown to excite the plasma wave. The laser wake-field accelerator (also called plasma wake-field accelerator) [40, 45, 46] uses a laser with the pulse equal to or smaller than the plasma wavelength. For a relativistically strong laser pulse, the plasma wave can break [47] which eventually leads to self injection of electrons into the resulting bubble in the

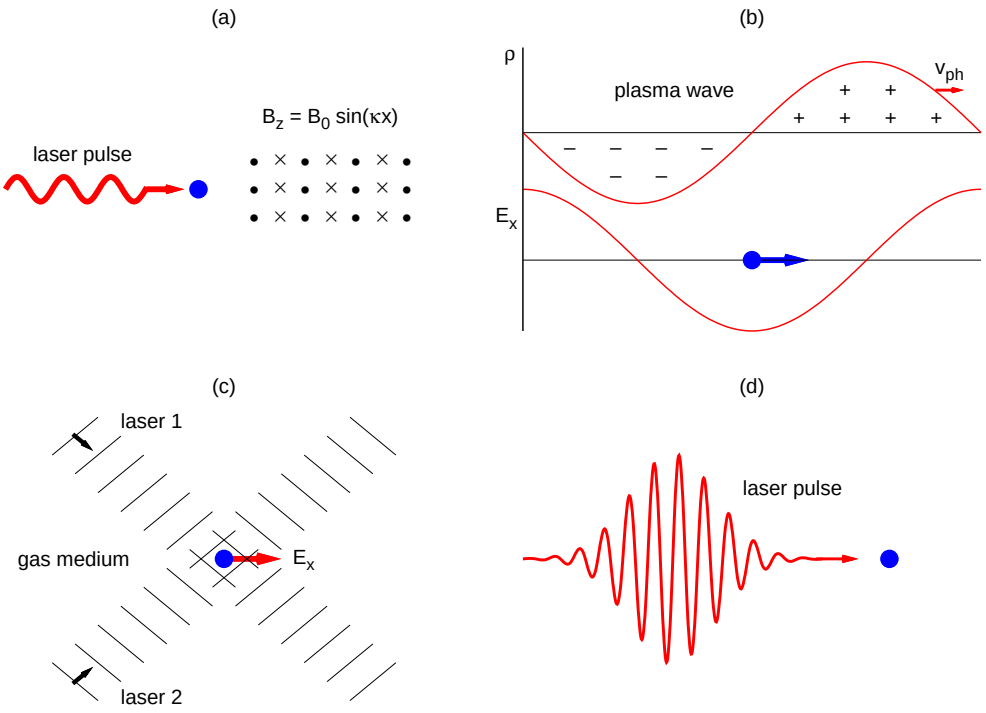

Figure 1.1: (Color) Some popular schemes of laser based electron acceleration: (a) IFEL accelerator, the net acceleration is provided by a proper choice of the external magnetic field; (b) plasma wave accelerator, electrons are accelerated by the electrostatic field of laser-induced plasma wave; (c) inverse Cherenkov accelerator, electrons are accelerated by the longitudinal field of the laser(s) slowed down by a gas medium; (d) direct vacuum acceleration, a laser pulse in vacuum interacts directly with the charged particle. An extraction mechanism is needed to acquire a nonzero energy.

plasma with the subsequent acceleration of the self-injected electrons to high energies [48, 49, 50]. Under some plasma conditions, the electrons possess the highly desirable mono-energeticity feature [51, 52, 53]. The results in Refs. [51, 52, 53] represent one of the major results in laser-based electron acceleration. Electron acceleration to GeV energies by the plasma wake accelerators was experimentally demonstrated recently [54].

The inverse Cherenkov accelerator [55, 56], Fig. 1.1c, depends on the subluminous phase velocity of the electromagnetic waves propagating in gases. This allows an injected ultra-relativistic electron to co-propagate with the pulse

at approximately the same field phase. The acceleration is provided by the longitudinal component of either two crossed quasi-planar laser beams (as in [55]) or by that of a focused laser (as in [56]). The idea of inverse Cherenkov accelerator was modified in [57] where plasma (rather than gas) was used to slow down the group velocity of the laser pulse and thus avoid the deceleration stage. The electrons in this scheme, upon reaching the maximum of the pulse, become energetic enough to overcome the laser pulse and thus do not appear in the region with negative ponderomotive force.

The direct vacuum acceleration, Fig. 1.1d, is popular for simplicity of its concept. The charged particles are supposed to accelerate in vacuum in the pure electromagnetic field of the laser beam. It is shown in Appendix A.1 that motion of a charged particle in a periodic plane electromagnetic wave consists of oscillatory motion in the transverse direction and a drift along the laser propagation. As was stated above, if the laser is pulsed, the particle, after acceleration while climbing the leading edge of the pulse, eventually decelerates at the pulse trailing edge. Certain particular schemes are proposed to extract the accelerated particle from the pulse and to avoid the deceleration stage. In papers [58, 59, 60, 61, 62, 63], the deceleration stage is avoided by natural inhomogeneities of focused laser pulses. The particles, accelerated by the laser field in the vicinity of focus, scatter from the large intensity region and thus can gain a nonzero net kinetic energy. Another extraction scheme deals with reflection of the laser pulse by a plasma mirror [64, 65]. The laser is reflected by plasma when the particle is in the middle of the pulse and has a high magnitude of energy oscillation. The ultra-relativistic electrons, in turn, normally can penetrate the overdense plasma by a distance on the order centimeters and thus are unaffected by the mirror. Injection of the particles into the middle of the pulse using, for example, field ionization of heavy atoms [66, 67] breaks the

symmetry of motion and was also shown to provide nonzero particle energy. A scheme of injection dealing with interplay between the electrostatic field of a partially evacuated target and the electromagnetic field of laser was discussed in [68]. In paper [69], usage of a metal screen with a hole in it was proposed to break the symmetry of motion. Some of the particle extraction schemes are shown schematically in Fig. 1.2.

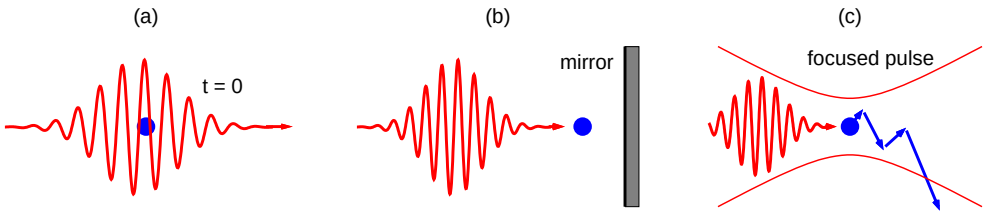

Figure 1.2: (Color) Particle extraction schemes in vacuum acceleration. (a) injection of a particle into the middle of the pulse; (b) reflection of the pulse by a mirror, particle continues moving through the mirror; (c) transverse scattering of a particle from a focused laser pulse.

Many direct vacuum acceleration schemes consider the extraction scheme dealing with particle scattering from a tightly focused laser beam. The tight focusing is needed to maximize the laser intensity in the vicinity of the laser focus and thus obtain large electromagnetic fields accelerating the particles. Whereas motion of charged particles in plane and quasi-planar electromagnetic waves is known, this is not the case for the regime of tight focusing. There are two main problems to be resolved in this context: (a) proper description of the field structure of a tightly focused beam and (b) calculation and optimization of particles motion in the resulting field. In this way, the most interesting case of direct vacuum acceleration dealing with the highest fields was not clear until recently. The case of tight focusing was clarified in the recent papers [63, 68], representing the original contribution of the author of this Thesis on the topic of direct vacuum acceleration.

A way to resolve the two problems of particle motion in a tightly focused laser beam is discussed in detail in Chapter 2 of this Thesis. The method employs an integral representation of the solutions of Maxwell equations with the given boundary conditions for the field description and numerical solution of the particle equations of motion. The two cases of particles moving in either pure electromagnetic field of the laser or in the self-consistent field of a plasma target interacting with the laser beams are considered. The methods and results discussed in Chapter 2 represent the conclusions of studies performed in Refs. [63, 68] as well as description of 3D relativistic electromagnetic particle-in-cell (PIC) code SCPIC developed for simulations of laser-plasma interactions and some new material to be published elsewhere.

Although it is possible, in principle, in most of the cases to use the same methods for ion acceleration as for electrons, in practice it is not usually done. Most of the proposed ion acceleration methods deal with partial evacuation of electrons from the target by the laser pulse, thus creating a charge separation electrostatic field which accelerates ions. Historically, the first studies of the dynamics of hot electron-driven plasma expansion into vacuum appeared in late 1960's [70], although at that time this phenomenon was discussed in the context of inertial confinement fusion (ICF). Laser-driven plasma expansion as a source of fast ions began to be discussed in the late 1970's [71, 72], mostly in planar geometry with semi-infinite plasma. During the last three decades, some optimizations of the ion acceleration by this scheme were proposed, such as using spherical geometry [73], multi-species ions [21, 74, 75], nonuniform initial plasma profiles [76, 77], and properly shaped [78] or multi-layered targets [79]. A typical process of the ion acceleration is depicted, for a case of spherical geometry of the plasma target, in Fig. 1.3. At a first stage of this process, the target is irradiated by the laser. Since the ions are heavy, they are almost

unaffected by the pulse. The light electrons, however, oscillate in the laser field with an amplitude comparable with, or, very often, exceeding, the size of the target. As a result, electrons tend to escape the target and thus an electrostatic field of the charge separation appears. This field slows down the electron expansion and, on the other hand, accelerates the ions in the radial direction.

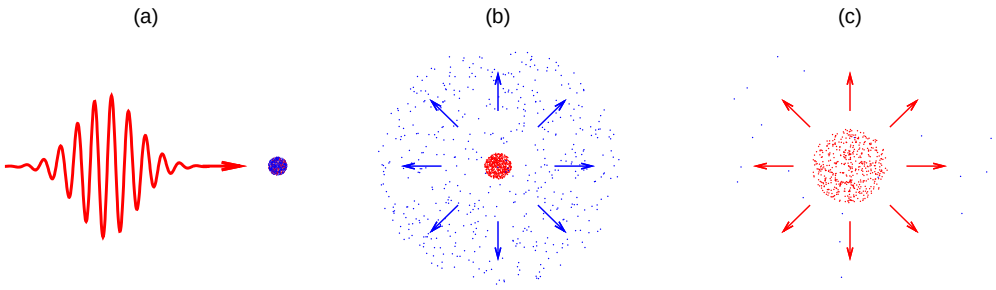

Figure 1.3: (Color) Acceleration of ions from a spherical target: (a) a laser pulse irradiates the target and heats it; (b) light hot electrons escape the target; (c) ions are accelerated in the field of the resulting unbalanced positive charge.

The details of absorption of laser energy by the target electrons are complicated (cf., for example, [80]). In many works the complicated physics of absorption is omitted altogether. Instead, an approximation is used in which the electrons are prescribed to have a certain distribution function at $t = 0$. In this way, only the problem of hot-electron driven expansion is studied. Depending on regime, the process of plasma expansion can be described in different ways. If the total kinetic energy of electrons considerably exceeds the total electrostatic energy of fully evacuated ions in plasma, such a regime is described using the model of Coulomb explosion (CE). In the CE model, the electron distribution function is assumed to be exactly zero. As a result, the problem of self-consistent motion of ions in the absence of electrons is solved. The limit of very small average kinetic energy of electrons is described with the

help of a quasi-neutral expansion model where the condition of quasi-neutrality is used to avoid the solution of Poisson's equation. Only few studies are dedicated to the description of plasma expansion in the intermediate regime of moderate electron average kinetic energy. This is especially the case for more than one ionic species present. The latter case is of particular interest since it can be shown to result in mono-energetic spectra of one of the ionic species comprising the expanding plasma.

In Chapter 3 of this Thesis, the hot-electron driven expansion of multi-species, nonuniform plasma is discussed. The electrons are assumed to have a Maxwellian velocity distribution at $t = 0$, characterized by a certain temperature. The multi-species plasma composition can be "homogeneous" (concentration of light ions does not depend on radius) or "heterogeneous" (the light ions form a shell around the heavy core). A major part of Chapter 3 represents the results of the author's contribution to the topic of plasma expansion published in papers [77, 81, 82]. These results include: the particular dynamics of double collisionless shocks in the CE of inhomogeneous spherical targets, dynamics of single-species homogeneous and inhomogeneous spherical targets in the intermediate electron energy regime, dynamics of two-species expansion of spherical plasma targets in the CE and intermediate electron energy regimes. The results were obtained using a gridless particle simulation code developed for modeling of 1D spherical plasma expansion incorporating multi-ion species.

The outline of this Thesis is as follows. In Chapter 2, acceleration of electrons by a tightly focused laser pulse is studied. In the Section 2.1, the history of the subject and the basic physical concepts of direct vacuum acceleration are presented in detail. The main problems of vacuum electron acceleration are posed. Among these problems is the correct field description which is an

important issue, especially for a tight laser focus. Section 2.2 describes the particular method of field evaluation which is used in this research. Section 2.3 presents results of numerical solution of the equations of motion for single charged particles moving in the tightly focused laser. To understand the motion of electrons in the self-consistent field, which includes also fields of the surrounding charges, one needs to solve the Vlasov equation for plasma evolution. Section 2.4 presents the 3D relativistic electromagnetic PIC code SCPIC created by the author of this Thesis. This code numerically solves the equations of a finite number of characteristics of the Vlasov equation for collisionless plasma and thus gives a numerical approximation to the solution of the Vlasov equation. The equations of motion are solved in the self-consistent electromagnetic field, being the sum of external and plasma-generated fields. The corresponding results are given in Section 2.5. Section 2.6 concludes the discussion of direct vacuum electron acceleration.

Hot-electron driven acceleration of ions from the laser-heated exploding spherical plasma targets is discussed in the Chapter 3. The detailed historical introduction and formulation of the problems to be solved are given in Section 3.1. The physical model and simulation tools used in the analysis are given in Section 3.2. The explosion of a single-species nonuniform plasma target, in two different regimes, CE and thermal explosion (TE) is discussed in Sections 3.3 and 3.4, correspondingly. The explosion of multi-species targets, both homogeneous or multi-layered, is discussed in Section 3.5. Section 3.6 presents discussion of the obtained results and conclusions.

Chapter 2

Vacuum electron acceleration by a tightly focused laser

2.1 Basic physical concepts of direct vacuum acceleration

2.1.1 Charged particle in electromagnetic field. Plane wave solution

To find the motion of a single charged particle in an external electromagnetic field $\vec{E}$, $\vec{B}$, one has to solve the Lorentz-Newton equations of motion

$$\begin{aligned} \frac{\mathrm{d}(\gamma m\vec{v})}{\mathrm{d}t} &= q(\vec{E} + \frac{\vec{v}}{c} \times \vec{B}), \\ \frac{\mathrm{d}\vec{r}}{\mathrm{d}t} &= \vec{v}, \end{aligned} \tag{2.1}$$

where m and q are, correspondingly, mass and charge of the particle, $\vec{r}$ and $\vec{v}$ are its position and velocity, $\gamma = 1/\sqrt{1 - \vec{v}^2/c^2}$, c is the speed of light and t is time in the laboratory frame. Due to nonlinearity on both sides of the first

equation of (2.1), where $\vec{E}$, $\vec{B}$ are, generally, nonlinear functions of coordinates $\vec{r}(t)$, the system (2.1) is exactly integrable only in very few cases. One of such cases is a plane electromagnetic wave:

$$\vec{E} = \vec{E}(kx - \omega t),\ \vec{B} = \vec{B}(kx - \omega t), \tag{2.2}$$

where x is coordinate along the wave propagation direction (longitudinal coordinate) and $k = \omega/c$, ω is the laser frequency. It is a well-know result that plane electromagnetic waves are necessarily transverse since having nonzero longitudinal components for the field depending only on the longitudinal coordinate would immediately make $\nabla \cdot \vec{E} = \partial E_x/\partial x \neq 0$.

For a plane wave, the equation of motion (2.1) was solved for relativistic case in late 1960's [37, 83, 84]. A solution for the case of plane polarized harmonic plane wave:

$$\vec{E} = E_0 \hat{e}_y \cos(kx - \omega t),\ \vec{B} = E_0 \hat{e}_z \cos(kx - \omega t), \tag{2.3}$$

where E_0 is the wave amplitude, and $\hat{e}_y$, $\hat{e}_z$ are unity vectors along the corresponding transverse axes, is given in Appendix A.1. The plane wave possesses a number of important symmetries which allow one to reduce the dimensionality of the system, and to solve the equations of motion of a charged particle exactly. If the particle starts at rest, and the laser pulse which has a finite length, starts from minus infinity, then a particle, upon pulse arrival, will perform oscillatory motion, with its relativistic factor γ oscillating between zero and

$$\gamma_{max} = 1 + \frac{a_{max}^2}{2}, \tag{2.4}$$

where the dimensionless field amplitude a at the particle position is $a =$

$qE_0/m\omega c$, with q, E_0, m, ω and c expressed in CGS units. A similar dependence (although with a different coefficient before a^2) holds for circular and elliptic polarizations. If the particle had a nonzero kinetic energy before the pulse has started interacting with it, its γ-factor can be shown to oscillate between γ_0, $t \to -\infty$ value, and

$$\gamma_{max} = \gamma_0 \left(1 + \frac{a_{max}^2}{2}\right), \tag{2.5}$$

The quadratic dependence between the magnitude of the field and amplitude of particle kinetic energy oscillations can result in very large particle energy for $a \gg 1$. Thus, the intensity of $10^{22}\,\mathrm{W/cm^2}$, discussed above, for which $a \approx 85$ in the case $\lambda = 1\,\mu m$, can produce up to 1.8 GeV electrons, according to Eq. (2.4).

Unfortunately, this value is only an amplitude of energy oscillations while the particle co-propagates with the laser pulse. When particle climbs the pulse, i.e., interacts with its leading edge, the amplitude of the field oscillation at the particle position increases with time and so does the amplitude of particle energy oscillations. Since the pulse is finite and the particle velocity is always smaller than c, the pulse will eventually overtake it. This results in $a = 0$ at $t \to +\infty$ at the particle position and zero amplitude of energy oscillations of the particle. In this way, interaction between the particle and a laser pulse leads only to the overall displacement of the particle in space. This is demonstrated in Fig. 2.1, where the trajectory and evolution of particle γ-factor are shown for $a_{max} = 1$ and a finite-duration pulse having wave envelope described by

$$a(x,t) = a_{max} \exp\Big(- \big(\frac{t - x/c - T_0}{\Delta T}\big)^2 \Big), \tag{2.6}$$

where T_0 is the envelope displacement (relative to $t = 0$) and ΔT its length.

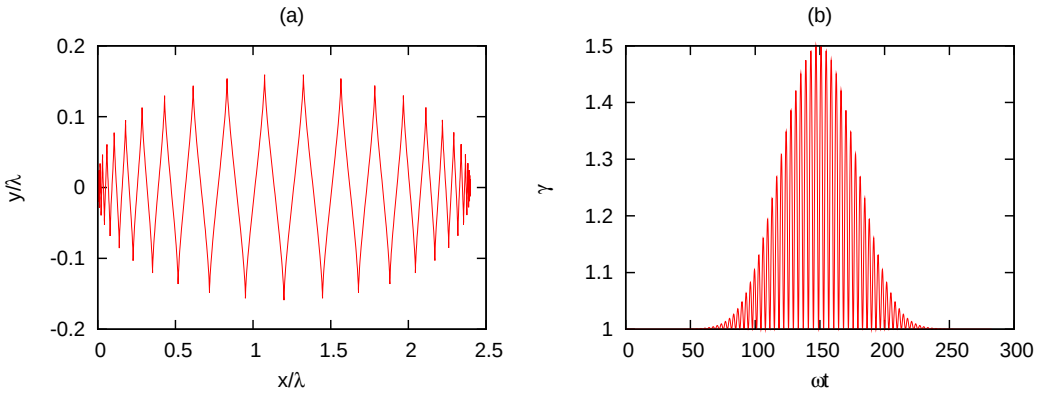

Figure 2.1: Electron trajectory (a) and γ-factor evolution (b) in interaction with a finite-duration plane polarized plane electromagnetic wave with $a_{max} = 1$. Results of computer integration of Eq. (2.1).

Usually the pulse length is defined not directly by ΔT but by a more general parameter called Full Width at intensity Half-Maximum (FWHM). For the Gaussian envelope given by (2.6), FWHM $= \Delta T \cdot \sqrt{2 \ln 2}$.

Summarizing the properties of charged particle motion in a plane electromagnetic wave, one can conclude that: (a) there is a quadratic dependence between the amplitude of the field and amplitude of particle kinetic energy oscillations; 2) the net energy acquired by the particle is zero. The inability of a pulsed plane wave to provide net acceleration of a charged particle was realized long ago [37]. This property of interaction poses the problem of particle extraction, i.e., a method of avoiding the deceleration stage at the trailing edge of the pulse.

2.1.2 Lawson-Woodward theorem

The inability of the particle to acquire net energy after interaction with a planar-like electromagnetic wave is the statement of the so-called Lawson-Woodward (LW) theorem[1] [64]. Given the known controversies in understand-

[1] As follows from the discussion below, a more appropriate name is "Lawson-Woodward principle" rather than the "theorem".

ing of this theorem [85, 86] its formulation and proof are given here. The proof is taken from work of Palmer [87].

Theorem 1 (Lawson-Woodward theorem)**.** *Consider a charge q moving in an electromagnetic field at a velocity v. Let the distance over which the field phase at the particle position changes by 2π be called phase slippage distance. If*

1. *Charge radiation reaction is negligible*
2. *Particle is ultra-relativistic ($v \approx c$)*
3. *There are no other free charges near the interaction region*
4. *There are no static fields*
5. *Particle is moving in free space*
6. *Distance from field source is large compared to the wavelength*
7. *The characteristic distance of the field amplitude change is large compared to the phase slippage distance of the particle*

then the net energy gain $\int_{-\infty}^{+\infty} qE_r dr = 0$, where $\hat{r}$ is the particle direction of motion.

Proof (Palmer's). Denoting angle between $\vec{k}$ and $\hat{r}$ as θ, and choosing the origin of time such that the particle position $r = vt \approx ct$,

$$\begin{aligned} &\int_{-\infty}^{+\infty} qE_r \mathrm{d}r = \int_{-\infty}^{+\infty} qE_{r0} \cos(k_r r - \omega t) \mathrm{d}r \approx \\ &c \int_{-\infty}^{+\infty} qE_{r0} \cos[k_r ct - \omega t] \mathrm{d}t = \\ &c \int_{-\infty}^{+\infty} qE_{r0} \cos[\omega t(\cos\theta - 1)] \mathrm{d}t \approx \\ &qcE_{r0} \int_{-\infty}^{+\infty} \cos[\omega t(\cos\theta - 1)] \mathrm{d}t = 0, \ \forall\, \theta \neq 0. \end{aligned} \tag{2.7}$$

If $\theta = 0$ then $\vec{k} \| \hat{r}$, and $E_{r0} = 0$ thus again resulting in a zero net energy gain. □

The Palmer's proof of the theorem needs some clarifications. First of all, the seventh condition, concerning the phase slippage distance, is not specified in [87], but since this condition is used at the last step in Eq. (2.7), where E_{r0} is taken out of the integral over time, it should be present in the formulation. This condition in fact is recognized in [64] where it is formulated as "the ponderomotive effects are neglected". Generally speaking, the last step in Eq. (2.7) is exactly valid only in the case of a constant amplitude wave. If the wave amplitude A is not exactly constant but changes slowly then

$$\int_{-\infty}^{+\infty} A \cos[\omega_1 t] \mathrm{d}t \approx \sum_{n=-\infty}^{+\infty} \int_{2\pi(n-1)/\omega_1}^{2\pi n/\omega_1} A_n \cos[\omega_1 t] \mathrm{d}t, \tag{2.8}$$

where $\omega_1 = \omega(\cos\theta - 1)$ and $A = qcE_{r0}$. A_n in Eq. (2.8) is the approximation to the value of A between $t = 2\pi(n-1)/\omega_1$ and $t = 2\pi n/\omega_1$ which, by the seventh condition of the theorem, can be approximated by a constant. Thus,

$$\sum_{n=-\infty}^{+\infty} \int_{2\pi(n-1)/\omega_1}^{2\pi n/\omega_1} A_n \cos[\omega_1 t] \mathrm{d}t = \sum_{n=-\infty}^{+\infty} A_n \int_{2\pi(n-1)/\omega_1}^{2\pi n/\omega_1} \cos[\omega_1 t] \mathrm{d}t = 0. \tag{2.9}$$

In principle, the presented proof is applicable also if the wave can be decomposed into a sum of plane waves. However, the amplitude of each of the components should change slowly at the distance of the phase slippage. This condition may be not satisfied, for example, in a case of a radially diverging source.

There is a subtle point that needs to be taken into consideration. In Eq. (2.7), θ is supposed to be a constant. However, interaction with an electromagnetic wave should obviously change this value. In this way, the energy,

which the particle gains during one laser cycle, should be small compared to the average kinetic energy of the particle during this cycle (cf. condition 2 of the theorem).

The LW theorem, as follows from its formulation, is applied to the case of a relativistic particle injected into the laser pulse. Such a particle cannot gain energy from the pulse. The validity of the theorem was illustrated experimentally in [88] where it was demonstrated that the moving beam of electrons did not change its energy distribution after the interaction with a laser pulse unless a plasma wall reflecting the pulse was introduced. In [88], the kinetic energy of electrons in the injection beam was equal to 30 MeV while the laser had ~ 0.5 mJ in a 4ps pulse focused into $\sim 10^2$ wavelengths which could possibly change the energy of electrons by a value of order keV's (when the reflecting wall is introduced). In other words, all the conditions of the LW theorem were met.

2.1.3 Non-zero energy gain

If the conditions of the LW theorem are violated, there can be a finite energy gain. An example of such gain was reported in the experimental work by Malka et. all [89]. In [89], keV electrons have gained energy of order 1 MeV upon crossing the laser having intensity $\approx 10^{19}\,\mathrm{W/cm^2}$ focused into a spot having $10\,\mu$m in diameter. The laser wavelength was $1\,\mu$m and its length $\approx 0.5\,$ps. Although the theoretical analysis in [89] has caused some criticism [90], the experimental result reported in [89] is an important example of a large energy gain in a vacuum acceleration scheme working in a regime when the conditions of LW theorem are violated.

Another example of LW theorem violation is the case discussed above when the laser pulse is reflected by a plasma mirror.

The LW theorem guarantees that there is no energy gain provided assumptions (1) – (7) from p. 15 are met. However, if they are violated, there is no guarantee of energy gain. A typical example is the case discussed in the beginning of this section: interaction between a particle, motionless at $t \to -\infty$, and a plane pulse. Although the second condition of the theorem is violated, the particle is just displaced in the space. This is caused by the properties of charged particle dynamics in a plane electromagnetic wave. As derived in Appendix A.1, in this interaction the transverse canonical momentum of the particle is conserved:

$$\frac{\mathrm{d}}{\mathrm{d}t}\left(\vec{p}+\frac{q}{c}\vec{A}\right)_{\perp}=0, \tag{2.10}$$

where $\vec{A}$ is the vector potential of the laser field and $\vec{p}$ particle momentum. Since the transverse and longitudinal motions of the particle are coupled through

$$\frac{\mathrm{d}}{\mathrm{d}t}\Big(\gamma(1-\frac{v_x}{c})\Big)=0 \tag{2.11}$$

(Eq. (A.24)), this leads to a zero energy gain of the particle if the values of $A_\perp$ are the same at $t \to -\infty$ and $t \to \infty$. For a finite pulse, $A_\perp(-\infty) = A_\perp(\infty) = 0$, and thus the net kinetic energy gain of the particle is zero.

If a particle is injected into the middle of the pulse at $t = 0$, its energy gain is defined by the difference $A_\perp(0) - A_\perp(-\infty)$ and thus depends on the field phase at the injection point at $t = 0$. Since $\vec{E} = -\frac{1}{c}\frac{\partial \vec{A}}{\partial t}$, maximum of $A_\perp$ corresponds to a zero field. In this way, if the transverse electric field is defined as $E_\perp \sim \cos(kx - \omega t + \varphi_0)$, the maximum energy gain of the particle corresponds to $\varphi_0 = \pi/2$. This conclusion is demonstrated in Fig. 2.2. If the field phase at the injection point in the middle of the pulse is zero, the net energy gain is zero. For a nonzero phase, there is a nonzero gain. For $\varphi_0 = \pi/2$, injection into the phase when field is zero, the energy gain corresponds to

$\gamma_{final} = \gamma_0(1 + a^2/2)$ for the plane polarization.

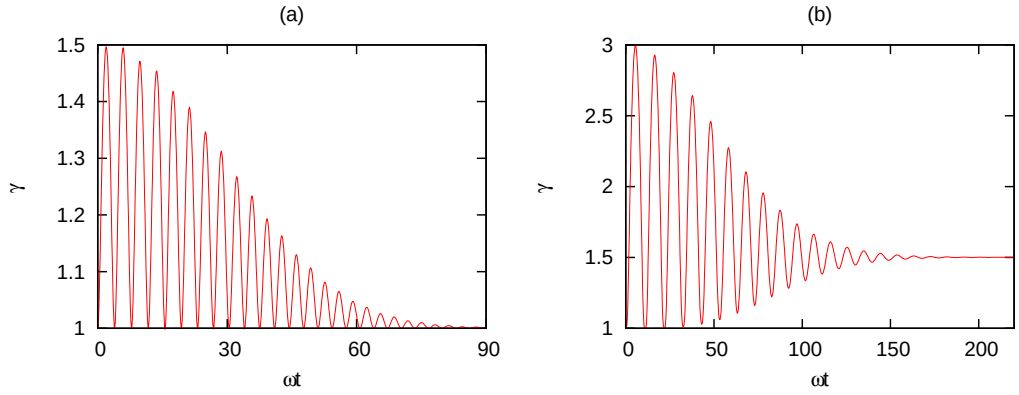

Figure 2.2: γ-factor evolution of a particle injected into the middle of a plane laser pulse: (a) injection with $\varphi = 0$, maximum field value; (b) injection with $\varphi = \pi/2$, zero field value. $a_{max} = 1$. Results of computer simulations.

An injection mechanism into the middle of the pulse can be provided by field ionization [66] or by interplay between the electrostatic field of a partially evacuated nano-scale target and the laser field [68].

2.1.4 Ponderomotive force

The plane wave solution to the Maxwell equations is an idealized field representation that is rarely the case in practice. To increase the intensity of the field, the laser is usually focused.

The transverse size of the laser beam upon leaving the optical system can be as large as tens of centimeters. After focusing, the size usually becomes not more than a few tens of microns. For a tightly focused beam, the size of the laser spot in the focal plane can be as small as one laser wavelength, i.e., on the order one micron. This allows one to increase the intensity by many orders of magnitude. As a result, the structure of electromagnetic field is more complicated than that of a plane wave. This brings in distortions of the particle trajectory that violate the symmetry of motion and could result

in nonzero energy gain of the particle.

The physical mechanism which actually breaks the symmetry of motion is associated with the ponderomotive force [91] of the focused beam. The ponderomotive force pushes the charged particles from the regions of high intensity to the regions of a lower intensity. The particle performs fast oscillations in the laser field but slowly drifts in the direction opposite to the intensity gradient. The simplest description of ponderomotive force can be given in the nonrelativistic limit for which the force acting onto the particle is caused almost entirely by the electric field component. Suppose that a particle has started its oscillation cycle anti-parallel to the intensity gradient. After an accelerating semi-cycle the particle is displaced into the region of a smaller field. At the beginning of the decelerating semi-cycle, the particle is still moving outward of the high intensity region and thus the returning force felt by the particle during the decelerating semi-cycle is smaller than the accelerating force during the accelerating semi-cycle. If the field decreases too fast, the particle may even be unable to stop at all. In the case of a slower decrease of the field amplitude with distance, the returning points, and thus the average particle position, drift with time towards the smaller intensity. The drift of the particle can be described by a force, called ponderomotive force, acting onto the guiding center of the particle defined as the oscillation-averaged position of the particle. A more quantitative discussion of ponderomotive force is given in Appendix A.2. The value of the force is defined in the nonrelativistic case as

$$\vec{F}_p = -\frac{q^2}{2m\omega^2}\nabla\left\langle \vec{E}^2 \right\rangle, \tag{2.12}$$

where the angle brackets denote averaging over one laser cycle. The relativistic modification contains also the cycle-averaged γ-factor of the particle in the

denominator [60, 92].

The ponderomotive force given by Eq. (2.12) gives a good approximation to the average force acting on electron provided the intensity inhomogeneity scale length is much larger than the particle quiver amplitude. The last condition usually requires moderate focusing, especially for relativistic intensities ($a \gg 1$). It was shown in a number of works [59, 60, 64] that the mechanism, called ponderomotive acceleration, indeed, provides net acceleration of the particles. The particles drift away from the high intensity due to the ponderomotive force and eventually scatter when the decelerating field is unable to stop the particle. This process is illustrated in Fig. 2.3 where an electron has acquired a final energy in vacuum from a focused pulse. The particle escapes the focal

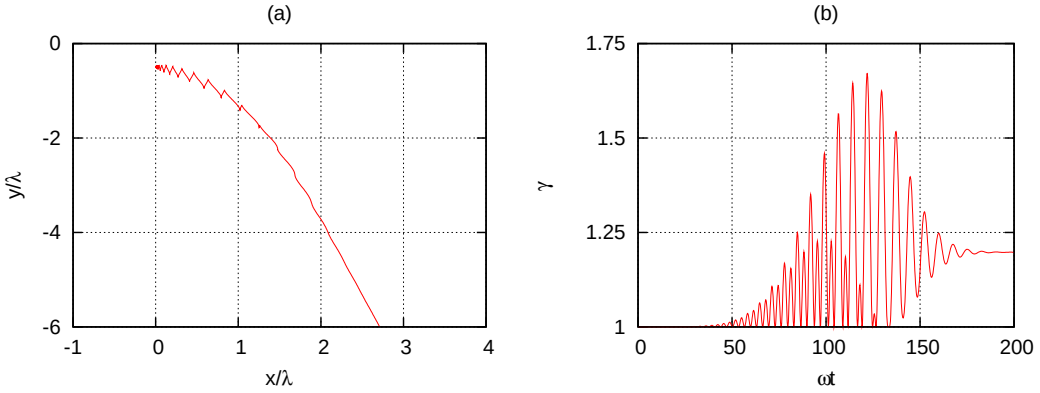

Figure 2.3: Electron trajectory (a) and γ-factor evolution (b) in interaction with a finite-duration plane polarized pulse with $a_{max} = 1$ focused into a spot having radius $w_0 = 3\,\lambda$ with the best focus at the origin. Results of computer simulations. The fields used in simulations are described in a first order paraxial equation, given by Eq. (2.22) below in Sec. 2.2.

spot and moves with some large angle with respect to the laser propagation direction. The angle depends on the field amplitude, pulse length, focal spot size and initial position of the particle relative to the best focus. The energy, obtained by the particle, is a fraction of the value given by Eq. (2.4) with a_{max} evaluated at the best focus, since in fact the net acceleration of the particle is

provided by the small field at the periphery of the focal spot. In this way, one can hope that a more tight focusing can provide a higher escape energy.

In the focused laser, not only the intensity profile is inhomogeneous, but also additional non-zero laser field components appear. Whereas the plane wave has only transverse field components, the focused pulse also has longitudinal components. This can be seen from, for example, the equation $\nabla \cdot \vec{E} = \partial E_x/\partial x + \partial E_y/\partial y = 0$, where y is a transverse component of the laser. If the intensity distribution in the focus is inhomogeneous, so is the distribution of the field and thus $\partial E_y/\partial y \neq 0$. Therefore, $\partial E_x/\partial x \neq 0$ and the longitudinal component E_x is, generally, nonzero (see also [93]). The existence of longitudinal component of the field affects the particle dynamics and under certain conditions can lead to a considerably smaller, than in the case of only transverse component presenting, scattering angle of the particle [94]. In Refs. [61, 95], it was proposed to use a ring-like intensity profile in the vicinity of the laser focus confining the particles which would not escape the ponderomotive potential formed around the laser axis. The particles are accelerated in this scheme by the longitudinal field component of the focused laser. The motion of the charged particles in the tightly focused laser, where the additional field components are large, is so complicated that a detailed understanding of this motion is still needed. In this Thesis, we will analyze the dynamics of the particles in the field of a tightly focused laser. The first task to achieve this goal is the correct description of the field of a tightly focused laser.

2.2 A tightly focused laser beam

In the majority of studies of the particle dynamics in focused fields [59, 61, 62, 64, 67, 69, 94, 96, 97, 98, 99, 100], a paraxial approximation with Gaussian

beam solution is employed. The paraxial approximation deals, in principle, with small focusing angles.

The derivation of the electromagnetic field of a focused laser in paraxial approximation as an expansion over a small parameter, related to the ratio between the laser wavelength and the focal spot size, can be found in the classical paper by Davis [101]. The idea is as follows. Let $\vec{A}$ be the Fourier transformation of the vector potential of the laser field in vacuum. $\vec{A}$ must satisfy Helmholtz equation

$$\nabla^2 \vec{A} + k^2 \vec{A} = 0, \tag{2.13}$$

where k is the wave vector length. In the crudest approximation, $A_x = A_z = 0$, and the only nonzero component is A_y. For the nearly plane wave, A_y is supposed to be a product of two functions:

$$A_y(\vec{r}) = \Psi(\vec{r}) \cdot e^{ikx}, \tag{2.14}$$

where $\Psi(\vec{r})$ is a slowly varying function of coordinates $\vec{r}$, i is the imaginary unit and x is the longitudinal coordinate. Substituting Eq. (2.14) into (2.13), one can obtain the equation for the slowly varying part of A_y:

$$\nabla^2 \Psi - 2ik \frac{\partial \Psi}{\partial x} = 0. \tag{2.15}$$

The paraxial approximation deals with low beam divergence and thus the derivatives along beam propagation x are considered much smaller than those perpendicular to it. In the first approximation, the derivative $\partial^2/\partial x^2$ is dis-

carded in (2.15), and the following paraxial equation is solved:

$$\nabla_{\perp}^2 \Psi - 2ik\frac{\partial \Psi}{\partial x} = 0. \tag{2.16}$$

It can be shown [102] that equation (2.16) has a solution

$$\Psi_0(\vec{r}) = \exp\big[C(x) - \frac{r^2}{2D(x)}\big], \tag{2.17}$$

where $r^2 = y^2 + z^2$ and

$$\begin{aligned} C(x) &= -\ln\sqrt{1 + \big(\frac{x - x_0}{kD_0}\big)} - i\arctan\big(\frac{x - x_0}{kD_0}\big) + \text{constant}, \\ D(x) &= D_0 + i\frac{x - x_0}{k}, \end{aligned} \tag{2.18}$$

with D_0 and x_0 being some constants. Eq. (2.17) is a special case of a more general set of solutions expressed as Gauss-Hermite modes [103]:

$$\begin{aligned} \psi_{0mn}(x) = \frac{1}{w(x)} H_m\big(\frac{\sqrt{2}z}{w(x)}\big) H_n\big(\frac{\sqrt{2}y}{w(x)}\big) \cdot \\ \exp\big[i\Phi(x) + ik\frac{r^2}{2R(x)} - \frac{r^2}{w^2(x)}\big], \end{aligned} \tag{2.19}$$

where

$$\begin{aligned} w^2(x) &= 2D_0\big[1 + \frac{(x - x_0)^2}{D_0^2 k^2}\big], \\ R(x) &= (x - x_0)\big[1 + \frac{k^2 D_0^2}{(x - x_0)^2}\big], \end{aligned} \tag{2.20}$$

and

$$H_n(x) = (-1)^n e^{x^2/2}\frac{\mathrm{d}^n}{\mathrm{d}x^n}e^{-x^2/2} \tag{2.21}$$

are Hermite polynomials.

In a finer approximation, $\partial^2/\partial x^2$ is not discarded in (2.15) but the solution to Eq. (2.15) is sought as an expansion over the small parameter $\epsilon = 2/kw_0$,

where w_0 is the radius of the focal spot. If only first-order terms are preserved in this expansion, the solution to (2.15) can be shown to have the form resulting in [60]:

$$\begin{aligned} E_x &= E_0\epsilon\frac{yw_0}{w^2}\exp\Big(-\frac{r^2}{w^2}\Big)\cos(\phi_G^{(1)}),\\ B_x &= E_0\epsilon\frac{zw_0}{w^2}\exp\Big(-\frac{r^2}{w^2}\Big)\cos(\phi_G^{(1)}),\\ E_y &= B_z = E_0\frac{w_0}{w}\exp\Big(-\frac{r^2}{w^2}\Big)\sin(\phi_G),\\ E_z &= B_y = 0, \end{aligned} \tag{2.22}$$

where E_0 is the field amplitude in the best focus, $\phi_G = wt+kx+\arctan(x/x_R)-xr^2/x_Rw^2+\psi_0$, $\phi_G^{(1)} = \phi_G + \arctan(x/x_R)$, $x_R = kw_0^2/2$ is the Rayleigh length and $w = w_0\sqrt{1+x^2/x_R^2}$.

Although the equation (2.15) is exact, the Eq. (2.22) is only its approximate solution which is, obviously, incorrect for $\epsilon \sim 1$, i.e., in the case of a tight focusing. Even the higher-order approximations, that are employed in [62], [67] and [100], do not, in principle, solve this problem.

There is another method of evaluating the laser fields, called the angular spectrum representation method. This method was employed in a number of studies [58, 60, 104, 105]. The field calculated by the angular spectrum representation method has a form of inverse Fourier integrals over sum of plane and evanescent waves satisfying boundary conditions in a certain plane, for example, in the focal plane. The result is further used in numerical solvers. The common problem with this method deals with, generally, unknown fields or vector potential in the plane where the boundary conditions have to be evaluated. This field should be guessed and thus the result, although being a solution to the wave equation, is still an approximation.

In this Thesis, a method of direct integration of the fields emitted by the surface of an optical element will be employed. This method was previously

discussed in [106], [107] and [108], and, in the context of particle acceleration, in [63, 68]. The method uses the following model.

Let a plane or a quasi-plane wave propagating in the $-\hat{x}$ direction hit a surface of ideally reflecting parabolic focusing mirror of radius r_m and focal length f_0 having optical axis in the $+\hat{x}$ direction (see Fig. 2.4). The quantities r_m and f_0 are supposed to be macroscopic, i.e.,

$$\begin{aligned} r_m &\gg \lambda, \\ f_0 &\gg \lambda, \end{aligned} \tag{2.23}$$

where λ is the laser wavelength. In this way, the mirror is characterized by its f-number

$$f_\# = \frac{f_0}{2r_m}. \tag{2.24}$$

The tight focusing regime corresponds to $f_\# \sim 1$.

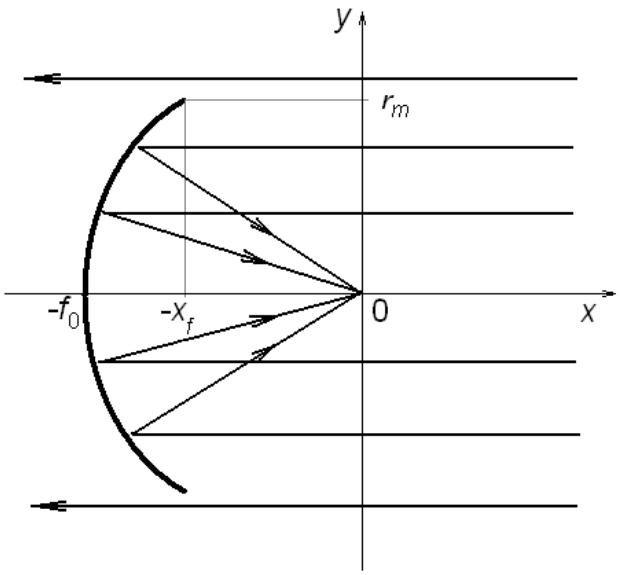

Figure 2.4: Scheme of the laser focusing model.

The fields of the electromagnetic wave incident onto the surface of the

mirror are given by

$$\begin{aligned}\vec{E}_{inc} &= \Re\Big\{\Big(0,\ E,\ 0\Big)e^{-i(kx+\omega t+\psi_0)}\Big\},\\ \vec{B}_{inc} &= \Re\Big\{\Big(0,\ 0,\ -E\Big)e^{-i(kx+\omega t+\psi_0)}\Big\},\end{aligned} \tag{2.25}$$

where $\Re$ sign stands for the real part, E is, generally, a slow function of transverse coordinates y and z changing on the scale of mirror radius r_m, and ψ_0 is the laser phase. As E changes only on macroscopic scale, the quasi-plane wave (2.25) is, with a good accuracy, transverse. The fields of the light reflected from the mirror are, in fact, those seen by the accelerated particles. These fields are calculated with the help of Stratton-Chu integrals.

The Stratton-Chu integrals, appeared first in the original paper [109] (although they were not called the Stratton-Chu integrals there), are an integral representation of electromagnetic field emitted by any closed surface, observed at any point inside the surface volume. The integrals are taken over the emitting surface and are the solution to Maxwell equations provided the source fields are a solution to Maxwell's equations. In general, the Stratton-Chu integrals can be used even if the tangential component of the emitting field suffers a discontinuity at the surface. The derivation of Stratton-Chu integrals, for the case of continuous field source at the surface, is given in Appendix A.3. The Stratton-Chu integrals for this case are

$$\begin{aligned}\vec{E}(\vec{r}_0) &= \frac{1}{4\pi}\oint_A [ik(\vec{n}\times\vec{B}_s)\psi + (\vec{n}\times\vec{E}_s)\times\nabla\psi + (\vec{n}\cdot\vec{E}_s)\nabla\psi]\,\mathrm{d}S,\\ \vec{B}(\vec{r}_0) &= \frac{1}{4\pi}\oint_A [ik(\vec{E}_s\times\vec{n})\psi + (\vec{n}\times\vec{B}_s)\times\nabla\psi + (\vec{n}\cdot\vec{B}_s)\nabla\psi]\,\mathrm{d}S,\end{aligned} \tag{2.26}$$

where $\vec{E}_s$ and $\vec{B}_s$ are field values on the surface A, $\vec{n}$ is the inner normal to the surface A and $\psi = e^{iku}/u$, $u = |\vec{r}_s - \vec{r}_0|$, $\vec{r}_s$ being a point on the surface.

The quantity ∇u is easily evaluated:

$$\nabla u = \frac{e^{iku}}{u}(iku - 1) \cdot (\vec{r} - \vec{r}_p). \tag{2.27}$$

The surface A in Eq. (2.26) is supposed to be a closed surface. This is not the case for the bounded paraboloidal mirror shown in Fig. 2.4. For this reason, the mirror surface must be closed by any continuation of it making the sum a closed surface. The field on the continuation surface is assumed to be zero. In this way, the field on the entire integrating surface A becomes discontinuous since it abruptly changes to zero at the mirror boundary. A more general, than in Eq. (2.26), form of Stratton-Chu integrals, derived in [109], can be applied to an electromagnetic field having discontinuous tangential components on the integrating surface. However, in the case of emitting surface being a bounded paraboloidal mirror, both normal and tangential components of the electromagnetic field are discontinuous on A. For this reason, the fields calculated by integrals in Eq. (2.26) over the surface of mirror will not satisfy Maxwell's equations. However, Eq. (2.26) will be applied formally to the problem of mirror focused laser beam. It will be checked later how far from the solution of Maxwell's equations the result is.

The paraboloidal mirror surface is described by the following equation:

$$y^2 + z^2 = 4f_0(x + f_0). \tag{2.28}$$

The inner normal to the surface (2.28) is given by [110]:

$$\vec{n} = \frac{\vec{r}_y \times \vec{r}_z}{|\vec{r}_y \times \vec{r}_z|}, \tag{2.29}$$

where $\vec{r} = \big(x(y,z),\, y,\, z\big)$, $\vec{r}_{y,z} = \partial\vec{r}/\partial(y,z)$, and $x(y,z)$ is given by Eq. (2.28).

The evaluation of Eq. (2.29) results in

$$\vec{n} = \frac{1}{\sqrt{4f_0^2 + y^2 + z^2}}\Big(2f_0,\ -y,\ -z\Big). \tag{2.30}$$

Let us now find the fields $\vec{E}_s$ and $\vec{B}_s$ entering the integrals (2.26). These fields are formally a sum of the incident and the reflected fields at the mirror surface. As the mirror is supposed to be perfectly reflecting, let us use boundary conditions for the normal and tangential components of the fields at the perfectly conducting surface [111]:

$$\begin{aligned} \vec{E}'_n &= \vec{E}_n, \\ \vec{E}'_\tau &= -\vec{E}_\tau, \\ \vec{B}'_n &= -\vec{B}_n, \\ \vec{B}'_\tau &= \vec{B}_\tau. \end{aligned} \tag{2.31}$$

Substituting fields (2.25) into Eq. (2.31) and summing the resulting reflected field with the incident (2.25) one can get the electromagnetic field components at the integrating surface:

$$\begin{aligned} \vec{E}_s &= \Re\Big\{\frac{E}{4f_0^2 + y^2 + z^2}\Big(-4f_0 y,\ 2y^2,\ 2yz\Big)e^{-i(kx+\omega t+\psi_0)}\Big\}, \\ \vec{B}_s &= \Re\Big\{\frac{E}{4f_0^2 + y^2 + z^2}\Big(-4f_0 y,\ 2yz,\ -2(4f_0^2 + y^2)\Big)e^{-i(kx+\omega t+\psi_0)}\Big\}. \end{aligned} \tag{2.32}$$

Note that although the incident field (2.25) is a quasi-plane wave with only E_y and B_z being nonzero, the field on the surface has, generally, all the six components.

Substituting Eqs. (2.32) and (2.30) into (2.26) and noting that $\mathrm{d}S = \mathrm{d}y\mathrm{d}z/n_x$, one can finally obtain, after some tedious algebra, the equations

suitable for numerical integration:

$$\begin{aligned}
\vec{E}(\vec{r}_0) =& \frac{1}{4\pi f_0}\iint_{y^2+z^2\le r_m^2} E\Big\{\big[\frac{\vec{a}k}{u}+\frac{\vec{b}_e k}{u^2}\big]\sin\big(k(x-u)+\omega t+\psi_0\big)- \\
&-\frac{\vec{b}_e}{u^3}\cos\big(k(x-u)+\omega t+\psi_0\big)\Big\}\,\mathrm{d}y\mathrm{d}z, \\
\vec{B}(\vec{r}_0) =& \frac{1}{4\pi f_0}\iint_{y^2+z^2\le r_m^2} E\Big\{\frac{\vec{b}_h k}{u^2}\sin\big(k(x-u)+\omega t+\psi_0\big)- \\
&-\frac{\vec{b}_h}{u^3}\cos\big(k(x-u)+\omega t+\psi_0\big)\Big\}\,\mathrm{d}y\mathrm{d}z,
\end{aligned} \tag{2.33}$$

where

$$\begin{aligned}
&\vec{a} = \big(y,\ 2f_0,\ 0\big), \\
&\vec{b}_e = -y\big((x-x_0),\ (y-y_0),\ (z-z_0)\big), \\
&\vec{b}_h = \big(2f_0(z-z_0),\ -y(z-z_0),\ y(y-y_0)-2f_0(x-x_0)\big),
\end{aligned} \tag{2.34}$$

$$x = \frac{y^2+z^2}{4f_0} - f_0 \tag{2.35}$$

and

$$u = \sqrt{(x-x_0)^2+(y-y_0)^2+(z-z_0)^2}. \tag{2.36}$$

Equation (2.33) is valid for the mirror f-number $f_\# > 0.25$.

Eq. (2.33) is integrated numerically using a simple mid-point method employing a finite-sum approximation of the integral, with the terms in the sum calculated at centers of each finite piece ΔS of the integration surface. Given some particular accuracy of numerical integration, the calculation time is proportional to r_m^2. The numerical integration program was written in C language and parallelled using OpenMP extension of the C language.

Let us start the analysis of the mirror focused laser field with the case of a pure plane wave incident onto the mirror, i.e., constant $E = E_0$. As an example, let us consider a mirror having radius $r_m = 10^3\lambda$. Although this is

still 1 – 2 orders of magnitude smaller than the size of optical elements used in practice, it is already a macroscopic quantity which corresponds to mirror diameter of 2 mm for $\lambda = 1\,\mu$m.

Figure (2.5) shows the absolute value of the Poynting vector of the fields calculated using Eq. (2.33), for the mirror f-number $f_{\#} = 0.75$. The patterns shown in Fig. (2.5) possess the characteristic rings (Airy rings) caused by

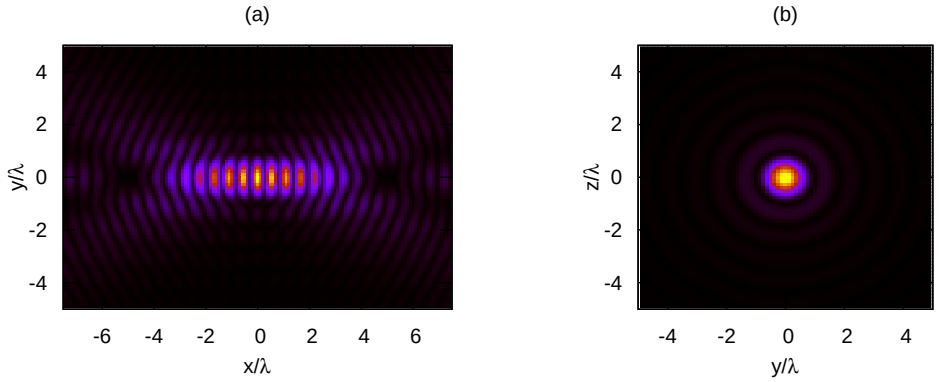

Figure 2.5: (Color) Absolute value of the focused field Poynting vector in XY (a) and YZ (b) planes passing through the geometrical focus of the parabolic mirror.

diffraction of light on the mirror boundary. As can be seen from the Fig. 2.5, the best focus of the mirror coincides with the geometrical focus of the parabolic surface. This corroborates the realism of the model used. The individual field components in the focal plane are given in Fig. 2.6. The focused laser "remembers" its polarization and thus the E_y and B_z components, the only nonzero ones in the incident field, have the maximum amplitude and focus to monopole-like structures. The longitudinal components E_x and B_x form dipole-like structures having a high amplitude, $\sim$ 25% of that of the transverse component. Therefore, this component by no means can be neglected as was done in some of the earlier studies of particle acceleration by

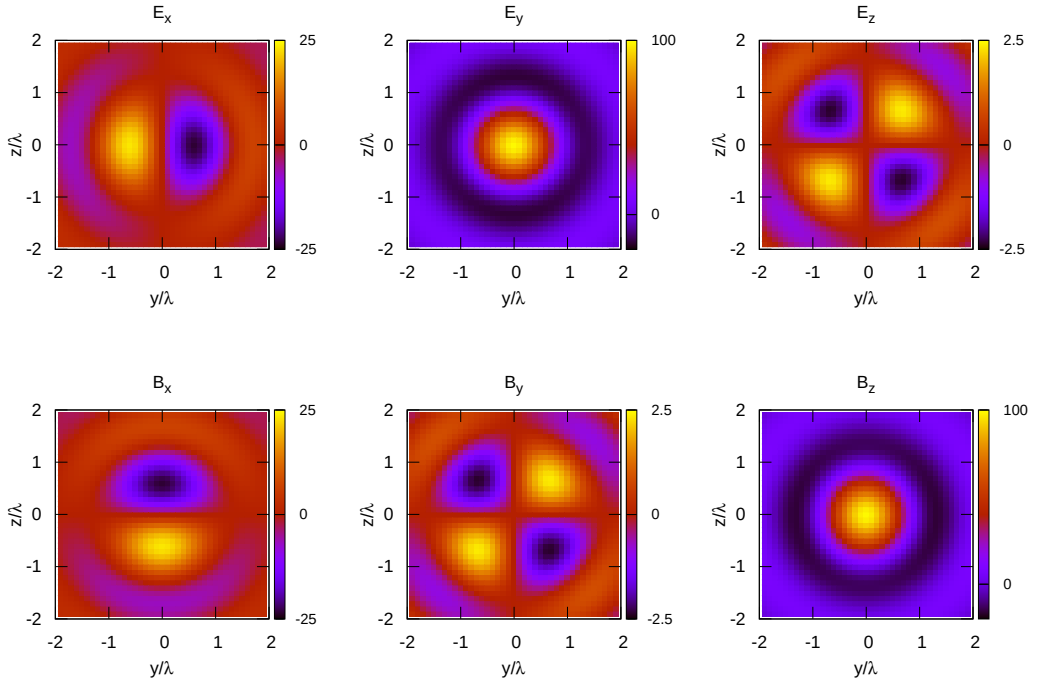

Figure 2.6: (Color) Field components in the focal plane of an $f/0.75$ mirror.

tightly focused beams [96]. The maxima of longitudinal and transverse fields are shifted in time by $\pi/2\omega$. This is accounted for in Fig. 2.6 where components E_x and B_x are shown at the shifted moment of time. Finally, there are small but non-zero components E_z and B_y which form quadrupole-like structures. These components are supposed to be exactly equal to zero in the first-order paraxial approximation (2.22).

Let us now check how well Maxwell's equations are satisfied. There are two possible sources of violation of Maxwell's equations: (1) the finite accuracy of numerical integration and (2) the inaccuracies caused by the application of Stratton-Chu integrals to the discontinuous source. In the following discussion, the fields are integrated accurately enough to make the violations due to the first source negligible. The violations due to the second source appear dependent on the mirror radius r_m. To estimate the violations quantitatively,

let us introduce the error parameter

$$\varepsilon_M = \left(|\nabla \times \vec{E} + \frac{1}{c}\frac{\partial \vec{B}}{\partial t}| + |\nabla \times \vec{B} - \frac{1}{c}\frac{\partial \vec{E}}{\partial t}| \right) \frac{\lambda}{E_{max}}, \tag{2.37}$$

where E_{max} is the field maximum at the best focus of the laser. For every mirror configuration, the quantity ε_M is spatially dependent. Specifically, let the quantity ε_{Mmax}, which is called the violation parameter below, be the maximum of this parameter within, say, ten wavelengths from the best focus. If the field exactly satisfies Maxwell's equations, this parameter is zero. The dependence of ε_{Mmax} on the mirror radius, for different f-numbers, is given in Fig. 2.7. The violation parameter almost does not depend on the f-number and decreases with increasing r_m as $1/r_m$. In this way, the larger mirror size

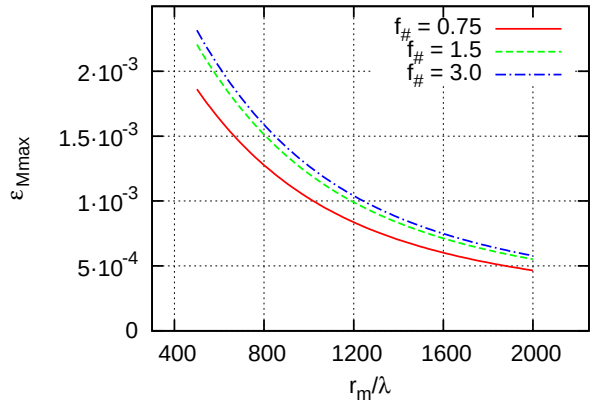

Figure 2.7: (Color) Maxwell equation violation parameter ε_{Mmax} vs. mirror radius, for $f_\# = 0.75$ (solid line), $f_\# = 1.5$ (dashed line), $f_\# = 3.0$ (dash-dotted line).

makes the violation parameter as small as desired, thus ensuring that the Maxwell equations are satisfied with the given accuracy. For the discussion in the next Section, the mirror radius will be chosen such that the resulting particles energy remain almost the same (within few percents) for any larger radius. In this way, it will be correct to claim that the results are obtained for

the source being a solution to Maxwell's equations. The Airy rings presenting in Figs. 2.5, 2.6 do not disappear with increase of r_m and thus are not caused by the approximations involved.

It is instructive to note that for the first order paraxial source given by Eq. (2.22), the violation parameter ε_{Mmax} is equal to ≈ 0.04 for $w_0 = 2\lambda$ and 0.18 for $w_0 = 1\lambda$, i.e. two orders of magnitude larger than the values in Fig. 2.7.

Let us suppose now that the mirror incident field is not a pure plane wave but rather a Gaussian beam:

$$E(x,\, y,\, z) = E_1 \exp\Big[- \Big(\frac{r}{r_g}\Big)^2 \Big], \tag{2.38}$$

where $r = \sqrt{y^2 + z^2}$ and r_g is the radius of the Gaussian beam incident onto the mirror and E_1 its constant amplitude. This structure of incident field is usually the case in practice. For the energy in the Gaussian incident beam to be equal to that in the pure plane wave, it is required that

$$E_0^2 \frac{r_m^2}{2} = E_1^2 \int_0^{r_m} \Big\{ \exp\Big[- \Big(\frac{r}{r_g}\Big)^2 \Big] \Big\}^2 r \mathrm{d}r. \tag{2.39}$$

For $r_g = r_m/2$, Eq. (2.39) gives

$$E_1 = E_0 \sqrt{8 \frac{e^8}{e^8 - 1}} \approx 2.83 E_0. \tag{2.40}$$

Although the ratio r_m/r_g can be higher than two in practice, the Gaussian incident beam is chosen to have $r_m/r_g = 2$ in this Thesis. A large ratio is equivalent to an increase of the mirror f-number since most of the incident beam energy is concentrated within a smaller, than r_m, radius. This can result in a moderate focusing even for small mirror f-numbers whereas it is interesting to study the electrons behaviour in the tight focusing regime. In

the case $r_m/r_g = 2$, $\int_0^{r_m} \exp(-2r^2/r_g^2) r\mathrm{d}r / \int_0^{\infty} \exp(-2r^2/r_g^2) r\mathrm{d}r = 99.97\%$ of the incident beam energy reaches the mirror surface and is reflected by it, while only 0.03% is wasted.

The absolute value of the Poynting vector of the Gaussian beam having $r_g = r_m/2$ focused by an $f/0.75$ mirror is given in Fig. 2.8. It can be noted that, as compared to the focused plane wave shown in Fig. 2.5, the diffraction rings have now disappeared, and the pattern is more smooth. Figure 2.9 illustrates the differences in more detail. It shows the transverse electric field

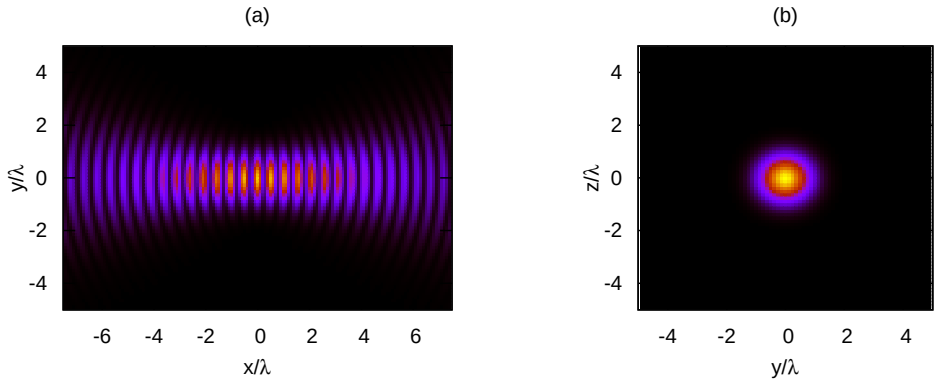

Figure 2.8: (Color) Absolute value of the focused field Poynting vector in XY (a) and YZ (b) planes passing through the geometrical focus of the parabolic mirror. The Gaussian beam with $r_g = r_m/2$ is focused by an $f/0.75$ mirror.

component of the focused plane wave and that of the focused Gaussian beam along the OY axis in the focal plane. Besides the smeared out diffraction rings, the spot size in the best focus appears larger in the case of a focused Gaussian beam whereas the maximum amplitude decreases. This results in approximately two times smaller maximum intensity of the focused Gaussian beam as compared to that of a plane wave, although the energy of the incident field within the mirror is the same. The Gaussian beam incident onto the mirror has less problems associated with the discontinuity of the fields on the

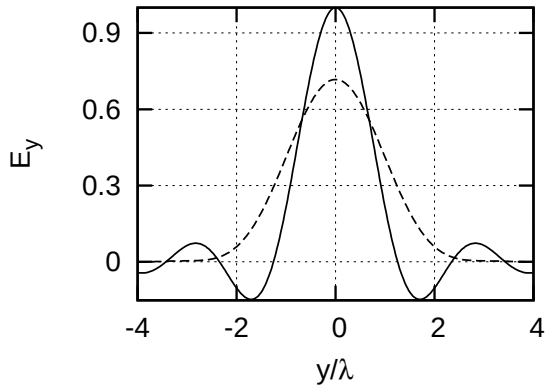

Figure 2.9: Transverse components of the field in the mirror focal plane for incident plane wave (solid line) and Gaussian beam with $r_g = r_m/2$ (dashed line). Mirror f-number is 1.

mirror boundary, especially if $r_m \gg r_g$. However, the incident field itself is no longer a solution to Maxwell's equations which, again, results in a finite ϵ_M. For the present case of $r_g = r_m/2$, nevertheless, the value of ϵ_{Mmax} has the same order as those shown in Fig. 2.7.

The smooth pattern given by the dashed line in Fig. 2.9 resembles a Gaussian shape. Therefore, it makes sense to compare it with the field given by Eq. (2.22) which has an exact Gaussian shape in the best focus. Such a comparison is given in Fig. 2.10. In Figure 2.10, the w_0 for paraxial field is chosen to be equal to the radius at which the field value of the mirror-focused spot is decreased e times as compared to that in the best focus. The comparison in Fig. 2.10 shows that, indeed, the focusing of a Gaussian beam produces a Gaussian spot, with some minor discrepancies between the structures of the mirror-focused ("exact") and the paraxial ("approximate") fields. Due to nonlinearity of the problem of charged particle acceleration, even the small discrepancies, however, can affect the dynamics of particle motion. In this way, it is of particular interest to find out when the approximate simple expressions (2.22) can be used instead of the complicated exact solution. The

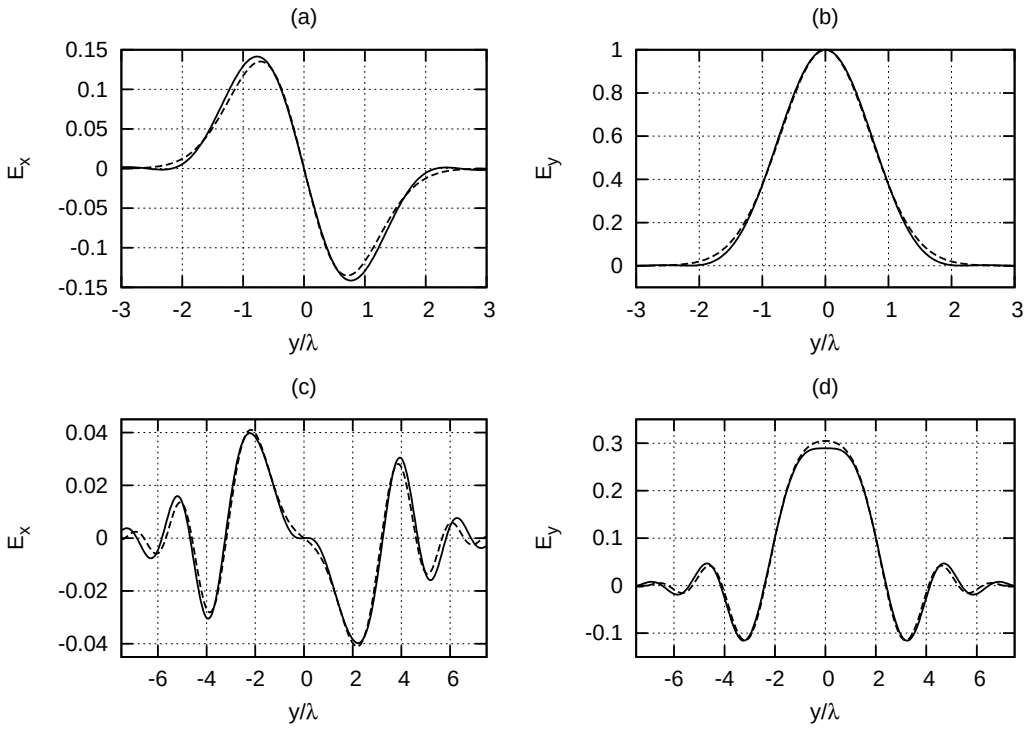

Figure 2.10: Longitudinal (a), (c) and transverse (b), (d) components of paraxial field given by Eq. (2.22) with $w_0 = 1.01\,\lambda$ (dashed lines) and $f/0.75$-focused Gaussian beam with $r_g = r_m/2$ (solid ones). Curves calculated in the focal plane (a), (b) or in the plane parallel to it and having $x = 10$ (c), (d). The phase on each figure is adjusted to maximize the field component shown.

answer to this question will be given in Section 2.3.

The last important question which needs to be discussed here is the dependence of the focal spot radius on the mirror f-number for the two types of fields incident onto the mirror. These dependencies are given in Fig. 2.11. The focal spot size in Fig. 2.11 is defined as the distance, in the focal plane, between the best focus and the closest point where the intensity is equal to one-half of that in the best focus. For larger f-numbers, the dependencies are linear, with the plane wave focused to a somewhat smaller spot than that of the Gaussian beam.

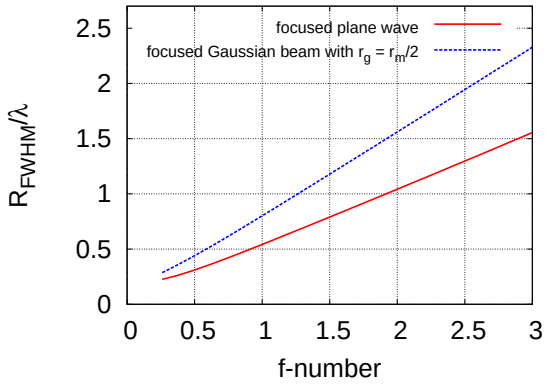

Figure 2.11: (Color) Dependence of the focal spot radius on the mirror f-number.

2.3 Acceleration of free particles in a tightly focused laser

Let us now proceed to the problem of acceleration of a single charged particle in the electromagnetic fields obtained in the previous section. These results have been reported in [63] and, in part, in [68].

In practice, the laser electromagnetic fields always have the form of a pulse. The pulse length can be very short – up to just a few laser cycles. This automatically broadens the frequency spectrum of the pulse. Furthermore, in some cases the frequency spectrum of the leading edge of the pulse does not match that of the trailing edge. It should be noted that the Stratton-Chu integrals (2.26) are derived under the assumption of a monochromatic electromagnetic wave on the exciting surface. If this wave is not monochromatic, it should be decomposed into Fourier harmonics, with the Stratton-Chu integrals taken for every harmonic. The sought field is the inverse Fourier transformation of the resulting Fourier components. However, time t enters the integrals in Eq. (2.26) only through a multiplier $e^{-i\omega t}$ which can be taken out of the integration sign. In this way, the inverse Fourier transformation can be taken indepen-

dently of the spatial integration, and the frequency spectrum of the incident pulse coincides with that of the focused one. For this reason, it is correct to just multiply the electromagnetic fields (2.26) by an envelope function $a(x_p, t)$, where x_p is the longitudinal coordinate of the particle, with the dependence on x_p also taken out of the integration sign, as x_p is independent on the integration variables y and z in Eq. (2.33). In this Thesis, the envelope is supposed to be described by a Gaussian (in time) shape given by Eq. (2.6).

The following discussion is mostly applied to the powerful lasers for which the quantity $a_{max} = eE_{max}/m\omega c \gg 1$, where E_{max} is the maximum of the field in the best focus. As a particular example, the following parameters of the laser were considered: maximum intensity of the pulse focused into a spot of $\sim 1\lambda$ in diameter is $10^{22}\,\mathrm{W/cm^2}$, laser wavelength $\lambda \approx 1\,\mu$m and laser pulse length, defined by FWHM, is 30 fs. These parameters are similar to those described in [8] for a particular laser device. The intensity of $10^{22}\,\mathrm{W/cm^2}$ corresponds to $a_{max} \approx 85$ for $\lambda = 1\,\mu$m. As follows from Fig. 2.11, the spot diameter of one wavelength corresponds to the mirror $f_{\#} \approx 0.9$ for the focused plane wave and $f_{\#} \approx 0.6$ for the focused Gaussian beam having $r_g = r_m/2$. An estimation shows that a plane wave with $\lambda \approx 1$ focused by an $f/1$ mirror and having maximum intensity in the focus equal to $10^{22}\,\mathrm{W/cm^2}$ corresponds to the peak power in the laser pulse equal to $\approx 120\,\mathrm{TW}$.

As discussed in Sec. 2.2, the proximity of the fields (2.26) to the solutions of Maxwell's equations depends on the size of the focusing mirror r_m. Furthermore, even if the fields were the exact solutions to the Maxwell equations, the field structure for different mirror radii is, in general, different, although the differences should vanish for $r_m \lggg \lambda$. As the amount of computations in the numerical integration increases with r_m as r_m^2, it is important to find the minimum value of r_m which would result in particle acceleration patterns

close to those with $r_m \ggg \lambda$ and the same intensity in the focus. It was found that for most cases the energy gained by the particle interacting with a laser, tightly focused by a mirror having $r_m = 100\,\lambda$, does not change more than by 10 – 20% if the mirror radius is further increased. The calculations in the following discussion are done for $r_m = 400\,\lambda$ and thus are believed to represent the results of interaction with a laser focused by a macroscopic mirror with accuracy of at least several percents.

It is easier to work with the dimensionless equations of motion rather than with the physical quantities in Eq. (2.1). Natural dimensionless parameters of the problem are $\vec{\xi} = k\vec{r}$, $\tau = \omega t$, $\vec{\nu} = \vec{p}/mc$ and $a = qE_{max}/m\omega c$. In the dimensionless coordinates, the equations of motion of a charged particle take form

$$\begin{aligned} \frac{\mathrm{d}\vec{\nu}}{\mathrm{d}\tau} &= a(\vec{\mathcal{E}} + \frac{\vec{\nu}}{\gamma} \times \vec{\mathcal{B}}), \\ \frac{\mathrm{d}\vec{\xi}}{\mathrm{d}\tau} &= \frac{\vec{\nu}}{\gamma}, \\ \gamma &= \sqrt{1 + \vec{\nu}^2}, \end{aligned} \tag{2.41}$$

where $\vec{\mathcal{E}}$ and $\vec{\mathcal{B}}$ are dimensionless fields: $\vec{\mathcal{E}} = \vec{E}/E_{max}$ and $\vec{\mathcal{B}} = \vec{B}/E_{max}$.

The equations of motion (2.41) of a charged particle in the fields (2.26) are solved numerically using 4-th order Runge-Kutta method [112]. To ensure that the results do not depend on properties of the particular numerical integration scheme used, some of the calculations were repeated using a 4-th order Adams method [112], with the results matched those obtained using the Runge-Kutta method.

Figure 2.12a shows a sample trajectory of an electron in the field of an $f/1$-focused plane wave having envelope length of 30 fs, laser wavelength $\lambda = 1\,\mu$m and maximum intensity in the best focus being equal to $10^{22}\,\mathrm{W/cm^2}$. As a reference, the contours of the Poynting vector absolute value at a certain moment

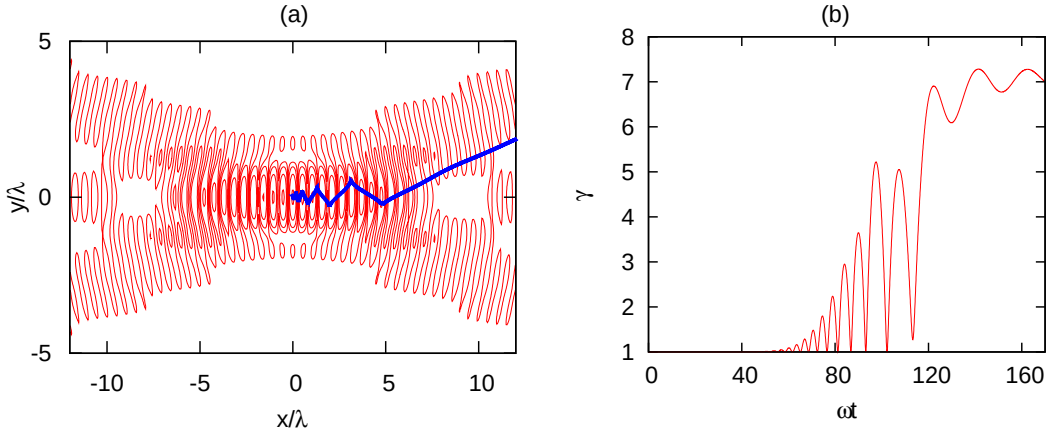

Figure 2.12: (Color) (a) Sample particle trajectory (thick blue line), with the contours of the laser intensity overlaid (thin red lines). (b) Energy evolution of the particle shown in the figure (a). The particle has started from the origin.

of time are given in Fig. 2.12a by the thin red lines. The particle dynamics resembles that of a ponderomotive force-scattered particle described in Sec. 2.1. Upon arrival of the leading edge of the laser pulse, the electron starts moving, with the trajectory similar to that of an electron in a plane wave (Fig. 2.1a). With increasing laser field intensity at the particle position, the amplitude of its oscillations increases, and particle drifts in the direction of laser propagation. Eventually, the particle leaves the region of high laser intensity. After this moment, the oscillations cease, with the particle continuing its motion along a rectilinear trajectory. These processes are illustrated by the energy evolution of the particle depicted in Fig. 2.12b. While inside the focal spot, the particle energy pattern resembles that of Fig. 2.1b. However, after the particle leaves the high intensity region, its energy becomes almost constant. The envelope center passes through the laser best focus at $\omega t \approx 175$ in Fig. 2.12b. As will be shown later, the particle still can gain or lose energy even after leaving the focal spot region. Even so, the structure of the fields provides a natural extraction mechanism which breaks the symmetry of interaction and

thus can result in a non-zero final kinetic energy of electrons.

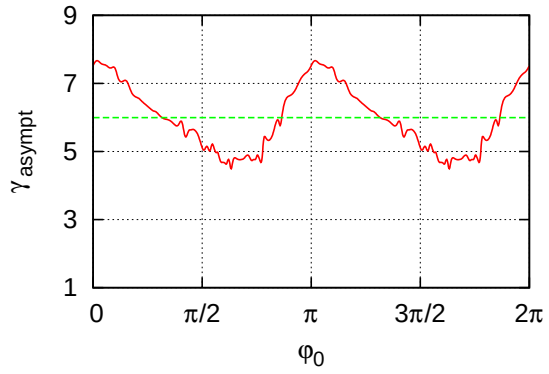

Figure 2.13: (Color) Asymptotic value of the particle γ-factor as a function of the laser phase φ_0 at the top of the pulse. The dashed line shows average of the γ-factor over the phase φ_0.

As the laser envelope is finite, the acceleration pattern depends on the phase φ_0, defined as the phase of the E_y field component at the best focus at the top of the pulse. The phase $\varphi_0 = 0$ corresponds to the maximum of the E_y field. Motion in the field having zero phase at the very top of the pulse results in, generally, a different asymptotic (at $t \to \infty$) energy than, say, that in the field having phase $\pi/2$. The corresponding dependence for the particle starting from the origin is given in Fig. 2.13. Depending on the phase, the energy can change considerably. A good way to characterize the acceleration, in this way, is an average of the energy over the phase. The corresponding average γ-factor is given in Fig. 2.13 by the dashed line.

As follows from Fig. 2.13, whatever the phase φ_0 is, the final energy is relatively small. The maximum dimensionless parameter a for the laser field is $a \approx 85$. This parameter corresponds to an ultra-relativistic motion in the case of a plane wave ($\gamma_{max} = a^2/2 \approx 3.6 \cdot 10^3$) whereas the values of γ-factor in Fig. 2.13 are almost three orders of magnitude smaller. However, it is obvious that the best focus is not the optimal initial position of the particle in the case of

a tight focus. For this position, the particle escapes the high intensity region before the top of the pulse reaches the laser focus and thus never feels a high laser field (cf. Fig. 2.12). One can anticipate that some pre-focal position should result in a higher final energy. To find out the optimal particle initial position, an energy map was created.

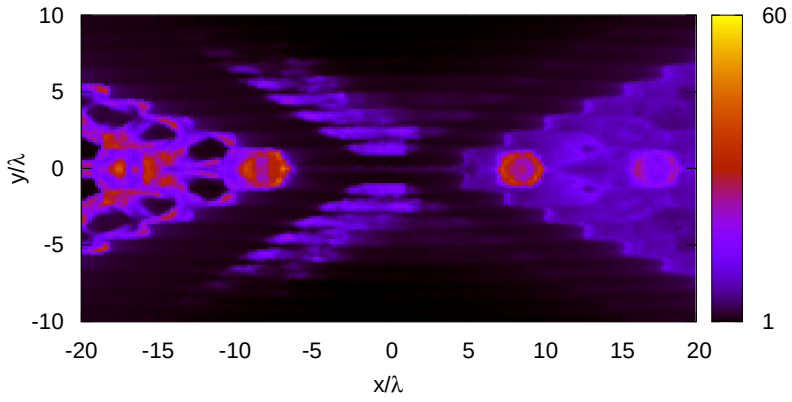

Figure 2.14: (Color) Electron energy map in XY plane for an $f/1$-focused plane wave having maximum intensity in the best focus $10^{22}\,\mathrm{W/cm^2}$, wavelength $\lambda = 1\,\mu$m and pulse length 30 fs.

An energy map is a dependence of the phase-average asymptotic energy of the particle on its initial position. Such a dependence is given for electrons in Fig. 2.14 as a color map. To create this dependence, $3.6 \cdot 10^5$ particles from the random positions in the shown box, with $z = 0$, were taken, with the subsequent average over 40 phases. It should be noted that if a particle starts from the plane $z = 0$, it will never escape this plane because the only nonzero components of laser field in the plane $z = 0$ are E_x, E_y and B_z. It can be easily seen that if $v_z = 0$ at $t = 0$, which is the case, then the force in $\hat{z}$ direction $F_z = E_z + (\vec{v} \times \vec{B})_z = 0$.

One can see from Fig. 2.14 that, indeed, the energy of the particles con-

siderably depends on their initial positions, with the optimal position being several wavelengths before the laser best focus. Although still far from the maximum value in plane wave, the electrons phase-average energy from the optimal positions are of order ≈ 30 MeV, with the maximum particle energy in individual runs, for certain phases, exceeding 100 MeV.

Let us analyze the acceleration in more detail. It was found that most of the particles with acquired energy exceeding several MeV from the energy map in Fig. 2.14 are accelerated by a combination of two major mechanisms. The first mechanism is called, as in [63], focal spot acceleration, and the second one is called Capture-and-Acceleration Scenario (CAS), as in [98, 99].

The focal spot acceleration deals with the particles appearing within the focal spot simultaneously with the maximum of the laser pulse. This results in a very rapid acceleration to a high energy during just a part of the laser cycle. This rapid acceleration stops when the particle leaves the focal spot. As an example, the trajectory and energy evolution of such a particle is given in Fig. 2.15 by the solid line.

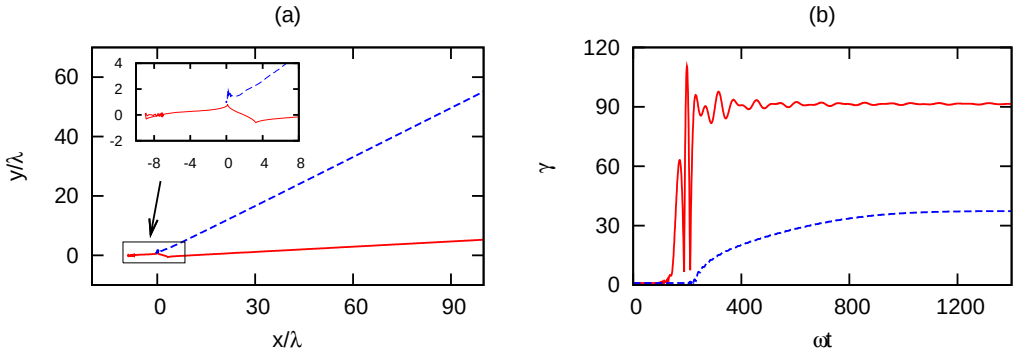

Figure 2.15: (Color) Trajectories (a) and γ-factor evolutions (b) of sample particles. Solid lines show a particle accelerating due to the focal spot acceleration mechanism, and the dashed ones show a CAS-accelerated particle. The inset in (a) shows the parts of the trajectories in the vicinity of the laser best focus.

The second mechanism, CAS, deals with the co-propagating of the particle with the laser field. For this mechanism, the particle is first accelerated to some modest energy, although relativistic, by the leading edge of the pulse. However, after the particle leaves the region of high intensity, its acceleration does not stop. The particle appears to be able to co-propagate along with the diverging laser field, with the local field phase at the particle position being approximately constant. This phase may be such that the particle feels an accelerating force which leads to a further slow increase of the energy. Furthermore, the accelerating force does not change the particle direction of propagation. The process of slow acceleration in the diverging field is illustrated by Fig. 2.15, dashed lines, and Fig. 2.16a, where the local phase of the E_y field component as seen by the particle is shown. One can see from Figs. 2.15b, dashed line, and 2.16a that, indeed, the main energy gain is acquired by the particle on the long time scale, after the field phase has locked, i.e. after the particle has started to co-propagate along with the diverging laser field, which corresponds to $\omega t \approx 230$ in the Figures. The acceleration is allowed since second and seventh conditions of the LW theorem are violated. As shown in Fig. 2.16b and in the inset in Fig. 2.16a, the particle has some modest energy with $\gamma \sim 3$ at the moment after which the phase is locked.

The process of phase locking has been connected with the subluminous phase velocity of the focused laser field along the CAS-accelerated particle trajectory in [98, 99] and, in [63], with an oscillating phase velocity of the focused field resulting in a slightly subluminous average phase velocity along a part of the trajectory. The oscillating phase velocity of the focused field is a result of the particle moving between the diffraction rings. As shown in the paper [68], the subluminous phase velocity is not, however, necessary for the particle-field synchronization; rather, if the particle has a relativistic velocity,

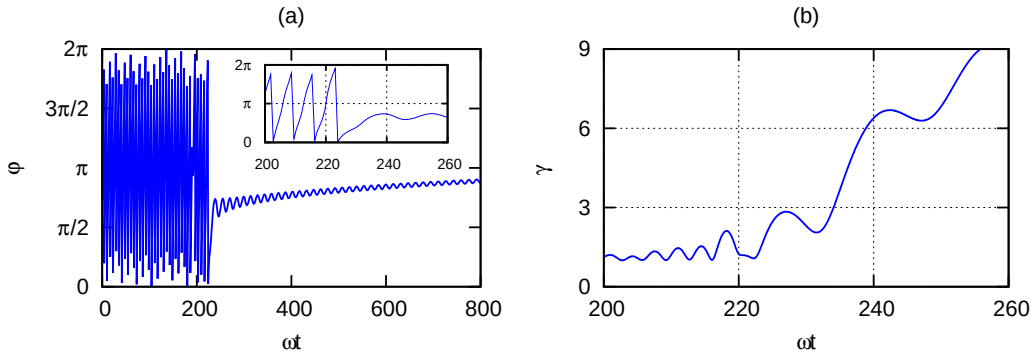

Figure 2.16: (a) Local phase of the E_y component of the laser field, as seen by the particle. The time is in the lab frame. The inset shows the field phase in the vicinity of the moment when the phase locks. (b) Behaviour of the particle γ-factor at the time scale of the inset in (a).

the phase synchronization will happen naturally on the time scale of order tens or hundreds of wavelengths. Indeed, a simple estimation shows that if there is no force at all, the phase change along a distance d for a particle with velocity v is $\delta\phi = 2\pi d(1 - v/c)/\lambda$, which, for a particle with $\gamma \approx 30$ gives $\delta\phi = \pi/4$ only at a distance $d \sim 225\lambda$. To see that the phase slippage $\delta\phi$ is small also in the case of a particle injected with a smaller γ-factor into an accelerating field, let us consider a simplified 1D model of the particle motion. In this 1D model, the particle moves under the action of a force

$$F_{1D}(r,t) = \frac{A}{r}\sin(\omega(t - r/c) + \phi_0), \tag{2.42}$$

where $A = A(r - ct)$ is a slowly varying force amplitude, ϕ_0 is a constant phase, and $k = 2\pi/\lambda = \omega/c$, as ususally. The amplitude A represents a Gaussian envelope of the pulse: $A(r - ct) = A_0 \cdot \exp[-(r/c - t - T_0)^2/\Delta T^2]$. The $1/r$ dependence of the model force amplitude is relevant to the $1/r$ dependence of all the field components of the focused laser far from its focus. The force F_{1D} depends on r since the trajectory of the synchronized particle, according to Fig.

2.15, is rectilinear along the acceleration path and thus the force acting onto the particle can be approximated by only an $\vec{r}$ nonzero component, depending on the distance from the best focus.

A relativistic 1D equation of motion of a particle under the action of the force (2.42) was solved numerically, with the parameters A_0 and ϕ_0 chosen to approximately match the resulting energy evolution pattern to that in Fig. 2.15b, dashed line[2]. The energy evolution and local phase seen by the particle that starts moving at the moment $\omega t = 230$ with $p = 2mc$ are depicted in Fig. 2.17. The qualitative agreement between the γ-factor evolutions in Figs. 2.17a and 2.15b, dashed line, and the stabilized phase pattern in Fig. 2.17b demonstrate that the initial $\gamma = 3$ is enough to prevent wave-particle dephasing, even in the field having phase velocity exactly equal to c. Since the particle velocity is slightly smaller than speed of light, after a certain large time the phase will change to a decelerating one. However, as more extensive simulations show, this happens at considerably large distances from the focus where fields are too small to noticeably change the particle energy.

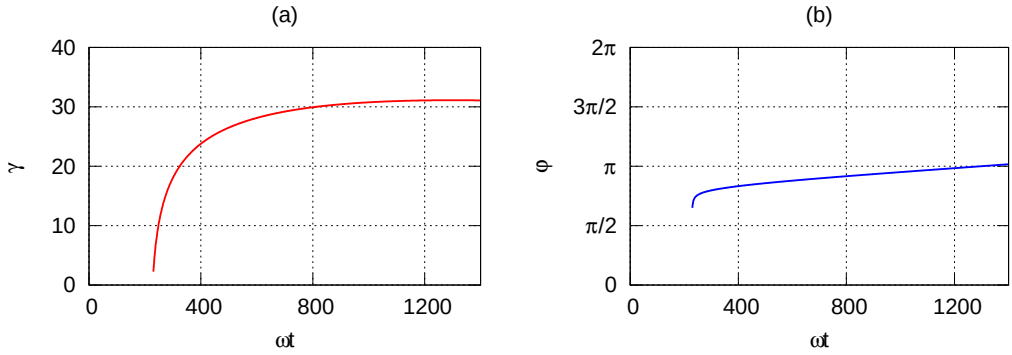

Figure 2.17: (a) Energy evolution of the particle moving in a simplified 1D model. (b) Phase of the force F_{1D} acting onto the particle, at the particle position. Time is given in the lab frame.

[2]The exact parameters used are: $A_0 = 14.1\, c^2/e$, $r(\omega t = 230) = 2.5\,\lambda$, $p(\omega t = 230) = 2\,mc$, $\phi_0 = \big(kr(t = 230) - 230\big) + 2.04$ rad

The above argumentation shows that if a particle moves along a rectilinear trajectory, and this motion has started with a relativistic velocity, the particle will remain synchronized with the field along a distance large enough to gain a finite energy. However, it is not obvious why the particle trajectory is rectilinear. To understand this aspect of the synchronized particles dynamics, let us pay attention to the details of the forces acting onto the CAS-accelerated particle.

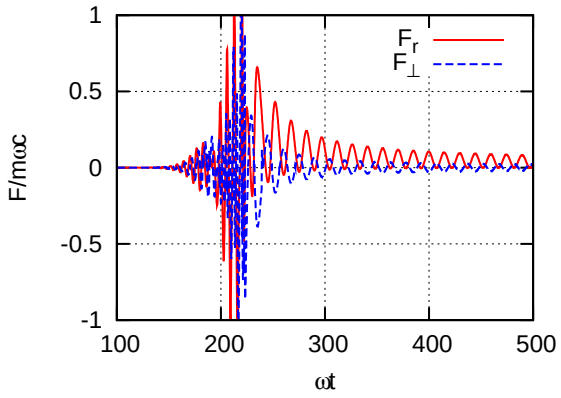

Figure 2.18: (Color) r- and $\perp$-components of the force acting onto the CAS-accelerated particle.

The total force acting onto the particle is $\vec{F} = e(\vec{E} + \vec{v} \times \vec{B}/c)$. Let its projection onto the particle direction of motion be F_r and the one perpendicular to it be $F_\perp$. Both F_r and $F_\perp$ lie in the plane $z = 0$ for the particle discussed. The two components, F_r and $F_\perp$, are depicted in Fig. 2.18. According to Fig. 2.18, after the instant $\omega t \approx 230$, correspondent to the moment of the phase lock, the $\perp$-component of the force starts to oscillate around zero whereas the force in the direction of the radius-vector oscillates around some finite value. The oscillations of the $F_\perp$ around zero value result in the stabilized direction of the particle motion (rectilinear trajectory), in agreement with the assumptions of the above discussed 1D model. On the other hand, the existence of a non-zero component of F_r gives rise to the non-zero energy gain of the particle.

To show how such a behaviour arises from the field structure let us consider a negatively charged particle having coordinate $\vec{r}_p$ and moving along the direction $\vec{r}_p$ in the plane $z = 0$. Let this particle have a fixed velocity $\vec{v}_p = \beta c\vec{r}_p/r_p$. Suppose for a while that the fields $\vec{E}(\vec{r}_p, t)$, $\vec{B}(\vec{r}_p, t)$ do not change the velocity of the particle. Let us consider quantity

$$\vec{F}(\vec{r}_p) = -e\Big[\vec{E}\big(\vec{r}_p, (k\vec{r}_p - \psi_0)/\omega\big) + \frac{\vec{v}_p}{c} \times \vec{B}\big(\vec{r}_p, (k\vec{r}_p - \psi_0)/\omega\big)\Big]. \qquad (2.43)$$

Obviously, the quantity (2.43) represents a force acting onto an electron located at point $\vec{r}_p$, moving with velocity $\vec{v}_p$ and synchronized with the laser wave at phase ψ_0. The phase ψ_0 is supposed to change so slowly with time that it can be considered almost constant.

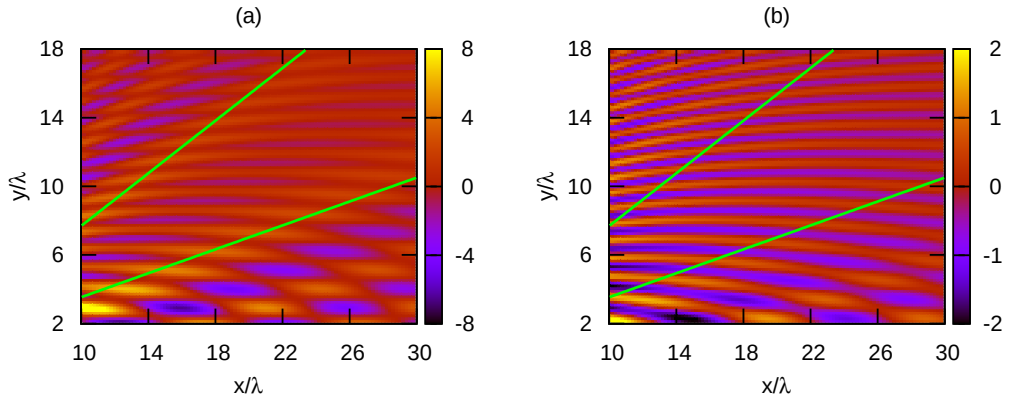

Figure 2.19: (Color) F_r (a) and $F_\perp$ (b) components of the force (2.43) for $\beta = 0.995$. The green solid lines show possible trajectories of the particles which would propagate rectilinearly and gain energy in the diverging laser field.

Figure 2.19a,b shows the values of projections of $\vec{F}$: F_r, onto the particle radius-vector, and $F_\perp$, perpendicular to it, of the quantity (2.43). The force $\vec{F}$ in Fig. 2.19 is calculated for the field of an $f/1$-mirror focused plane wave

and a certain phase ψ_0. In Fig. 2.19, β was chosen to be $\beta = 0.995$, which corresponds to a particle γ-factor $\gamma \approx 10$. It is worth to note that the patterns shown in Fig. 2.19 almost do not change for any $\gamma \gtrsim 4$.

One can see that if a particle propagates along paths shown by the green solid lines in Fig. 2.19, then the $F_\perp$ component of the force acting onto the particle should oscillate around a zero value whereas F_r oscillates around some positive value. In other words, if the particle happens to be injected, by the complicated pre-acceleration process in the focal spot, along one of these paths, it will continue moving along them. Furthermore, it will gain energy in the diverging laser field. Since the patterns in Fig. 2.19 almost do not change for larger particle energies, they will remain the same even for the particle being constantly accelerated. In other words, in the described field, the particle will gain energy due to the nonzero accelerating force F_r, and will not change direction, due to the zero average of $F_\perp$. It will stay synchronized, due to the large distance needed to be passed for a noticeable phase slippage. This results in an energy evolution shown by the dashed line in Fig. 2.15b. This behavior is a pure consequence of the laser field geometrical structure. For other field patterns it may not necessarily work. Indeed, as reported in [98, 99], for a first-order paraxial Gaussian field, the CAS is observed only for externally injected relativistic particles.

It is typical for the highest energy particles that they are accelerated by a combination of the two described mechanisms (focal spot acceleration and CAS). A sample energy evolution is given in Fig. 2.20.

One can determine a scaling of the maximum possible electron energy versus mirror f-number, for a fixed laser power, or versus laser power, for a fixed mirror geometry. Such dependencies are given in Fig. 2.21a,b. Figure 2.21a shows the scaling of maximum possible energy vs. f-number for a 120

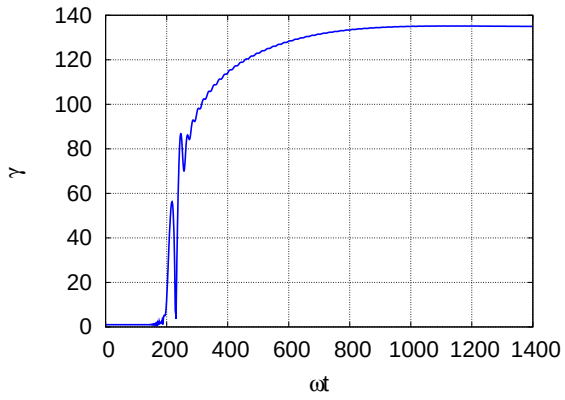

Figure 2.20: A sample energy evolution of a high-energy particle.

TW laser. Unlike the phase-averaged energy scaling ([63]), the scaling is non-monotonic, with two local maxima. The dependence of the particle dynamics on the laser phase for the case when the two acceleration mechanisms work, is, in fact, much more severe than that shown in Fig. 2.13. Due to this strong dependence, the phase-averaged energy in ([63]) followed a simpler scaling. The reason for the two local maxima is a competition between the two acceleration mechanisms when the f-number changes. Extensive study of the particle dynamics from the energy map in Fig. 2.14 shows that the energetic particles from the bright spots behind the focus ($-10 < x/\lambda < -5$) are mostly accelerated by the focal spot acceleration or by the combination between the two mechanisms as shown in Fig. 2.20. The particles from the horizontal lines, right above and below the best focus in Fig. 2.14, are mostly accelerated by CAS. For $f_{\#} = 1$, the pure CAS-accelerated particles acquire considerably, at least 3 times, smaller energy than the focal spot acceleration. However, if the laser is defocused, this situation changes (see Fig. 2.21c). The energy gain of the focal spot accelerated particles decreases whereas that of CAS increases. For this reason, with defocusing from $f_{\#} = 1$ to $f_{\#} \approx 2$, the maximum energy decreases. This trend changes for $f_{\#} \gtrsim 2$ where the CAS-accelerated par-

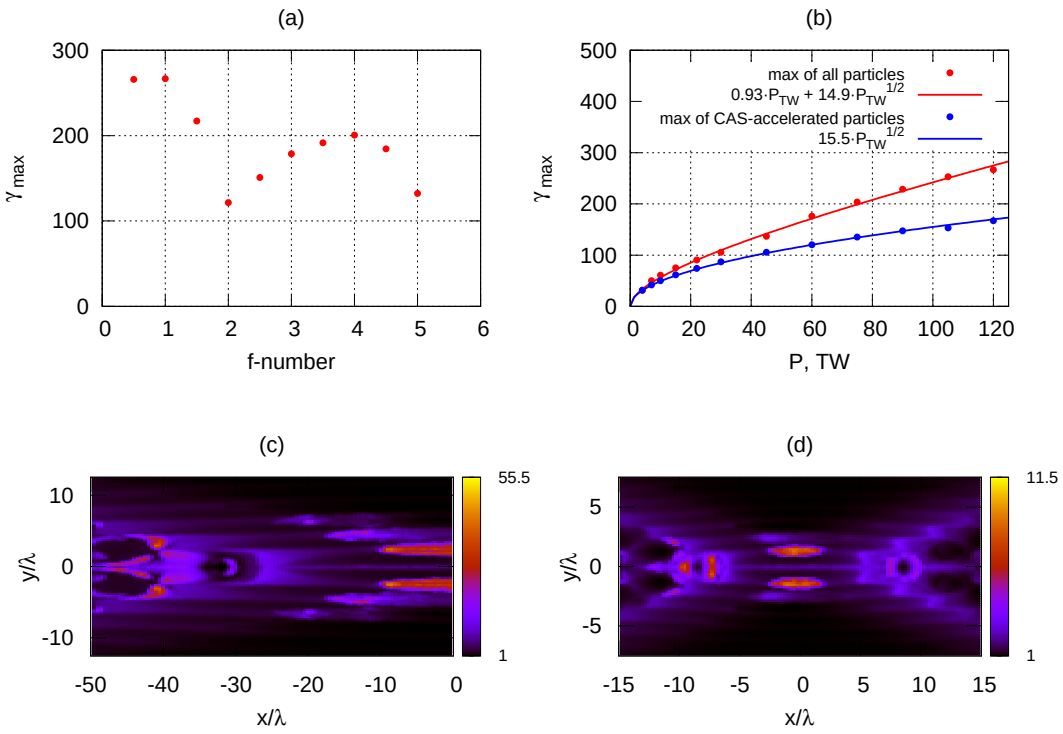

Figure 2.21: (Color). Focused plane wave. (a) Maximum particle γ-factor vs. $f_{\#}$; (b) γ-factor scaling for $f_{\#} = 1$; (c) energy map for a 120 TW laser focused by an $f/2$ mirror; (d) energy map for a 7 TW laser focused by an $f/1$ mirror.

ticles, for which the maximum energy keeps increasing, play the major role. The maximum energy continues increasing until $f_{\#} \sim 4$ and then the energy decreases again. For very large f-numbers, the fields become too small for the CAS mechanism to work.

The pattern type shown in Fig. 2.14 for laser power $P = 120\,\mathrm{TW}$ keeps its geometry for other values of power. This is demonstrated in Fig. 2.21d where the energy map for $P = 7\,\mathrm{TW}$ is given. The particles from the horizontal lines right above and below the best focus are accelerated predominantly by CAS for the smaller laser power, too. It therefore makes sense to have the maximum energy scaling vs. laser power for two kinds of particles: all the particles and those from the horizontal lines regions. The corresponding dependencies are given in Fig. 2.21b by the red and blue colored points. The fitting curves are

given in Fig. 2.21b by the solid lines. The absolute maximum energy scales as a sum of functions proportional to P and to $\sqrt{P}$, due to the different scalings of the two discussed major accelerating mechanisms. The CAS-accelerated particles are scaled as $\sqrt{P}$ as shown in Fig. 2.21b by the blue line.

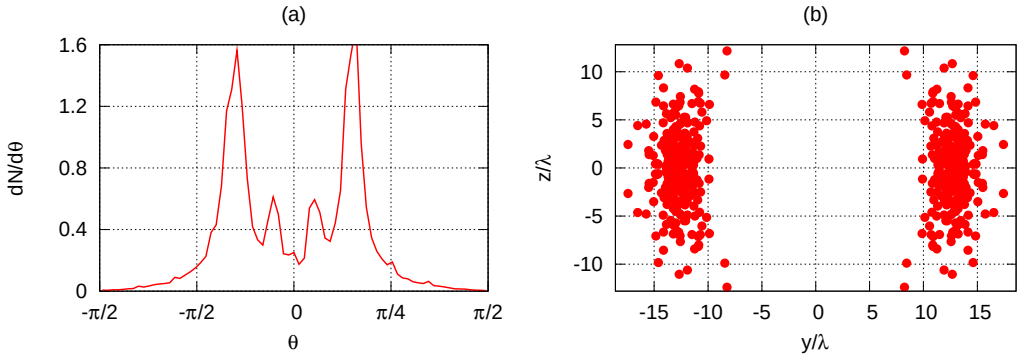

Figure 2.22: (a) Angular distribution of all particles having $\gamma > 30$ in the case of $f/1$-focused 120 TW laser. The distribution is normalized to unity. θ is the angle between the particle momentum and OX axis. (b)Transverse positions, at a certain moment when all the particles have finished oscillations and started to move along a rectilinear trajectory, of the 2% most energetic electrons from 25 000 electrons initially regularly distributed in the square of size $10 \times 10\lambda$ with center at $(-2\lambda, 0, 0)$, parallel to the YZ plane. The laser is tightly focused ($f_{\#} = 0.9$).

The patterns in Fig. 2.19 depend on the synchronization phase ψ_0 and therefore different synchronization phases ψ_0 result in the different paths allowing acceleration in the diverging laser field. These rectilinear paths have certain angles between them and the laser propagation direction. For this reason, the accelerated particles have some angular spread. However, if one filters the most energetic particles, one finds that they are accelerated by the same path giving the maximum energy. Therefore, the most energetic particles are grouped around a certain direction, with a small angular spread. This is demonstrated in Fig. 2.22a where the angular distribution of the energetic particles is shown. Due to the maxima in the angular distribution, the most

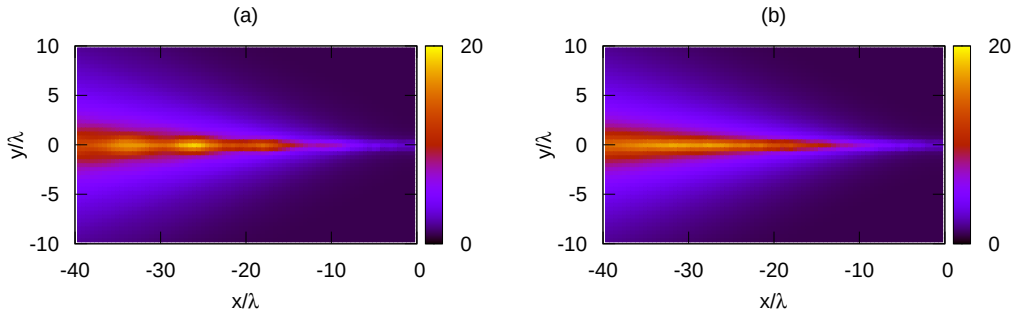

Figure 2.23: (Color) Electron energy maps of (a) a Gaussian beam focused by an $f/1$ parabolic mirror; (b) a paraxial beam with $w_0 = 1.35\,\lambda$ which results in the same FWHM as in (a). The both energy maps are calculated for the same laser power $P \approx 120$ TW.

energetic particles form jets having maximum density in a certain direction. In 3D space, the centers of the jets lie in the XY plane as shown in Fig. 2.22b[3].

As was shown in Section 2.2, a focused Gaussian beam of large radius possesses a structure very close to that of a Gaussian beam in paraxial approximation. Since calculating realistic fields through the Stratton-Chu integrals requires considerable computing resources, it is of great interest to find out when a paraxial approximation can be used in the problems of charged particle acceleration. Figure 2.23 gives energy maps of electrons accelerated by an $f/1$-focused Gaussian beam and a paraxial beam having the same FWHM in the focus.

The patterns in Fig. 2.23 look very similar, and are considerably different from that in Fig. 2.14 where the presence of diffraction rings has largely affected the particle dynamics. The energy values on both maps in Fig. 2.23 are of the same order and are noticeably smaller than those in Fig. 2.14. It is obvious, that for high beam radii in the focus, the two field representations, mirror-focused Gaussian beam and paraxial Gaussian beam, must give iden-

[3]Figure 2.22b was taken from [63], Fig. 13.

tical results. However, for smaller radii of the laser beam in the focus the paraxial approximation gives an inaccurate result. Therefore, a critical value of w_0 in Eq. (2.22) should exist, such that it is safe, with a certain accuracy, to use paraxial approximation for all values of w_0 larger than the critical one. The solid line in Figure 2.24a shows a maximum relative difference between

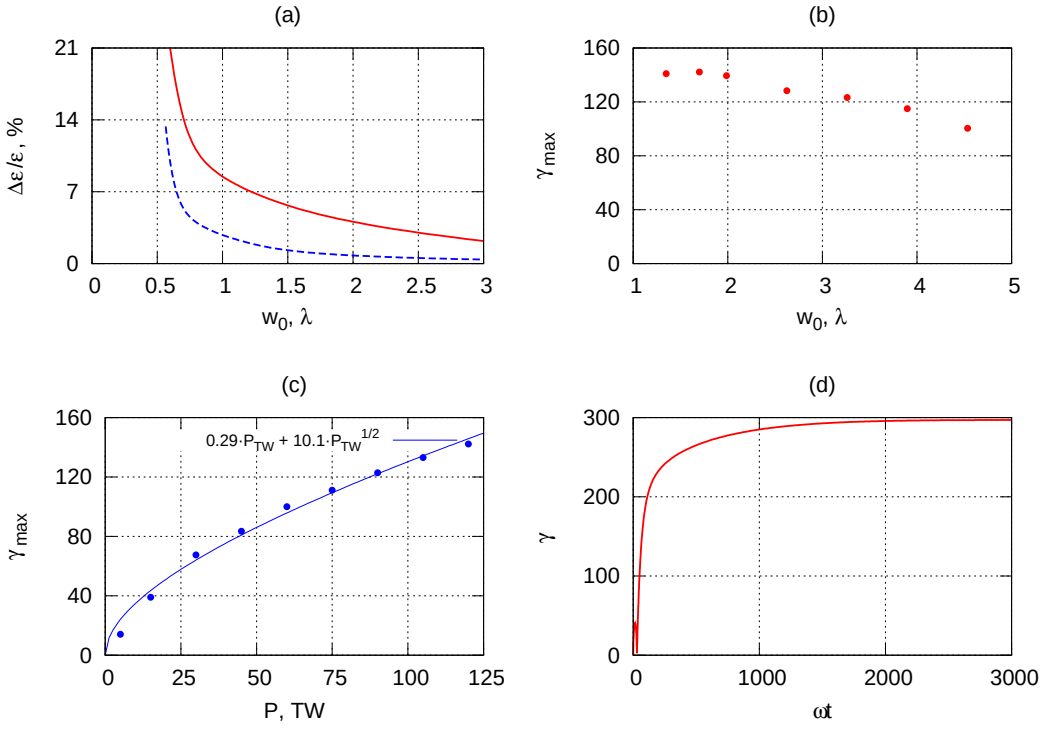

Figure 2.24: (Color) (a) Relative maximum difference vs. laser waist size between the particle γ-factors from the best focus of a focused Gaussian beam and a 1-st (solid line) or 5-th (dashed line) order paraxial Gaussian beam. Maximum value of a at the best focus is $a = 1$. (b) Scaling of the maximum acquirable particle energy in the 1-st order paraxial Gaussian field vs. w_0 for laser power 120 TW. (c)Scaling of the maximum acquirable particle energy vs. laser power for $w_0 = 1.7$ that corresponds to relative error 5% in Fig. 2.24a. (d) Energy evolution of a sample CAS-accelerated particle injected into the middle of the pulse at the best focus of a Gaussian laser beam, $P = 120\,\mathrm{TW}$, $f_\# = 1$.

the kinetic energies of the particles accelerated by the exact and approximate fields. The particle is located at the laser best focus at $t \to -\infty$. As an additional check, the comparison of the exact field with the 5-th order paraxial

approximation [100]:

$$
\begin{aligned}
E_x &= E_0\frac{y}{w}\exp\Big(-\big[\frac{r}{w}\big]^2\Big)\cdot\Big\{\epsilon\frac{w_0}{w}\cos[\phi_G^{(1)}]+\\
&\quad \epsilon^3\big(-\frac{w_0^2}{2w^2}\cos[\phi_G^{(2)}]+\frac{r^2w_0}{w^3}\cos[\phi_G^{(3)}]-\frac{r^4}{4w^4}\cos[\phi_G^{(4)}]\big)+\\
&\quad \epsilon^5\big(-\frac{3w_0^3}{8w^3}\cos[\phi_G^{(3)}]-\frac{3r^2w_0^2}{8w^4}\cos[\phi_G^{(4)}]+\frac{17r^4w_0}{16w^5}\cos[\phi_G^{(5)}]-\\
&\quad \frac{3r^6}{8w^6}\cos[\phi_G^{(6)}]+\frac{r^8}{32w_0w^7}\cos[\phi_G^{(7)}]\big)\Big\},\\
E_y &= E_0\frac{w_0}{w}\exp\Big(-\big[\frac{r}{w}\big]^2\Big)\cdot\Big\{\sin[\phi_G]+\\
&\quad \epsilon^2\big(\frac{y^2}{w^2}\sin[\phi_G^{(2)}]-\frac{r^4}{4w_0w^3}\sin[\phi_G^{(3)}]\big)+\\
&\quad \epsilon^4\big(\frac{w_0^2}{8w^2}\sin[\phi_G^{(2)}]-\frac{r^2w_0}{4w^3}\sin[\phi_G^{(3)}]-\frac{r^2(r^2-16y^2)}{16w^4}\sin[\phi_G^{(4)}]-\\
&\quad \frac{r^4(r^2+2y^2)}{8w_0w^5}\sin[\phi_G^{(5)}]+\frac{r^8}{32w_0^2w^6}\sin[\phi_G^{(6)}]\big)\Big\},\\
E_z &= E_0\frac{yz}{ww_0}\exp\Big(-\big[\frac{r}{w}\big]^2\Big)\cdot\Big\{\epsilon^2\frac{w_0^2}{w^2}\sin[\phi_G^{(2)}]+\\
&\quad \epsilon^4\big(\frac{r^2w_0^2}{w^4}\sin[\phi_G^{(4)}]-\frac{r^4w_0}{4w^5}\sin[\phi_G^{(5)}]\big)\Big\},
\end{aligned}
\tag{2.44}
$$

$$
\begin{aligned}
B_x &= E_0\frac{z}{w}\exp\Big(-\big[\frac{r}{w}\big]^2\Big)\cdot\Big\{\epsilon\frac{w_0}{w}\cos[\phi_G^{(1)}]+\\
&\quad \epsilon^3\big(2\frac{w_0^2}{2w^2}\cos[\phi_G^{(2)}]+\frac{r^2w_0}{2w^3}\cos[\phi_G^{(3)}]-\frac{r^4}{4w^4}\cos[\phi_G^{(4)}]\big)+\\
&\quad \epsilon^5\big(\frac{3w_0^3}{8w^3}\cos[\phi_G^{(3)}]+\frac{3r^2w_0^2}{8w^4}\cos[\phi_G^{(4)}]+\frac{3r^4w_0}{16w^5}\cos[\phi_G^{(5)}]-\\
&\quad \frac{r^6}{4w^6}\cos[\phi_G^{(6)}]+\frac{r^8}{32w_0w^7}\cos[\phi_G^{(7)}]\big)\Big\},\\
B_y &= 0,\\
B_z &= E_0\frac{w_0}{w}\exp\Big(-\big[\frac{r}{w}\big]^2\Big)\cdot\Big\{\sin[\phi_G]+\\
&\quad \epsilon^2\big(\frac{r^2}{2w^2}\sin[\phi_G^{(2)}]-\frac{r^4}{4w_0w^3}\sin[\phi_G^{(3)}]\big)+\\
&\quad \epsilon^4\big(-\frac{w_0^2}{8w^2}\sin[\phi_G^{(2)}]+\frac{r^2w_0}{4w^3}\sin[\phi_G^{(3)}]+\frac{5r^4}{16w^4}\sin[\phi_G^{(4)}]-\\
&\quad \frac{r^6}{4w_0w^5}\sin[\phi_G^{(5)}]+\frac{r^8}{32w_0^2w^6}\sin[\phi_G^{(6)}]\big)\Big\},
\end{aligned}
\tag{2.45}
$$

where

$$\phi_G^{(n)} = \phi_G + n \cdot \arctan(x/x_R), \tag{2.46}$$

is done and shown in Fig. 2.24a by the dashed line. To match the f-number of the mirror used for calculating the exact field and w_0 for paraxial approximation, it was demanded that the total energy flux of the two sources through the focal plane was equal to each other, i.e.,

$$\int S_x^{(mirror focused)} \mathrm{d}s = \int S_x^{(paraxial)} \mathrm{d}s, \tag{2.47}$$

where $\vec{S}$ is the Poynting vector and integration was carried out over the focal plane. Since the accuracy of several percents which was provided by the mirror having $r_m = 400\,\lambda$ is not sufficient for the precise comparisons, the mirror radius was taken to be $r_m = 10^4\,\lambda$. This value guarantee that the energies of the particles coincide with those of asymptotic value $r_m \to \infty$ with accuracy $\sim 10^{-3}$. The numerical integration of the Stratton-Chu integrals was carried out with accuracy not worser than 10^{-7}.

It can be seen from Fig. 2.24a that for $w_0 \gtrsim 2\,\lambda$ the difference between the results calculated with exact and 1-st order paraxial field representations can be as small as $\sim 5\%$. If the size of the spot is higher than this value it is safe to use the paraxial approximation and be sure the obtained results coincide with the exact ones with at most a few percents. If the 5-th order paraxial approximation is used, the error does not exceed 5% for $w_0 \gtrsim 1\,\lambda$.

Since the discrepancies between the particle dynamics in the mirror-focused Gaussian and paraxial Gaussian fields are small, one can use the paraxial field to repeat the scalings of Fig. 2.21a,b. These scalngs are given in Fig. 2.24b,c for the 1-st order paraxial field. Compared to the values in Fig. 2.21a,b, the Gaussian field has produced smaller energies. The dependence $\gamma_{max}(w_0)$, on

the other hand, has become more uniform. The reason for this is that it was impossible to find CAS-accelerated free particles in the case of a Gaussian field. However, if the particle is injected into the middle of the pulse then it is still possible to accelerate it via CAS and acquire a high energy. An example of energy evolution of such a particle started from right above the laser best focus is given in Fig. 2.24d. Note that the curve in Fig. 2.24d does not have the tiny fast oscillations as was the case in the case of a focused plane wave (cf. Fig. 2.20). Apparently, these oscillations were associated with the existence of diffraction rings in the case of a focused plane wave.

It is shown in Section 2.5 that a mechanism of particle injection exists which makes the CAS acceleration possible in the case of a focused Gaussian field.

2.4 Electromagnetic 3D PIC code SCPIC

2.4.1 General outline

In the previous section, motion of a free single particle in a field of a tightly focused plane polarized beam has been analyzed. However, motion of an isolated particle, although important, is rarely interesting in practice where the laser usually interacts with plasma targets of a certain density. To study such interactions one needs to use special tools. The most widely used tools for studying laser-plasma interactions are Particle-in-Cell (PIC) codes.

The code SCPIC was created by the author of this Thesis in 2008. Most of methods, although standard, were borrowed from the parallel PIC code Mandor [113] which was developed at the University of Alberta in 2002 – 2005. The SCPIC code solves Maxwell's equations using a certain finite-difference-time-domain (FDTD) method. To solve for the plasma evolution, the code

finds a numerical approximation to the solution of the Vlasov equation:

$$\begin{aligned} \frac{\partial f_\alpha}{\partial t} + \frac{\partial f_\alpha}{\partial \vec{r}} \cdot \vec{v} + \frac{\partial f_\alpha}{\partial \vec{p}} \cdot \dot{\vec{p}} = 0, \\ \dot{\vec{p}} = q\big[\vec{E}(\vec{r},t) + \frac{\vec{v}}{c} \times \vec{B}(\vec{r},t)\big], \end{aligned} \tag{2.48}$$

where $f_\alpha(\vec{r},\vec{p},t)$ is the single-particle distribution function of the α-th species representing density of its particles in the 6D phase space, $f_\alpha = \mathrm{d}N_\alpha/\mathrm{d}^3r\mathrm{d}^3p$, and the fields $\vec{E}(\vec{r},t)$ and $\vec{B}(\vec{r},t)$ are the sum of external and the internal plasma fields. In this way, the code is in principle capable of solving only problems of interaction of laser light with collisionless plasma.

Equation (2.48) can be solved using the method of characteristics [114]. As the distribution function depends on the phase space coordinates $\vec{r}$ and $\vec{p}$ and time t, Eq. (2.48) can be written as

$$\frac{\mathrm{d}f_\alpha}{\mathrm{d}t} = 0. \tag{2.49}$$

In this way, the distribution function of an infinitesimal piece of plasma stays constant along the trajectory of the piece in the phase space. This trajectory is called characteristic. Mathematically, finding the characteristic is equivalent to finding the seven functions $\vec{r}(s)$, $\vec{p}(s)$, $t(s)$ of a parameter s. Given these seven dependencies, a curve in the 7D (phase space + time) space can be specified. These dependencies must satisfy the following differential equations [115]:

$$\begin{aligned} \frac{\mathrm{d}t}{\mathrm{d}s} &= 1, \\ \frac{\mathrm{d}\vec{r}}{\mathrm{d}s} &= \vec{v}(s), \\ \frac{\mathrm{d}\vec{p}}{\mathrm{d}s} &= \dot{\vec{p}}\big(\vec{r}(s),\vec{p}(s),t(s)\big). \end{aligned} \tag{2.50}$$

The family of characteristics defines a hypersurface over which the distri-

bution function is a solution to the Vlasov equation.

In the code, only a finite family of characteristics is tracked. To accomplish this goal, the code has a number of markers, with the i-th marker specifying a point in the phase space, at time t, lying along the i-th characteristic. The position of every marker in the phase space is obtained by numerical solution of Eq. (2.50) for each marker. Each marker is associated with a value of an α-th distribution function at $t = 0$ at the marker's initial position.

To solve equation (2.50) for each of the markers, one needs to know the fields $\vec{E}$ and $\vec{B}$. These fields can be found from Maxwell's equations:

$$\begin{aligned} \nabla \times \vec{E} &= -\frac{1}{c}\frac{\partial \vec{B}}{\partial t}, \\ \nabla \times \vec{B} &= \frac{1}{c}\frac{\partial \vec{E}}{\partial t} + \frac{4\pi}{c}\vec{J}. \end{aligned} \tag{2.51}$$

Equation (2.51) contains the quantity $\vec{J}$ which is a sum of moments of the distribution functions f_α:

$$\vec{J} = \sum_\alpha q_\alpha \int \vec{v} f_\alpha \mathrm{d}^3 p, \tag{2.52}$$

where q_α is the charge of the α-th particle species. As the code has only a finite number of characteristics, it is a common situation that there are no markers at the point $(\vec{r}, \vec{p})$ at time t. For this reason, the value of $f_\alpha(\vec{r}, \vec{p}, t)$ is found by summing the contributions of markers in a certain vicinity of the point $(\vec{r}, \vec{p})$. The particular mechanism is described in a subsection below. In fact, the step of evaluation of f_α is omitted entirely and J is computed directly from the information about the markers in vicinity of a point $\vec{r}$ in the space.

The code algorithm can be summarized in simple terms as follows. The plasma is represented by a finite set of markers moving in the phase space and

described by the set of equations of motion (2.50). These equations contain fields $\vec{E}$ and $\vec{B}$ which are found by a solution to Eq. (2.51). The last equations contain, in turn, the current density term $\vec{J}$ which is evaluated from the positions of the markers in the phase space. Thus, at each discrete time step, the set of markers positions in the phase space gives the current density $\vec{J}$, which allows one to update the fields $\vec{E}$ and $\vec{B}$ to the next time step. The new fields are used to update the coordinates and velocities of the markers to the next time step. This sequence is repeated further until the problem calculation is finished.

It is convenient to work in dimensionless units. The only physical variable through which all dimensional units can be expressed is the laser frequency ω. Using this parameter the dimensionless quantities can be obtained by dividing the physical ones by:

$$\begin{aligned}
t_0 &= \frac{2\pi}{\omega} \text{ (for time)}, \\
r_0 &= \frac{2\pi c}{\omega} \text{ (for coordinate)}, \\
p_0 &= mc \text{ (for momentum)}, \\
E_0 &= \frac{m\omega c}{2\pi e} \text{ (for electromagnetic field)}, \\
n_0 &= \frac{m\omega^2}{16\pi^3 e^2} \text{ (for particle density)}, \\
J_0 &= en_0 c \text{ (for current density)}, \\
\rho_0 &= en_0 \text{ (for charge density)}.
\end{aligned} \tag{2.53}$$

In (2.53), e and m are charge and mass of an electron and c is the speed of light.

The details of the code algorithms are given in the following subsections.

2.4.2 Finite-difference solution to the Maxwell equations

The Maxwell equations for the field are solved in the SCPIC code using a classical FDTD method known as the Yee scheme [116]. The Yee scheme gives a numerical solution having 2-nd order accuracy in both time and space and uses a regular mesh.

The meshes for different field components are displaced from each other in space. If Δx, Δy and Δz are mesh steps along x, y and z and Δt is the time step, then a quantity $A(x, y, z, t)$ at a mesh node (i, j, k) can be written as

$$A^n_{i,j,k} = A(i\Delta x, j\Delta y, k\Delta z, n\Delta t), \tag{2.54}$$

where n is the number of the time step.

In this notation the storage scheme for the components of vectors $\vec{E}$, $\vec{B}$ and $\vec{J}$ in the Yee scheme can be written as follows

$$\begin{aligned} &B_{x\,i,\,j-0.5,\,k-0.5}^{\,n-0.5}, \quad B_{y\,i-0.5,\,j,\,k-0.5}^{\,n-0.5}, \quad B_{z\,i-0.5,\,j-0.5,\,k}^{\,n-0.5} \\ &E_{x\,i-0.5,\,j,\,k}^{\,n}, \quad E_{y\,i,\,j-0.5,\,k}^{\,n}, \quad E_{z\,i,\,j,\,k-0.5}^{\,n}, \\ &J_{x\,i-0.5,\,j,\,k}^{\,n-0.5}, \quad J_{y\,i,\,j-0.5,\,k}^{\,n-0.5}, \quad J_{z\,i,\,j,\,k-0.5}^{\,n-0.5}. \end{aligned} \tag{2.55}$$

In this way, B_x at the mesh node (i, j, k) at time step n is evaluated at $x = i\Delta x$, $y = (j - 0.5)\Delta y$, $z = (k - 0.5)\Delta z$ and $t = (n - 0.5)\Delta t$ and so on. Using the storage scheme (2.55), the finite-difference approximation to the Maxwell

equations (2.51) can be written as

$$
\begin{aligned}
B_{x\,i,\,j-0.5,\,k-0.5}^{\;n+0.5} &= B_{x\,i,\,j-0.5,\,k-0.5}^{\;n-0.5} + \Delta t\cdot \\
&\Big[\frac{E_{y\,i,\,j-0.5,\,k}^{\;n} - E_{y\,i,\,j-0.5,\,k-1}^{\;n}}{\Delta z} - \frac{E_{z\,i,\,j,\,k-0.5}^{\;n} - E_{z\,i,\,j-1,\,k-0.5}^{\;n}}{\Delta y}\Big], \\
B_{y\,i-0.5,\,j,\,k-0.5}^{\;n+0.5} &= B_{y\,i-0.5,\,j,\,k-0.5}^{\;n-0.5} + \Delta t\cdot \\
&\Big[\frac{E_{z\,i,\,j,\,k-0.5}^{\;n} - E_{z\,i-1,\,j,\,k-0.5}^{\;n}}{\Delta x} - \frac{E_{x\,i-0.5,\,j,\,k}^{\;n} - E_{x\,i-0.5,\,j,\,k-1}^{\;n}}{\Delta z}\Big], \\
B_{z\,i-0.5,\,j-0.5,\,k}^{\;n+0.5} &= B_{x\,i-0.5,\,j-0.5,\,k}^{\;n-0.5} + \Delta t\cdot \\
&\Big[\frac{E_{x\,i-0.5,\,j,\,k}^{\;n} - E_{x\,i-0.5,\,j-1,\,k}^{\;n}}{\Delta y} - \frac{E_{y\,i,\,j-0.5,\,k}^{\;n} - E_{y\,i-1,\,j-0.5,\,k}^{\;n}}{\Delta x}\Big],
\end{aligned}
\tag{2.56}
$$

and

$$
\begin{aligned}
E_{x\,i-0.5,\,j,\,k}^{\;n+1} &= E_{x\,i-0.5,\,j,\,k}^{\;n} + \\
&\Delta t\cdot\Big[\frac{B_{z\,i-0.5,\,j+0.5,\,k}^{\;n+0.5} - B_{z\,i-0.5,\,j-0.5,\,k}^{\;n+0.5}}{\Delta y} - \\
&\frac{B_{y\,i-0.5,\,j,\,k+0.5}^{\;n+0.5} - B_{y\,i-0.5,\,j,\,k-0.5}^{\;n+0.5}}{\Delta z} - J_{x\,i-0.5,\,j,\,k}^{\;n+0.5}\Big], \\
E_{y\,i,\,j-0.5,\,k}^{\;n+1} &= E_{y\,i,\,j-0.5,\,k}^{\;n} + \\
&\Delta t\cdot\Big[\frac{B_{x\,i,\,j-0.5,\,k+0.5}^{\;n+0.5} - B_{x\,i,\,j-0.5,\,k-0.5}^{\;n+0.5}}{\Delta z} - \\
&\frac{B_{z\,i+0.5,\,j-0.5,\,k}^{\;n+0.5} - B_{z\,i-0.5,\,j-0.5,\,k}^{\;n+0.5}}{\Delta x} - J_{y\,i,\,j-0.5,\,k}^{\;n+0.5}\Big], \\
E_{z\,i,\,j,\,k-0.5}^{\;n+1} &= E_{z\,i,\,j,\,k-0.5}^{\;n} + \\
&\Delta t\cdot\Big[\frac{B_{y\,i+0.5,\,j,\,k-0.5}^{\;n+0.5} - B_{y\,i-0.5,\,j,\,k-0.5}^{\;n+0.5}}{\Delta x} - \\
&\frac{B_{x\,i,\,j+0.5,\,k-0.5}^{\;n+0.5} - B_{x\,i,\,j-0.5,\,k-0.5}^{\;n+0.5}}{\Delta y} - J_{x\,i,\,j,\,k-0.5}^{\;n+0.5}\Big].
\end{aligned}
\tag{2.57}
$$

Given the fields at a certain time step n, the $\vec{B}$ field at the next time step is found using Eq. (2.56) and the $\vec{E}$ using Eq. (2.57). Equations (2.56) and (2.57) represent the Yee scheme for numerical FDTD solution of Maxwell equations, one of the simplest schemes known.

It can be shown that the Yee scheme is stable for

$$\Delta t < \frac{1}{c\sqrt{1/\Delta x^2 + 1/\Delta y^2 + 1/\Delta z^2}}. \tag{2.58}$$

Eq. (2.58) is known as a Courant condition for stability of Yee scheme.

2.4.3 Equations of motion of markers along the characteristics

The trajectories of markers in the phase space are solved using a relativistic modification of the Boris scheme [117, 118].

As the initial value for the parameter s in Eq. (2.50) is arbitrary, the system of equations of motion of characteristics can be rewritten as follows:

$$\begin{aligned} \frac{\mathrm{d}\vec{r}}{\mathrm{d}t} &= \vec{v}, \\ \frac{\mathrm{d}\vec{p}}{\mathrm{d}t} &= q\big[\vec{E} + \frac{\vec{v}}{c} \times \vec{B}\big], \end{aligned} \tag{2.59}$$

where q is a charge of the given particle species, for example, charge of electron.

Eq. (2.59) is nothing but the equation of motion of a charged particle in an external electromagnetic field. For this reason, markers are sometimes called large particles, thus introducing a concept which is intuitively easier to understand. This concept, which results in the same algorithms, is, however, not used in this Thesis because it has some inherent difficulties such as rigid particles which are inconsistent with the theory of relativity.

Since $\vec{p} = m\vec{v}/\sqrt{1 - v^2/c^2}$, Eq. (2.59) is nonlinear. For this reason, solving a discretized equation of motion would require solving a nonlinear algebraic equation at every time step. Indeed, if the coordinate $\vec{r}$ of the marker is discretized at time step n whereas momentum is found at a shifted moment of

time, $n + 0.5$, the discretized equation of motion, having 2-nd order accuracy in time, takes the form

$$\begin{aligned}
&\frac{\vec{r}^{n+1} - \vec{r}^{n}}{\Delta t} = \frac{\vec{p}^{n+0.5}}{\gamma^{n+0.5}}, \\
&\frac{\vec{p}^{n+0.5} - \vec{p}^{n-0.5}}{\Delta t} = q\big[\vec{E}^{n} + \frac{\vec{p}^{n+0.5} + \vec{p}^{n-0.5}}{2\gamma^{n} mc} \times \vec{B}^{n}\big], \\
&\gamma^{n+0.5} = \sqrt{1 + (\vec{p}^{n+0.5}/mc)^2}, \\
&\gamma^{n} = \sqrt{1 + [(\vec{p}^{n+0.5} + \vec{p}^{n-0.5})/2mc]^2}.
\end{aligned} \tag{2.60}$$

Even if $\vec{B}^n$ was known at the n-th time step, which is not the case for the Yee scheme used, finding out $\vec{p}^{n+0.5}$ from $\vec{p}^{n-0.5}$ and $\vec{r}^{n}$ (second equation in 2.60) implies solving a nonlinear algebraic equation. This would make the markers motion step very computationally expensive. This problem is resolved in [117, 118] as follows.

First, the entire time step $\vec{p}^{n-0.5} \to \vec{p}^{n+0.5}$ is decomposed into half-time step acceleration in the electric field $\vec{E}^n$, subsequent rotation in the field $\vec{B}^n$ and the remaining half-time step acceleration in the field $\vec{E}^n$. As the fields depend only on coordinates and the coordinates do not change during rotation, this is a legitimate decomposition. The decomposed equation of motion is solved as follows. Let the momentum value after the first acceleration half-time step be $\vec{p}^{*}$ and after the rotation $\vec{p}^{**}$. The equation

$$\frac{\vec{p}^{*} - \vec{p}^{n-0.5}}{\Delta t/2} = q\vec{E}^{n} \tag{2.61}$$

is linear and is solved trivially. The subsequent rotation does not change the particle energy and therefore $\gamma^n = \gamma^* = \sqrt{1 + (\vec{p^*}/mc)^2}$. This value is

substituted into the rotation equation

$$\frac{\vec{p}^{**} - \vec{p}^{*}}{\Delta t} = q\frac{\vec{p}^{**} + \vec{p}^{*}}{2\gamma^{*}mc} \times \vec{B}^{n}. \tag{2.62}$$

Rewriting Eq. (2.62) in a more transparent form, one can obtain:

$$\vec{p}^{**} = \vec{p}^{*} + \alpha(\vec{p}^{*} \times \vec{B}^{n}) + \alpha(\vec{p}^{**} \times \vec{B}^{n}), \tag{2.63}$$

where $\alpha = q\Delta t/2\gamma^{*}mc$. Equation (2.63) is linear and has the following solution:

$$\vec{p}^{**} = \frac{A \cdot X}{1 + \alpha^2 \cdot (\vec{B}^{n})^2}, \tag{2.64}$$

where

$$\mathbf{A} = \begin{pmatrix} 1 + \alpha^2 B_x^{n2} & \alpha B_z^n + \alpha^2 B_x^n B_y^n & -\alpha B_y^n + \alpha^2 B_x^n B_z^n \\ -\alpha B_z^n + \alpha^2 B_x^n B_y^n & 1 + \alpha^2 B_y^{n2} & \alpha B_x^n + \alpha^2 B_y^n B_z^n \\ \alpha B_y^n + \alpha^2 B_x^n B_z^n & -\alpha B_x^n + \alpha^2 B_y^n B_z^n & 1 + \alpha^2 B_z^{n2} \end{pmatrix} \tag{2.65}$$

and

$$X = \vec{p}^{*} + \alpha\vec{p}^{*} \times \vec{B}^{n}. \tag{2.66}$$

The remaining half-step acceleration in the field $\vec{E}^{n}$

$$\frac{\vec{p}^{n+0.5} - \vec{p}^{**}}{\Delta t/2} = q\vec{E}^{n} \tag{2.67}$$

is solved trivially.

As was pointed out above, the Yee scheme does not give $\vec{B}^{n}$ but rather $\vec{B}^{n-0.5}$ or $\vec{B}^{n+0.5}$. However, it can be noted that Eq. (2.56) contains only $\vec{E}^{n}$ which is known from the previous time step. In principle, one could use (2.56) to find $\vec{B}^{n+0.5}$ and have an additional storage for $\vec{B}^{n}$ which is calculated as

$\vec{B}^n = (\vec{B}^{n+0.5} + \vec{B}^{n-0.5})/2$. However, as was proposed in [117], in practice, to avoid the extra storage requirement, $\vec{B}^n$ is calculated from a half-time step from $\vec{B}^{n-0.5}$ and $\vec{E}^n$. After the equations of motions of the markers are solved, the remaining half-time step is performed to find $\vec{B}^{n+0.5}$ from $\vec{B}^n$ and $\vec{E}^n$.

The described procedure allows one to avoid the solution to the nonlinear systems of equations for the markers at every time step and is second-order accurate in time.

The remaining unresolved complication is finding the values of fields at the markers positions. The field values are given at the mesh nodes and therefore are discrete. On the other hand, markers move, generally, between the mesh nodes where the fields are unknown. To find out the fields, one needs to use an interpolation of the values from the nodes into the space between them. In the SCPIC code, a method called PIC volume weighting is used. For 2D geometry, this method (which in this case called area weighting) is described in [119]. Since a 2D method explanation is more illustrative, it is given below. The 3D generalization, which was actually used in the code, is straightforward.

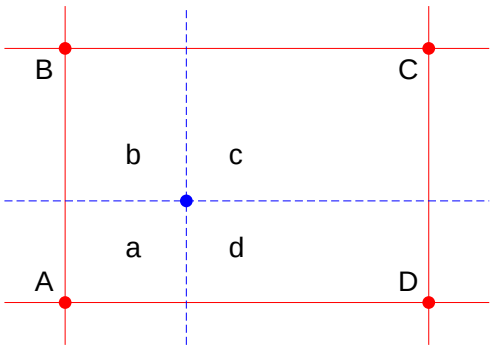

Figure 2.25: (Color) Illustration of the PIC area weighting method.

The area weighting interpolation method idea is depicted in Fig. 2.25. Let

the marker appear in the cell having vertices at nodes A, B, C and D. If lines parallel to the cell boundaries and passing through the marker are drawn, they divide the cell into four sub-cells having areas, correspondingly, a, b, c and d. If the sought function has values f_A, f_B, f_C and f_D on the nodes then, according to the area weighting method, the value of the function at the marker position is

$$f = \frac{f_A S_c + f_B S_d + f_C S_a + f_D S_b}{S_{cell}}, \tag{2.68}$$

where S_a, S_b, S_c and S_d are the area of the sub-cells shown in Fig. 2.25 and S_{cell} is the area of the entire cell.

2.4.4 Evaluation of currents

As was mentioned above, every marker is associated with a certain value of distribution function at $t = 0$. The value of the distribution function does not change along the trajectory of the marker in phase space, i.e., along the characteristic. In the general case of infinite number of characteristics, where no approximations are needed, the value of distribution function at any given point of the phase space is equal to the value associated with a marker appeared at this point, or to zero if no characteristics pass through this point.

In the SCPIC code, the currents are not evaluated directly from the distribution function. Rather, the charge density is calculated first and then the current density is found from the continuity equation

$$\frac{\partial \rho_\alpha}{\partial t} + \nabla \cdot \vec{J}_\alpha = 0. \tag{2.69}$$

Use of this algorithm ensures that the code conserves charges and no fictitious charges are generated due to inaccurate fulfillment of $\nabla \cdot \vec{E} = 4\pi\rho$, which is equivalent to Eq. (2.69).

The charge density ρ_α is proportional to the particle density n_α which in principle can be computed as

$$n_\alpha(\vec{r},t) = \int f_\alpha(\vec{r},\vec{p},t)\mathrm{d}^3p, \tag{2.70}$$

with function $f_\alpha(\vec{r},\vec{p},t)$ being equal to the value of the distribution function associated with the marker appearing at the point $(\vec{r},\vec{p})$ of the phase space at time t. However, since $f_\alpha = \mathrm{d}N_\alpha/\mathrm{d}^3r\mathrm{d}^3p$, an i-th marker is associated with a certain particle density in the phase space: $(f_\alpha)_i = \mathrm{d}(N_\alpha)_i/\mathrm{d}^3r\mathrm{d}^3p$. The total charge density of α-th species, in this way, can be calculated as

$$n_\alpha(\vec{r},t) = \sum_i \frac{\mathrm{d}N_{\alpha i}}{\mathrm{d}^3r} = \sum_i \mathrm{d}n_{\alpha i}, \tag{2.71}$$

where the summation is carried out over all the markers appearing at time t in the point of the real space having coordinates $\vec{r}$. The quantity

$$\mathrm{d}n_{\alpha i} = \frac{\mathrm{d}N_{\alpha i}}{\mathrm{d}^3r} = f_{\alpha i}\mathrm{d}^3p \tag{2.72}$$

is the particle density associated with every marker. It is infinitesimal in the case of a continuous characteristic distribution and can be finite in the discrete case.

In this way, every marker can be viewed as associated with a certain particle density $\mathrm{d}n_{\alpha i}$, and the total particle density at a particular point is the sum of all the densities associated with the markers located at that point. For this reason, one can operate only with the particle densities associated with the markers rather than with the distribution functions. The particle densities $\mathrm{d}n_{\alpha i}$ are calculated at $t = 0$ and used further to evaluate the particle density n_α at $t > 0$.

The method of extrapolation of a charge density, associated with a certain marker, onto the grid is similar to the PIC volume weighting method described above. For the geometry shown in Fig. 2.25, the value n_i at the marker position is extrapolated into the adjacent nodes as follows:

$$\begin{aligned} n_{Ai} &= n_i \frac{S_c}{S_{cell}}, \\ n_{Bi} &= n_i \frac{S_d}{S_{cell}}, \\ n_{Ci} &= n_i \frac{S_a}{S_{cell}}, \\ n_{Di} &= n_i \frac{S_b}{S_{cell}}. \end{aligned} \tag{2.73}$$

The total charge density at every node is the sum of the contributions from all the markers.

The evaluation of the current densities from the known charge density is most transparent in the 1D case. In this case, the continuity equation (2.69) simplifies to

$$\frac{\partial \rho_\alpha}{\partial t} + \frac{\partial J_{\alpha x}}{\partial x} = 0. \tag{2.74}$$

Below, for simplicity of notation, the index α is suppressed. If ρ is discretized at an unshifted time t^n and unshifted mesh nodes i, j, k, the discretized equation (2.74) has the form

$$\frac{\rho_i^{n+1} - \rho_i^n}{\Delta t} = -\frac{J_{i+0.5}^{n+0.5} - J_{i-0.5}^{n+0.5}}{\Delta x}, \tag{2.75}$$

where index x in J_x was also suppressed for simplicity. Eq. (2.75) can be rewritten as

$$J_{i+0.5}^{n+0.5} = J_{i-0.5}^{n+0.5} - \frac{\Delta x}{\Delta t}\left(\rho_i^{n+1} - \rho_i^n\right). \tag{2.76}$$

Equation (2.76) is a system of linear equations giving set of $J_{i+0.5}^{n+0.5}$ provided

ρ_i^n and $J_{-0.5}^{n+0.5}$ are known. Supposing that the marker is moving at distance $x > \Delta x/2$ from the boundary, it is safe to set $J_{-0.5}^{n+0.5} = 0$.

There are two possible cases: 1) both x^n and x^{n+1} are located within a single cell, say, between nodes i and $i+1$; and 2) both x^n and x^{n+1} are located inside different cells, i.e., the marker has jumped from one cell into another. It is easy to see that since the particle velocity is limited by c and the time step is constrained by the Courant condition (2.58), a marker can jump only into at most an adjacent cell during a single time step.

Let us illustrate the method by considering the first possibility. Application of the PIC extrapolation algorithm results in the following nonzero values of charge density

$$\begin{aligned}
\rho_i^n &= \frac{(i+1)\Delta x - x^n}{\Delta x}\rho_0, \\
\rho_i^{n+1} &= \frac{(i+1)\Delta x - x^{n+1}}{\Delta x}\rho_0, \\
\rho_{i+1}^n &= \frac{x^n - (i+1)\Delta x}{\Delta x}\rho_0, \\
\rho_{i+1}^{n+1} &= \frac{x^{n+1} - (i+1)\Delta x}{\Delta x}\rho_0,
\end{aligned} \tag{2.77}$$

where ρ_0 is the charge density associated with the marker. Substitution of Eq. (2.77) into the system (2.76) and solving it results in

$$\begin{aligned}
&J_{0.5}^{n+0.5} = 0, \\
&\dots \\
&J_{i-0.5}^{n+0.5} = 0, \\
&J_{i+0.5}^{n+0.5} = \frac{\Delta x}{\Delta t}\frac{x^{n+1} - x^n}{\Delta x}\rho_0 = \rho_0 v, \\
&J_{i+1.5}^{n+0.5} = \rho_0 v - \frac{\Delta x}{\Delta t}\frac{x^{n+1} - x^n}{\Delta x}\rho_0 = 0, \\
&\dots \\
&J_{i_{max}+0.5}^{n+0.5} = 0.
\end{aligned} \tag{2.78}$$

In this way, motion of a marker between nodes i and $i+1$ results in only nonzero current density at the current node $i+0.5$ and zero at all other nodes. The second possibility, moving of the marker in the two adjacent cells, results in the current density $\rho_0 v$ proportionally divided between the two cells depending on what part of the trajectory actually lies in the cell.

The derivation of a general 3D case is less transparent and involves considerable efforts. If a marker moves within a single cell having lower vertex with indices (i,j,k), the algorithm results in the following nonzero current densities:

$$\begin{aligned}
J_{x\,i+0.5,\,j,\,k}^{\,n+0.5} &= \rho_0 v_x \frac{(j+1)\Delta y - \overline{y}}{\Delta y} \cdot \frac{(k+1)\Delta z - \overline{z}}{\Delta z} + \\
&\quad \frac{1}{12}\rho_0 v_x \frac{(y^{n+1}-y^n)(z^{n+1}-z^n)}{\Delta y \Delta z}, \\
J_{x\,i+0.5,\,j+1,\,k}^{\,n+0.5} &= \rho_0 v_x \frac{\overline{y} - j\Delta y}{\Delta y} \cdot \frac{(k+1)\Delta z - \overline{z}}{\Delta z} - \\
&\quad \frac{1}{12}\rho_0 v_x \frac{(y^{n+1}-y^n)(z^{n+1}-z^n)}{\Delta y \Delta z}, \\
J_{x\,i+0.5,\,j,\,k+1}^{\,n+0.5} &= \rho_0 v_x \frac{(j+1)\Delta y - \overline{y}}{\Delta y} \cdot \frac{\overline{z} - k\Delta z}{\Delta z} - \\
&\quad \frac{1}{12}\rho_0 v_x \frac{(y^{n+1}-y^n)(z^{n+1}-z^n)}{\Delta y \Delta z}, \\
J_{x\,i+0.5,\,j+1,\,k+1}^{\,n+0.5} &= \rho_0 v_x \frac{\overline{y} - j\Delta y}{\Delta y} \cdot \frac{\overline{z} - k\Delta z}{\Delta z} + \\
&\quad \frac{1}{12}\rho_0 v_x \frac{(y^{n+1}-y^n)(z^{n+1}-z^n)}{\Delta y \Delta z},
\end{aligned} \tag{2.79}$$

$$
\begin{aligned}
J_{y_{i,\,j+0.5,\,k}}^{n+0.5} &= \rho_0 v_y \frac{(i+1)\Delta x - \overline{x}}{\Delta x} \cdot \frac{(k+1)\Delta z - \overline{z}}{\Delta z} + \\
&\quad \frac{1}{12}\rho_0 v_y \frac{(x^{n+1}-x^n)(z^{n+1}-z^n)}{\Delta x \Delta z}, \\
J_{y_{i+1,\,j+0.5,\,k}}^{n+0.5} &= \rho_0 v_y \frac{\overline{x} - i\Delta x}{\Delta x} \cdot \frac{(k+1)\Delta z - \overline{z}}{\Delta z} - \\
&\quad \frac{1}{12}\rho_0 v_y \frac{(x^{n+1}-x^n)(z^{n+1}-z^n)}{\Delta x \Delta z}, \\
J_{y_{i,\,j+0.5,\,k+1}}^{n+0.5} &= \rho_0 v_y \frac{(i+1)\Delta x - \overline{x}}{\Delta x} \cdot \frac{\overline{z} - k\Delta z}{\Delta z} - \\
&\quad \frac{1}{12}\rho_0 v_y \frac{(x^{n+1}-x^n)(z^{n+1}-z^n)}{\Delta x \Delta z}, \\
J_{y_{i+1,\,j+0.5,\,k+1}}^{n+0.5} &= \rho_0 v_y \frac{\overline{x} - i\Delta x}{\Delta x} \cdot \frac{\overline{z} - k\Delta z}{\Delta z} + \\
&\quad \frac{1}{12}\rho_0 v_y \frac{(x^{n+1}-x^n)(z^{n+1}-z^n)}{\Delta x \Delta z},
\end{aligned}
\tag{2.80}
$$

$$
\begin{aligned}
J_{z_{i,\,j,\,k+0.5}}^{n+0.5} &= \rho_0 v_z \frac{(i+1)\Delta x - \overline{x}}{\Delta x} \cdot \frac{(j+1)\Delta y - \overline{y}}{\Delta y} + \\
&\quad \frac{1}{12}\rho_0 v_z \frac{(x^{n+1}-x^n)(y^{n+1}-y^n)}{\Delta x \Delta y}, \\
J_{z_{i+1,\,j,\,k+0.5}}^{n+0.5} &= \rho_0 v_z \frac{\overline{x} - i\Delta x}{\Delta x} \cdot \frac{(j+1)\Delta y - \overline{y}}{\Delta y} - \\
&\quad \frac{1}{12}\rho_0 v_z \frac{(x^{n+1}-x^n)(y^{n+1}-y^n)}{\Delta x \Delta y}, \\
J_{z_{i,\,j+1,\,k+0.5}}^{n+0.5} &= \rho_0 v_z \frac{(i+1)\Delta x - \overline{x}}{\Delta x} \cdot \frac{\overline{y} - j\Delta y}{\Delta y} - \\
&\quad \frac{1}{12}\rho_0 v_z \frac{(x^{n+1}-x^n)(y^{n+1}-y^n)}{\Delta x \Delta y}, \\
J_{z_{i+1,\,j+1,\,k+0.5}}^{n+0.5} &= \rho_0 v_z \frac{\overline{x} - i\Delta x}{\Delta x} \cdot \frac{\overline{y} - j\Delta y}{\Delta y} + \\
&\quad \frac{1}{12}\rho_0 v_z \frac{(x^{n+1}-x^n)(y^{n+1}-y^n)}{\Delta x \Delta y},
\end{aligned}
\tag{2.81}
$$

where $v_x = (x^{n+1} - x^n)/\Delta t$, $v_y = (y^{n+1} - y^n)/\Delta t$, $v_z = (z^{n+1} - z^n)/\Delta t$, $\overline{x} = (x^{n+1} + x^n)/2$, $\overline{y} = (y^{n+1} + y^n)/2$ and $\overline{z} = (z^{n+1} + z^n)/2$. Equations (2.79) – (2.81) can be found in [120].

Multi-cell markers motions can be decomposed into the single-cell motions, with the proportional contribution into each of the cell. The total current density at each node is the sum of the contributions of every marker. The

algorithm given by Eqs. (2.79) – (2.81) ensures the continuity equation is fulfilled with the machine precision.

2.4.5 Boundary conditions for fields, markers and electromagnetic sources

The SCPIC code has three types of boundary conditions (BCs) for both fields and markers: periodic, reflecting and absorbing.

For markers, periodic boundary conditions are trivial: once a marker reaches a boundary it continues from the opposite side with unchanged velocity. The periodic BCs for fields is described by the fields in the ghost cells being equal to those near the opposite boundary.

In the case of reflecting BCs, the markers bounce back from a wall with reversed normal component of the velocity. The values of the field in the ghost cells are such that the following is ensured on the reflecting wall:

$$\begin{aligned} &E_n : continuous, \\ &E_\tau = 0, \\ &B_n = 0, \\ &B_\tau : continuous. \end{aligned} \tag{2.82}$$

In the case of absorbing BCs, markers stick to the boundary upon reaching it and just stop their motion. This inevitably leads to accumulation of static charges on the absorbing BCs. The field absorbing BCs are implemented using Mur's first order boundary conditions. This is a classical and the simplest possible algorithm for implementation of absorbing BCs. Its derivation can be found in [121].

For field excitation, a total field/scattered field (TFSF) method is used.

This method, which is described in great detail in [122], introduces a source into the computational domain which does not interact with the field reaching the source from the domain (i.e. with the field scattered from the plasma targets in the domain). The method needs an exact knowledge of the source fields in the vicinity of an excitation plane (interface). These fields must satisfy Maxwell equations. In the SCPIC code, the source fields used are those of a parabolic focusing mirror, calculated by the Stratton-Chu integrals using methods described in Section 2.2.

The SCPIC code was created using C programming language and parallelized using OpenMP extension of the language. Besides the described features, the code also has an ability to turn the simulation domain into a moving frame which can be used in calculations of propagation of short pulses in long plasmas.

2.5 Electron acceleration from micro- and nanotargets in a tightly focused laser

Using the SCPIC code, simulations of interaction between a focused laser and plasma targets were performed. The goal of the analysis given in this Section[4] is to understand the acceleration process and find optimal conditions for electron acceleration in interaction with the nano-scale targets. The nanotargets participating in the interaction serve as a source of the particles.

As a first step, a situation closely related to the test particle problem is considered: the interaction between a laser and a spherical nanotarget. A linearly polarized laser pulse of Gaussian shape (in time) with longitudinal

[4] A major part of the text in this Section was taken directly from the paper [68].

FWHM (full width at half maximum) length 9λ (λ is the laser wavelength) which is equivalent to the pulse duration ~ 30 fs for $\lambda = 1\,\mu$m, focused by a parabolic mirror, hits a cluster having center positioned off-axis in the focal plane. As an example, a focused plane wave will be considered. The electron plasma density of the spherical nanotarget is taken as $n = 100\,n_{cr}$, where n_{cr} is the critical electron density, $n_{cr} = m\omega/4\pi e$, where e is the electron charge and m is, as in previous section, its mass. The initial radius of the target is 50 nm and the wavelength of the laser is equal to 1 micron. The number of particles per cell (markers per mesh cell) used was 10^3. The mesh resolution was 33^3 cells per λ^3. The ion charge-to-mass ratio is equal to $e/3672m$. It was assumed that there is no preplasma that is relevant to the laser with a high intensity contrast ratio.

Figure 2.26a shows a cluster irradiated by a 120 TW laser focused by a parabolic mirror with $f_{\#} = 1$ into a spot of ~ 1 wavelength diameter. The laser pulse propagates in the direction of the x-axis and the laser polarization plane is XY. The position of the cluster in the focal plane is chosen consistent with the previous result of test particle simulations considered in the Section 2.3 to produce a relatively high final energy of the electrons.

After laser-cluster interaction, the accelerated electrons form a jet moving off from an exploding ion core. The jet possesses a fine structure, i.e. it consists of well separated narrow subwavelength-sized layers (bunches). A similar bunching of electrons was reported in previous theoretical studies [123, 124, 125]. So far, there has been no clear explanation of this phenomenon. Due to the simplicity of the numerical experiment arrangement considered in this Section, it was possible to give such an explanation which is presented below.

The simulations have demonstrated that the submicron bunches within the

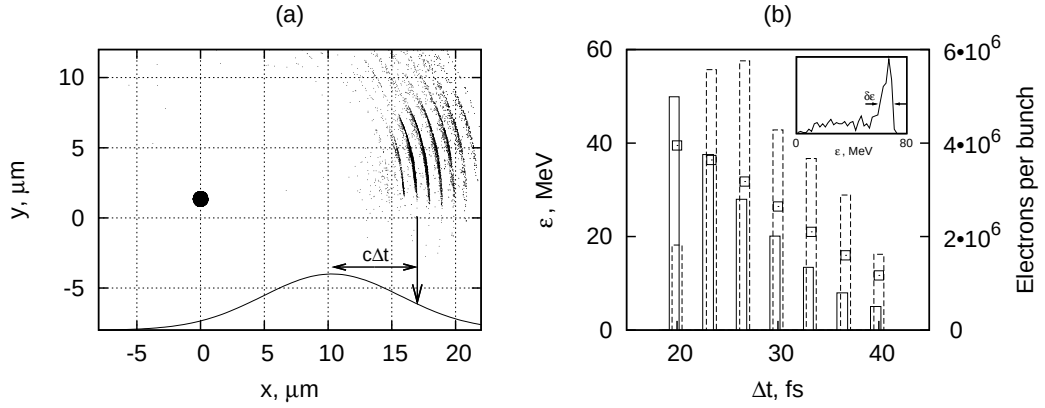

Figure 2.26: (a) Electron jet moving out from the Coulomb-exploding ion core after interaction between the laser and a spherical plasma target. Here, a projection of the 3D distribution of electrons ($15\mu\text{m} \lesssim x \lesssim 20\mu\text{m}$) and ions ($x \simeq 0$) onto the XY plane is shown for 33 fs after the pulse maximum reached the cluster. The laser is focused onto the origin. Initial position of the target center is: (0, 1.35, 0) μm. The curve at the bottom of the figure shows the position of the Gaussian envelope at this moment of time. (b) Average electron energies (solid line bars) and number of particles (dashed line bars) in the bunches for the instant corresponding to the panel (a) versus the time delay of the pulse maximum with respect to the bunches; estimation for the particles number per bunch given by Eq. (2.83) (open squares). The inset shows the spectrum of the electrons in the last (most energetic) bunch.

propagating electron jet (cf. Fig. 2.26a) are sequentially extracted from the cluster as the laser intensity at the cluster increases following the Gaussian shape. Every bunch starts to move out of the cluster at its own instant. The distance between the nearby bunches is one laser wavelength. It is instructive to show the typical energy of the electrons in each bunch as a function of the distance Δx between the bunch and the center of the laser pulse or the corresponding time shift $\Delta t = \Delta x/c$. This dependence is illustrated in Fig. 2.26b by the solid bars. The number of particles in every bunch is given by the dashed bars. The energies of electrons in the bunches increase with the bunch order number; the later the bunch appears, the higher its energy is. Certainly, this picture is typical for the early stage of electron motion as long as the faster bunches do not start to overtake the slower ones. In the case of relativistic

electrons whose velocities are close to the speed of light, this requires quite a long time. Simultaneously, the laser pulse overtakes the trapped electron jet, and far away from the cluster they both propagate independently.

Serial bunch production occurs at the instants when the laser field is high enough to extract electrons from the cluster, which attracts them back by the Coulomb force increasing in proportion as more and more electrons are removed. Increasing of laser intensity at the pulse leading edge provides the serial generation of the electron bunches. The electric field components of the laser at the position of the cluster center, during a laser period, in the vicinity of the top of the pulse (as example) are shown in Fig. 2.27a. The E_z

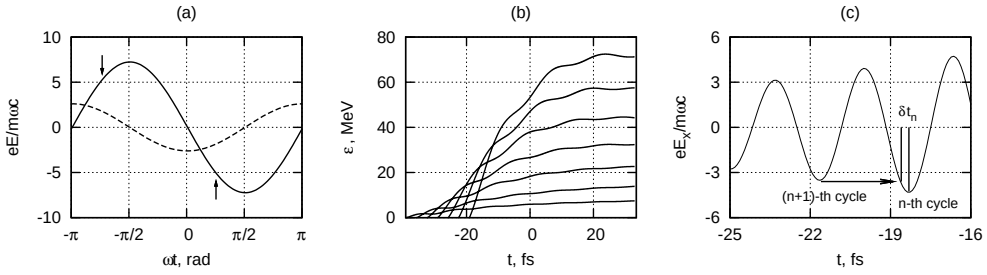

Figure 2.27: (a) Longitudinal (solid line) and transversal (dashed line) electric field components of the laser in the vicinity of the top of the pulse; (b) energy evolutions of the test particles started at different moments within the pulse; (c) the scheme showing how the bunch length is estimated.

component, not shown in Fig. 2.27a, is equal to zero. As the longitudinal component of the field is dominating (due to the tight focusing), in the following qualitative explanation it will be considered to be the only field component present. The electrons can start moving when the absolute value of the laser field exceeds the electrostatic field of the uncompensated positive charge of the cluster (due to the electrons extracted at the previous laser cycles). If the cycle is located at the leading edge of the wave envelope, the maximum of the laser field exceeds that of the previous cycle, which is approximately equal to the electrostatic field that can be estimated as the Coulomb field of

the cluster on its boundary. The instants when the electrons can be extracted from the cluster are schematically shown by the arrows in Fig. 2.27a. However, the particles started at the positive (first arrow) maximum of the field, move backwards (electrons have negative charge), enter the region of negative E_x, slow down, stop and return back to the cluster. The particles started at the negative (second arrow) maximum of the field co-propagate with the pulse in the accelerating phase and are effectively accelerated. For this reason, the bunches are separated by the distance $1\,\lambda$ (period of the E_x field component) from each other. The PIC simulations have indeed shown that the bunches corresponding to Fig. 2.26a have been extracted in the vicinities of the negative maxima of E_x. The particle extraction stops when the value of the field reaches maximum laser intensity, thus resulting in an asymmetric jet with the length less than or equal to half of the pulse length. In the case when the laser intensity is higher than that needed to extract all electrons, the jet size is shorter than the half of the pulse length.

To estimate the energies of the particles in the bunches, further test particle simulations were performed for a single particle starting its motion from the center of the cluster. A test particle (initially at rest) was prescribed to move at the moment when the magnitude of E_x at its position was equal to the maximum magnitude of E_x at the previous pulse cycle. That has allowed us to omit the electrostatic field because it strongly decreases with distance from the boundary of the cluster which size is much smaller than λ. The laser field is calculated by using Stratton-Chu integrals in the entire space. The energy evolutions of the test particles, started in different cycles are shown in Fig. 2.27b where the top of the pulse passes the center of the cluster at $t = 0$. The final energies of the electrons in Fig. 2.27b reproduce the trend given in Fig. 2.26b by the solid bars (the closer to the top of the pulse, the higher the

energy).

In this way, the electrostatic field of the uncompensated positive charge provides a mechanism of injection of the particles into the wave (cf. [66]). This mechanism, in principle, must also work in the case of a plane wave, with the only difference that the injecting force in that case would be the Lorentz force which should result in the distances between bunches being equal to the $\lambda/2$ (cf. [125]).

The number of particles ΔN in a single bunch can be estimated using a simple balance $\Delta E_x \approx \Delta E_c$, where ΔE_x is the difference between the field maxima in the two subsequent cycles of the pulse and $\Delta E_c = e\Delta N/R^2$ is the corresponding difference between the Coulomb field at the boundary of a cluster. This results in

$$\Delta N \approx \frac{\Delta E_x R^2}{e} = \Delta a_x \cdot \frac{2\pi m c^2 R^2}{\lambda e^2}, \tag{2.83}$$

where Δa_x is the difference between the maximum values of dimensionless x-component of the laser electric field in the two subsequent cycles of the pulse. The resulting estimation of the electron numbers is given by the open boxes in Fig. 2.26b. Certainly, Eq. (2.83) can significantly overestimate the number of particles in the last most energetic bunch in the case where laser intensity is high enough to extract all the electrons before the laser pulse maximum reaches the cluster. This is because the last bunch contains only the remaining electrons (all cluster electrons minus electrons from all previous bunches). This estimation also somewhat underestimates the number of particles in all the bunches due to the nonzero E_y field component and Lorentz force which have not been taken into account. However, this approximation gives the correct order of magnitude and therefore correctly describes the physics of electron

injection.

Equation (2.83) suggests a way of maximizing the number of particles in a bunch; the steeper the pulse shape, the higher the number of extracted electrons. In this way, a high intensity ultra-short laser pulse would be able to extract all the particles in just few bunches thus maximizing the number of electrons per bunch. On the other hand, a long envelope would produce many bunches with fewer number of particles in each of them and smaller bunch size. The latter is due to a decrease of the duration of electron injection which happens because the maxima between the subsequent cycles become closer to each other (see Fig. 2.27c).

The length of every bunch can be estimated if one takes into account that the electron extraction stops at the negative maximum of the field in the given laser cycle. Let the pulse envelope have form $a(x,t) = a_0 \exp[-(x/c-t)^2/\Delta T^2]$, where ΔT is the pulse duration and a_0 is the pulse maximum dimensionless amplitude. Then, if n is the number of bunch, its length δt_n satisfies $\cos(2\pi\delta t_n/T) = E_{x\,n+1}/E_{x\,n}$ (see Fig. 2.27c), where $E_{x\,n}$ is the negative maximum of the x field component in the n-th cycle, and can be estimated as

$$\delta t_n = \frac{T}{2\pi} \arccos\left(\frac{\exp[-(nT/\Delta T)^2]}{\exp[-((n-1)T/\Delta T)^2]}\right), \tag{2.84}$$

where T is the laser wave period.

If the pulse is long ($\Delta T \gg T$) then not too far from its top, $\cos(2\pi\delta t_n/T) \approx 1 - (2\pi\delta t_n/T)^2/2$, and

$$\delta t_n \approx \frac{T}{2\pi}\sqrt{2\,\frac{E_{x\,n} - E_{x\,n+1}}{E_{x\,n}}} \approx \frac{T}{\pi}\sqrt{\frac{T}{2}\,\frac{\partial \ln a}{\partial t}}\,. \tag{2.85}$$

The bunch length is minimum if extracted at the top of the pulse ($\delta t_1 = T\exp[-(T/\Delta T)^2]/2\pi$) and approaches $T/4$ for the bunches generated by the

pulse wing ($n \to \infty$).

The final energy of the electron depends on the laser phase at which the particle starts to move; the interval of phases allowing extraction of the particles from the cluster (located between the second arrow and negative maximum of E_x in Fig. 2.27a) defines the spectrum thickness shown as $\delta\varepsilon$ in the inset of Fig. 2.26b. This interval slightly depends on the number of the bunch. From the test particle simulations, the approximate scalings for the maximum energy $(\varepsilon_{max})_n$ and energy spread $\delta\varepsilon_n$ in the n-th bunch were found:

$$\begin{aligned} (\varepsilon_{max})_n &\approx 120\sqrt{I_n/I_0}\,\mathrm{MeV}\,, \\ \delta\varepsilon_n &\approx [28 - 40(I_n/I_0 - 0.75)^2]\,\mathrm{MeV}\,, \end{aligned} \tag{2.86}$$

where I_n is the intensity in the n-th (from top to bottom of a pulse) cycle of the laser and I_0 is the intensity at the top of the laser. For the bunches in Fig. 2.26, n ranges from 6 (most energetic bunch) to 12.

The first scaling in Eq. (2.86) reflects the approximate proportionality of the particles energy to the laser field which is consistent with the mechanism of particle acceleration in the diverging laser field discussed in Sec. 2.3. The second scaling is just a numerical approximation to a more sophisticated dependence; it, however, demonstrates that the electrons in a single bunch are rather monoenergetic (with the best $\delta\varepsilon/\varepsilon < 20\%$ in the vicinity of the top of the pulse). The inset in Fig. 2.26b shows an example of such monoenergetic spectrum.

The described mechanism also works with more complicated targets, for both focused plane wave and a focused Gaussian beam. An example of interaction of an $f/1$-focused laser with an ultrathin foil target is given in Fig. 2.28.

In Fig. 2.28, as before, the laser power, focused by an $f/1$ mirror was taken

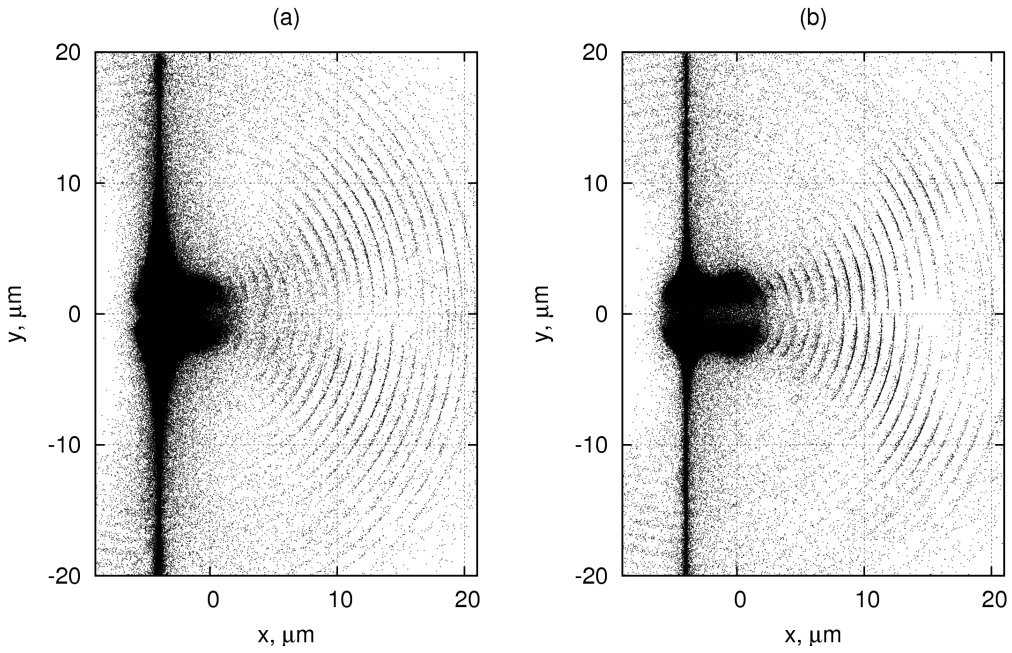

Figure 2.28: A snapshot of particles accelerated by the plane wave (a) and a Gaussian beam (b), incident onto an f/1 parabolic mirror. Only electrons with $-\lambda/2 \leq z \leq \lambda/2$ are shown. The foil position is given by $\Delta x = -4\,\lambda$ from the best focus.

to be 120 TW, with the wavelength $\lambda = 1\,\mu$m and pulse length 30 fs. The laser polarization plane is XY and the propagation direction is OX. The foil having thickness of 100 nm is composed of plasma with electron density $100\,n_{cr}$. As before, the ion charge-to-mass ratio is 3672. The number of particles per cell used was 10^2 and the mesh resolution 33^3 cells per λ^3.

As can be seen from Fig. 2.28, interaction of both focused plane wave and focused Gaussian beam with the foil can produce bunched electron jets, consisting of attosecond bunches. The distance between the jets is equal to λ in the half-spaces $y > 0$ and $y < 0$. At the same time, the jet bunches in $y > 0$ or $y < 0$ half-spaces are shifted by $\lambda/2$ in the x direction with respect to each other. The mechanism of particle extraction is similar to that described above, with the only difference that the electrons are extracted by either E_x or

E_y field components, whichever is dominant at the point of extraction. When it is said that the bunch is extracted by the E_y field component, it is implied that the E_y field pushes the particle in y direction which immediately gives rise to the Lorentz force extracting the electrons from the foil.

The parameters of jets extracted from the foil appeared to depend considerably on the distance Δx between the center of the foil and the best focus position and on the mirror f-number. The maximal number of high-energy electrons is produced by the foil located in the best focus position.

Figure 2.29 shows angular dependencies of the electrons deposited on the right wall of the simulation box. In Fig. 2.29, θ is defined as an angle between the particle momentum and OX axis. All the displaced foil positions appearing in Fig. 2.29 for plane wave incident onto the focusing mirror are shifted in the $-x$ direction within the Rayleigh length. It can be seen that there is a considerable difference between the number of particles extracted from the foils having different displacements with respect to the focus, especially for the $f_{\#} = 1$ case. The angular distributions in Fig. 2.29 are integrated over time and the azimuthal angle.

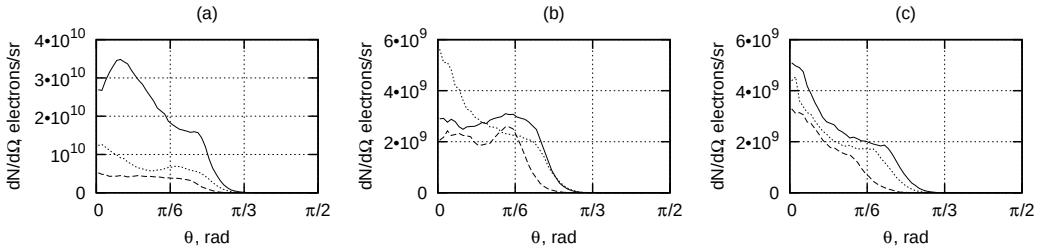

Figure 2.29: Angular distributions of the electrons accelerated by a laser beam focused by an $f/1$ (a), $f/2$ (b) and $f/3$ (c) parabolic mirrors. Solid line: focused plane wave, $\Delta x = 0$; dotted line: focused Gaussian beam, $\Delta x = 0$; dashed line: focused plane wave, $\Delta x = -4\,\lambda$ (for $f_{\#} = 1$), $\Delta x = -9\,\lambda$ (for $f_{\#} = 2$), $\Delta x = -20\,\lambda$ (for $f_{\#} = 3$).

Increasing the mirror f-number results in a several times decrease in the

number of electrons extracted from the target, both in the case of plane wave and the Gaussian beam incident onto the mirror. In this way, the main parameter responsible for the number of extracted particles is the intensity in the focus rather than the power. Therefore, unlike the free particle results discussed above, it does make sense to focus the laser pulse most tightly. The electron jet production by a focused Gaussian beam is somewhat less effective than that by the focused plane wave.

Let us discuss now the particles energy spectra. Figure 2.30a shows the spectra of electrons moving inside a solid angle of $4\pi/1000$ sr (that is equivalent to a cone having full base angle 7°) in the direction of the maximum density of the electron jet. All the four spectra corresponding to different laser beams possess flattened and banded tails. The highest energy and number of particles are for the plane wave focused by an $f/1$ mirror. An estimation for the number of particles gives the total charge ~ 250 pC in the beam propagating within the specified solid angle of $4\pi/1000$ sr for this $f/1$ case. The energy spectrum of these particles is quasi-monoenergetic. It was confirmed that the jets density is a maximum in the laser polarization plane passing through the best focus of the mirror.

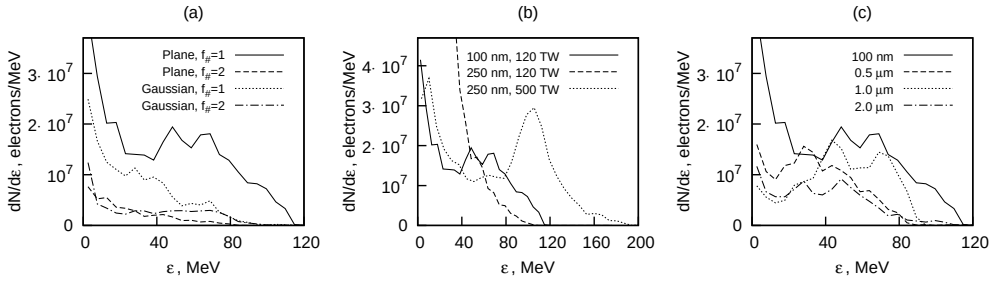

Figure 2.30: Spectra of electrons moving inside the solid angle $\Delta\Omega = 4\pi/1000$ sr in the direction of the maximum density of the electron jet: (a) 120 TW laser, 100 nm foil, various f-numbers and types of laser pulses incident onto the focusing mirror; (b) plane wave beam incident onto the $f/1$-mirror, various foil thickness or laser power; (c) 120 TW plane wave focused by an $f/1$-mirror, 100 nm foil pre-expanded to various thicknesses.

It is of some interest to consider interaction with a thicker foil. Figure 2.30b shows spectra of jet electrons accelerated from the 100 nm- and 250 nm-thick foils, correspondingly (solid and dashed lines). As the foil thickness increases from 100 nm to 250 nm, the particles become less monoenergetic. The number of energetic ($\varepsilon > 60$ MeV) electrons also decreases whereas the number of low-energetic particles greatly increases with the foil thickness. Note, that in the case of completely removed electrons from the 100 nm-thick foil having charge density $100\,n_{cr}$ ($1.11 \cdot 10^{23}\mathrm{cm}^{-3}$ for the laser wavelength $\lambda = 1\mu\mathrm{m}$), the remaining ions will cause an electrostatic field at the surface having magnitude approximately equal to the E_x component of the laser field. If the laser intensity is increased ~ 4 times (Fig. 2.30b, dotted line), the spectrum again becomes monoenergetic, with the energies of electrons increased ~ 2 times. This indicates that the main mechanism of acceleration is CAS which scales as square root of the laser power (cf. Sec. 2.3).

Due to unlimited electron supply of the focal domain from the foil, the jet length for transversally unbounded foil is equal to the length of the laser envelope (Fig. 2.28). As the angles between the electrons in the bunches are not entirely equal, the bunches diverge. This results in the electron density in the bunch decreasing with distance from the foil as $\sim 1/r^2$. The measurement of the electron density per bunch results in values up to $\sim 1\,n_{cr}$ at the distance $\sim 10\lambda$ from the foil.

Let us now consider the type of targets which might be more feasible as a practical matter than the ultrathin foils discussed above. This is a plasma slab having charge density profile

$$n(x, y, z) = n_0 \exp\big[-\big(\frac{x}{\Delta x}\big)^2\big], \tag{2.87}$$

where Δx is the thickness of the plasma slab. Such a density distribution may result from interaction between a foil and the laser prepulse which can be either natural or a controlled prepulse. For convenient comparison with a nondecayed foil, let us consider the slabs with different thicknesses having the same number of particles as the 100-nm ultrathin foil discussed above, having $\Delta x = 0$. Such a comparison is given in Fig. 2.30c.

All of the spectra shown in Fig. 2.30c can be considered as quasi-monoenergetic and, in fact, do not differ from each other considerably until a slab thickness is much smaller than the Rayleigh length. The main difference is some decrease of the number of accelerated particles with thickness. For this reason, it can be concluded that interaction of the foil with the prepulse does not considerably worsen the properties of accelerated electrons if the resulting plasma size is of the order one laser wavelength. The higher preplasma size can result in appearance of Maxwellian tails (cf. Fig. 2.30c, dash-dotted line, for the $2\,\lambda$ plasma size, for $\varepsilon > 60$ MeV). However, even for this case, the electrons are extracted from the plasma in the form of jets consisting of subwavelegth-sized bunches.

It is instructive to discuss an oblique incidence of the laser pulse. As an example, let us consider a p-polarized plane wave focused by an $f/1$ mirror. The resulting charge density pattern in plane $z = 0$ for the case of 30° incidence angle is shown in Fig. 2.31a. The p-polarized oblique incidence results in an asymmetric jet pattern; one jet appears suppressed and another has a higher charge density within it. The electron energy spectra for 15, 30 and 45 degrees angle of laser incidence are given in Fig. 2.31b where the spectrum of normal incidence is given by the solid line for reference. One can conclude that, at first, the p-polarized oblique laser incidence can produce more energetic particles than the normal one, and, secondly, there is an optimal angle of incidence

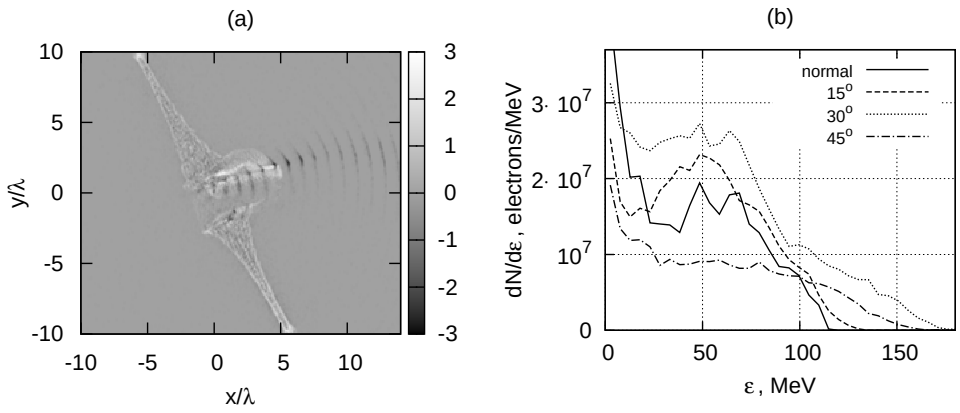

Figure 2.31: (a) Plasma charge densitiy, in units of en_{cr}, in the plane $z = 0$ of plasma for 30° p-polarized laser incidence. (b) Electrons spectra in the solid angle $\Delta\Omega = 4\pi/1000$ sr in the direction of the maximum density of the electron jet for different laser incidence angles and p-polarization.

resulting in the best quality electrons. For the chosen parameters of foil and laser, this optimal angle is $\sim 30°$. The number of electrons in the solid angle $4\pi/1000$ which corresponds to the densest part of the jet is $\sim 2 \cdot 10^9$. Given the energy in the peak $\sim 50\,\mathrm{MeV}$, this corresponds to the laser-to-particle energy conversion factor $> 0.5\%$. Oblique incidence of a p-polarized laser pulse results in an enhanced longitudinal electric field component which efficiently accelerates electrons. The larger the angle of incidence, the stronger this component. However, for large enough angles of incidence both laser intensity at the target and target transparency become low and electrons cannot be accelerated efficiently any more. This results in non-monotonic dependence of the electron energy spectra (Fig. 2.31) on the angle of incidence. For the case of s-polarized light, it was found that the oblique incidence does not produce improvement in the electron spectra, with the jets structure being symmetrical as in the case of normal laser incidence.

2.6 Conclusion

In this Chapter, a dynamics of electrons in a relativistically strong tightly focused laser was discussed. First, a problem of finding the exact fields of a parabolic mirror-focused laser field was solved numerically using analytical methods developed in [109] and employed previously in [106], [108] and [63]. The structure of the resulting fields was discussed in detail. It was shown that the expressions (2.26) approach the solutions of Maxwell equations for mirror radius much larger than the laser wavelength. In the calculations, the radius was taken large enough for the discrepancy from the exact solution to the Maxwell equations to be negligible.

The field of a parabolic mirror was used in the equations of motion of a free charged particle. These equations were solved numerically. It was found that the particle can be accelerated by means of two mechanisms or their combination. The first mechanism, focal spot acceleration, deals with the plane wave-like interaction between the particle and field at the leading edge of the pulse inside the focal spot. Upon reaching high energy, the particle escapes the hot spot and does not loose its energy due to slowing down in the trailing edge of the pulse as would happen in the interaction with a plane wave. This is the kind of interaction which one would intuitively expect. The second mechanism, CAS, which was found previously for the case of injected relativistic particles in [99, 98], deals with synchronization between the particle and the field and slow acceleration in a constant phase of the diverging laser. A simple 1D model of CAS was proposed giving intuitive explanation of the process.

An energy map, i.e., dependence of the phase-averaged asymptotic energy of the particle on its initial position, has demonstrated high spatial inhomo-

geneity of the energy acquired by the particles. The energy maps created for different f-numbers have allowed us to find the maximum energy which a particle can reach for the given laser parameters. The maximum energy scales as a sum of a function linear in laser power and the one proportional to the square root of it. The CAS-accelerated particle energy scales as $\sqrt{P}$, where P is the laser power.

The structure of the focused laser depends on that of the incident field on the parabolic mirror. Two kinds of incident laser were discussed: pure plane wave and a Gaussian beam of a large radius having a macroscopic scale. In the case of a Gaussian beam incident onto the mirror, the resulting structure is close to that of a Gaussian paraxial beam. It was found that it is safe to use the 1-st order paraxial approximation (2.22) in the problems of particle acceleration by a focused Gaussian beam for any $w_0 \gtrsim 2\,\lambda$ and the 5-th order paraxial approximation (2.44), (2.45) for $w_0 \gtrsim 1\,\lambda$ since the resulting error in acquired kinetic energy due to inaccuracy of the field lies within few percents.

To study the interaction between the focused laser and more realistic targets than free particles, a 3D relativistic electromagnetic PIC code SCPIC was created. The code uses standard numerical methods. A unique ability of the SCPIC code is employing the fields of a focused laser described by expressions (2.26) as boundary conditions for the field sources. These sources were used in studies of interaction with spherical nano-plasmas and ultrathin foils. It was shown that the tightly focused laser can extract bunches of attosecond durations from the targets. A simple and intuitive model of bunch generation was proposed dealing with interplay between the laser field and electrostatic field of a partially evacuated target. The model has provided estimation of bunch length and particle energy which matched the results of PIC simulations within a factor of 2. The PIC simulations of interaction with ultrathin

foils, for both normal and oblique incidence of laser and with pre-expanded foils have demonstrated extraction of electron bunches with the total charge in all the bunches being as high as few tens nanoCoulombs per steradian in the densest part of accelerated electron pattern. The electron energy from the plasma targets scales approximately as $\sqrt{P}$.

All the calculations in this Chapter were performed for laser powers within abilities of currently existing or next generation systems and can be verified experimentally.

Chapter 3

Expansion of spherical nanoplasmas into vacuum

3.1 Plasma expansion as a source of accelerated ions

As mentioned in Chapter 1, a common way to accelerate ions is to create a charge separation between electrons and ions by means of laser heating of electrons. During this process, a laser is shined onto the surface of a target, such as foil, microdroplet or an atomic cluster. The target, or its part interacting with the laser, is usually ionized at the very beginning of the pulse leading edge while the rest of the laser pulse interacts with the resulting plasma. The light electrons acquire a certain energy in this process and start to escape the target. This process continues until the potential energy of the electrostatic field of the remaining unbalanced positive charge of the target ions is equal to the kinetic energy of the escaping electrons. Whether the laser pulse is short or long, the electrostatic field of charge separation persists. On a longer time scale, the charge separation field accelerates the ions from the target. A

description of the ions dynamics is one of the goals of this Chapter.

A full-scale study of laser-plasma interaction with nanotargets requires considerable computational efforts (cf. [126, 127]). Furthermore, due to the complexity of the models used, the full-scale study does not show the physical behavior of accelerating particles in simple terms.

In the many papers discussing the laser-driven acceleration of ions, a number of simpler models are used. The laser is usually not considered at all. Instead, the electrons are prescribed to have a certain distribution function at $t = 0$ which is believed to be a result of interaction with a laser. The ions are usually considered immovable at $t = 0$. At $t > 0$, the plasma evolution is determined, depending on the particular plasma expansion model used. The models can be either hydrodynamical or kinetic and may or may not assume a thermodynamical equilibrium for the electrons. The hydrodynamical models use assumptions, such as isothermal, adiabatic or, more generally, polytropic equation of state for hydrodynamical closure. Finally, the expansion can be considered in limiting cases such as quasi-neutral expansion or, in the other limit, a Coulomb explosion of the target.

Historically, the first theoretical studies of plasma expansion into vacuum began more than forty years ago starting with [70]. The first approaches have been exploiting a hydrodynamic model of quasi-neutral expansion and self-similar solutions for semi-infinite plasmas in planar geometry [70, 72, 128, 129, 130, 131, 132, 133, 134, 135, 136]. The hydro-model was also extended to the case of spherical geometry and mass-limited targets [73] in the context of particular interest to inertial confinement fusion. In most of the hydrodynamical models, in order to provide the hydrodynamical closure, authors have assumed isothermal [70, 73, 128, 129, 130, 132, 133, 134, 136] electrons and cold ions. The isothermal electrons are supposed to describe interaction of a long laser

pulse with plasma, with the laser being an infinite reservoir of energy keeping temperature constant. For reference, a derivation of self-similar solution to the hydrodynamic equations of isothermal equilibrium plasma expansion is presented in Appendix B.1. For a special form of boundary conditions, the quasi-neutral hydrodynamical model with isothermal electrons has allowed an exact solution for the Cauchy problem [71].

More complicated models [135, 137] use polytropic equation of state for electrons, $p_e = kn_e^\gamma$, where p_e is the hydrodynamic pressure of electrons and γ polytropic index. A particular case of adiabatic electrons ($\gamma = 5/3$ for monatomic gas) can describe interaction of short laser pulses with plasma. To account for non-equilibrium effects, several authors have also used a simplified kinetic description of electrons [72, 131].

The quasi-neutral expansion of plasma takes place when the scale length of plasma inhomogeneity is much larger than the electron Debye length. In principle, this is usually the case at later stages of plasma expansion unless the temperature of electrons is comparable to the Coulomb energy of the ion core. However, at earlier stages of expansion or for large electronic temperatures the charge separation effects may be important. In the early papers these effects were accounted through numerical modeling [73, 133, 134, 135, 138, 139]. The charge separation effects were included into the hydrodynamical model in more recent papers [140, 141]. The paper [140] has employed an interpolation formula for an unknown characteristic of expansion taken from a Lagrangian code, whereas the authors of [141] have found a self-similar solution for a certain value of the electrons polytropic index.

From the beginning of systematic studies of plasma expansion and fast ion generation, the hydrodynamic models have faced difficulties in describing wavebreaking and subsequent multistream ion motion. This was first pre-

dicted to occur in a plasma with two electron species (hot and cold) [128, 129, 130, 136]. Only a kinetic approach can describe this multistream motion adequately. This was demonstrated, for example, in [142] where the authors have numerically solved kinetic equations for a 1D planar plasma configuration and found stable multi-layered structures resulting from the multistream motion.

For this reason, in the late 1990-s – early 2000-s, a number of analytical works have concentrated on the kinetic approach. A particular self-similar solution to Vlasov kinetic equations for electrons and ions for quasi-neutral adiabatic plasma expansion in 1D, 2D, or 3D symmetric case was found in [143]. Later there was found a more general (than in [143]) class of solutions to the initial-value problem for the Vlasov equations for arbitrary initial particle velocity distributions that was achieved by using the renormalization-group approach [144, 145, 146].

The opposite limiting case, the Coulomb explosion, was kinetically analyzed in a number of papers [76, 77, 146, 147], where appearance of singularities resulting from multi flows taking place for inhomogeneous initial plasmas was reported. These singularities were also referred as "collisionless shocks". There is a number of papers presenting PIC simulations of laser-plasma interactions proving that such regime can be realized in practice [148, 149, 150, 151].

The most complicated theoretical study is the kinetic problem of plasma expansion in the intermediate regime, neither quasineutral not CE, with strong charge separation effects. For plane geometry this regime is often referred as Target Normal Sheath Acceleration (TNSA) [78] where, at the plasma-vacuum interface, electrons create a strong sheath electrostatic field, which accelerates ions to high energies. A number of hybrid models were proposed [75, 152] in this context with fully kinetic ions and a simplified description for electrons.

In this Thesis, a particular case of expansion of a spherically symmetric

plasma into vacuum is considered. Physically, it may address an interaction of a laser with spherical nano-clusters. The plasma is described kinetically with a Maxwellian distribution function of electrons and all the ions motionless at $t = 0$. At $t > 0$ a Vlasov equation of collisionless plasma evolution is solved numerically using the particle simulation approach in the different regimes, starting from the quasineutral, passing the charge separation regime and finishing with the CE.

Due to motion of accelerated ions in the 4π solid angle, their applicability is limited. However, there are certain nuclear reactions which can be carried out between the ions [18]. To maximize their cross-section, it is desirable that the ions be monoenergetic.

Typically, the energy spectra of the ions accelerated by the plasma expansion is rather broad and terminates with an abrupt upper cutoff. However, it is known that monoenergetic ions can be produced from microplasmas composed of heavy and light ions [74, 153]. The most straightforward way is generation of high-quality light ion beams from the double layer targets, irradiated by ultraintense laser pulses [79, 154, 155]. In this scheme the first layer, at the foil front, consists of high-Z atoms, while the second (rear) layer is a thin coating of low-Z atoms. The coated thin layer detaches from the foil and moves as a whole out of the foil which acts on it as electrostatic pusher. A similar scheme was proposed in Ref. [156] for a spherical target composed of high-Z core and a thin shell of light ions. As before, the heavy ions create a strong radial electric field which acts as a Coulomb piston onto the light ions and effectively accelerates them.

The quasi-monoenergetic spectra of light ions were reported also for homogeneous multi-species targets for which the light species is distributed uniformly inside the target [21, 127, 157, 158, 159]. Ions with monoenergetic

features is a result of light ion acceleration at the heavy ion front that was clearly demonstrated in semi-analytical BVP (Boltzmann – Vlasov – Poisson) model for expanding multispecies plasmas with strong charge separation field, dealing with the planar geometry [75]. Similarly, the effect of light ion acceleration at the heavy ion front was derived in the analytical approach of adiabatic expansion of quasi-neutral plasma bunch where the spectrum of light ions possesses a narrow band structure [144]. Vlasov simulations of adiabatic expansion of a two ion species 1D plasma slab with charge separation field have demonstrated that the electrostatic shock at the heavy ion front gives rise to a peak in the light ion energy spectrum [154].

Spherical geometry of the homogeneous multi-species targets results in a more monoenergetic spectrum of light ions as compared to the expansion in the planar geometry (cf., for expample, [75] and [21]). The case of acceleration of impurity light ions in the spherical geometry was considered analytically in the recent papers [160] and [161] for, correspondingly, Coulomb explosion and self-similar charge separation driven expansion of a uniformly distributed plasma target. A more general case of a finite light ions concentration was studied numerically in [81] and [82] where formation of a mono-energetic spectrum was demonstrated for a wide range of electron temperatures and light ion concentrations. In this Thesis, the results of [81] and [82] are summarized and generalized.

3.2 Electrostatic gridless spherical particle code

It is possible, in principle, to run the 3D electromagnetic code described in the section 2.4, either with the laser or without it, with a certain initial distribution function of electrons and ions. However, since the problem in question is multi-

parametric, its study in this case would require many expensive computations which cannot be afforded.

For modeling of the spherical plasma expansion, a 1D electrostatic gridless spherical particle code was created. This code numerically solves a spherically-symmetric expansion of, generally, multi-species plasma into vacuum.

As commented in Sec. 2.4, the characteristics of the Vlasov equation for a collisionless plasma formally coincide with those of a free particle in an external field (2.59). One can write the equations (2.59) in a spherical coordinate system. As shown in Appendix B.2, the equations for $r(t)$ and $v_r(t)$ in the new coordinates in the non-relativistic limit are

$$\begin{aligned} \frac{\mathrm{d}r}{\mathrm{d}t} &= v_r, \\ \frac{\mathrm{d}v_r}{\mathrm{d}t} &= \frac{q}{m}E_r + \frac{1}{r^3}\frac{l^2}{m^2}, \end{aligned} \tag{3.1}$$

with certain equations for θ, φ, v_θ and v_φ, which are of no interest for the reasons clarified below. In Eq. (3.1), E_r is the radial component of the electrostatic field, magnetic field was neglected, and l^2 is the square of angular momentum:

$$\vec{l} = m\vec{r} \times \vec{v} = \vec{l}_0, \tag{3.2}$$

where $\vec{l}_0$ is the value of angular momentum at $t = 0$. In the present case of a purely central potential and field $\vec{E} = \hat{r}E_r(r,t)$, with no external fields, the angular momentum is conserved.

Equations (3.1 – 3.2) define the behavior of r-th and v_r-th coordinates of a characteristic of the Vlasov equation started at $t = 0$ from a point ($\vec{r}_0$, $\vec{p}_0 = m\vec{v}_0$) in phase space, such that $\vec{l}_0 = \vec{r}_0 \times \vec{p}_0$. In principle, to evaluate the distribution function at any point of the 6D space, one needs to solve four other equations for θ, φ, v_θ and v_φ. However, it is easy to see that since the

angular momentum is an integral of motion, the velocities v_θ and v_φ are in fact dependent on v_r. Indeed, the square of the total particle velocity $\vec{v}$ is

$$v^2 = v^2(\cos^2\alpha + \sin^2\alpha) = v_r^2 + \frac{1}{r^2} r^2 v^2 \sin^2\alpha = v_r^2 + \frac{1}{r^2}\frac{l^2}{m^2}, \qquad (3.3)$$

where α is an angle between $\vec{v}$ and $\vec{r}$ of the particle. In this argumentation, the term "particle" is used due to the formal coincidence between the equations of characteristics and equations of motion of a material point.

Equation (3.3) says that if v_r^2 is known, v^2 is automatically specified. On the other hand, due to conservation of $\vec{l}$, the particle velocity must stay in a certain plane defined by vectors $\vec{r_0}$ and $\vec{v_0}$. This gives the second restriction, defining the components of $\vec{v}$. In this way, v_θ and v_φ depend on v_r and can be calculated from it.

Due to the spherical symmetry, the distribution function does not depend on coordinates θ and φ. Therefore, knowledge of r of the characteristic is sufficient to know the distribution function at any θ and φ for the given r.

In view of the above argumentation, given the spherical symmetry, the 1D system of equations (3.1) completely describes the 3D evolution of plasma for any initial distribution function provided the last possesses spherical symmetry in the real space and a way to calculate the static field E_r is known.

Let us imagine a characteristic started at $t = 0$ from a point $(r_0, \theta_0, \varphi_0)$ with certain values of v_{r0} and l^2. At a moment $t > 0$, the characteristic will appear at another point in space (r, θ, φ) and will have a certain value of v_r. Due to the spherical symmetry, the values of r and v_r do not depend on θ_0 and φ_0 if l^2 is fixed. Furthermore, the characteristics are uniformly distributed over the surface of the sphere with radius r for any r in this case. Therefore, every characteristic can be associated with a hollow sphere carrying a certain

charge $\mathrm{d}dq_\alpha = q\mathrm{d}N_\alpha = qf_{\alpha 0}\mathrm{d}^3r\mathrm{d}^3v$ with it, where α is the index of the given species, $f_{\alpha 0}$ is the value of α-th distribution function at the starting point of the characteristic, q is the total charge of the given plasma component and $\mathrm{d}^3r\mathrm{d}^3v$ is an element of phase space. In this way, only one characteristic per r_0 per $\vec{v}_0$ is needed.

It is possible to avoid utilizing a grid, as in the standard PIC algorithm, and therefore avoid solving the Poisson equation. Instead, the value of E_r can be evaluated using Gauss's theorem:

$$E_r(r) = \frac{1}{r^2}\sum_\alpha \int_0^r \mathrm{d}q_\alpha. \tag{3.4}$$

In the 1D code, there is a finite number of characteristics, each one of them is associated with a charge $\delta q_\alpha = Q_\alpha/N_\alpha$, where Q_α is the total charge of the given species and N_α is the number of characteristics. The integral in 3.4 is replaced by a finite sum over characteristic markers. At $t = 0$, every characteristic starts from an appropriate r_0 and $\vec{v}_0$ chosen from a certain distribution. At $t > 0$, the equations (3.1) are solved for every characteristic using the leap-frog time-differencing scheme.

In the approach used, the ions are considered initially motionless whereas electrons have a 3D Maxwellian velocity distribution with a certain temperature T_e. In the following discussion, only one or two ion species will be considered. The calculations are carried out in dimensionless units. The time, radial coordinate, electric field, particle densities, velocities, and energies are measured in ω_{L1}^{-1}, R, $4\pi Z_1 e n_1 R$, n_1, $R\omega_{L1}$ and $M_1\omega_{L1}^2R^2/2$, respectively, where ω_{L1} is the Langmuir frequency of the heaviest plasma species in the center of cluster, R is the initial characteristic radius of the cluster, Z_1e, n_1, M_1 are the charge, density, mass of the heaviest plasma species. For consistency, the

temperature is measured in the units of $M_1\omega_{L1}^2 R^2/2$.

The reliability of the code was checked for the two single-species cases: (1) CE of a homogeneous ion sphere of given radius with a thin linearly decreasing boundary (*example 2* in [77]) that corresponds to $T_e \to \infty$; (2) a quasi-neutral-like expansion of a spherical plasma with Gaussian initial density profile, that corresponds to $T_e \to 0$. These problems have exact analytical solutions [77, 144].

The asymptotic ion spectrum for the CE regime (1) is given in Fig. 3.1a, where ε is the dimensionless ion kinetic energy. The solid line in Fig. 3.1a represents the numerical spectrum. For reference, the analytic spectrum is given by the dots. Perfect coincidence of the analytical and numerical results is found. The main code benchmark for the electron-ion plasma is provided by

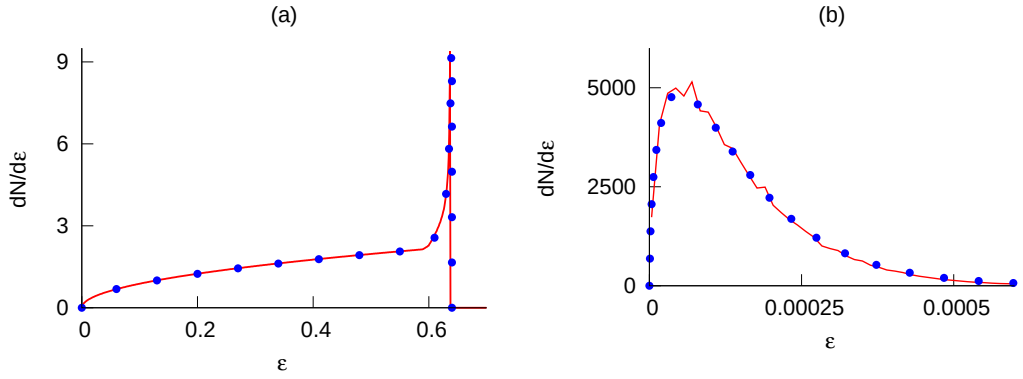

Figure 3.1: (Color) Code benchmarks with various targets configurations: spectrum for CE of *example 2* of [77] (a); quasi-neutral spectrum [144] (b). Solid lines: the numerical results; dots – analytical spectra from the references. Here and below, the spectra are normalized to unity.

the test in the low-temperature regime of plasma expansion (2) which is most difficult for simulations. This regime can be described analytically by a quasi-neutral expansion approximation. Numerical study of this regime requires very high resolution due to the quasi-neutrality condition $r_D \ll R$, where r_D is the electron Debye radius. The resulting asymptotic spectrum of expansion of a

spherical plasma target with initial Gaussian density profile and $R = 140\, r_D$, is found by using 10^7 characteristics. It is given in Fig. 3.1b by the solid line. The corresponding spectrum of exact analytical solution [144] is given by the dots. Again, comparison demonstrates very good matching between these two spectra. The matching indicates that the 1D code describes the 3D problem correctly, without problems of an unphysical behavior.

3.3 Coulomb explosion of inhomogeneous single-species spherical plasma

If the laser is powerful enough, it can strip all the electrons from the target. This happens when the laser electric field component considerably exceeds the electrostatic field of the ion core of the plasma target with fully evacuated electrons. Due to the high ion mass, the ions almost do not interact with the laser field. Rather, when the laser and electrons are gone, the ions repel from each other. On a longer time scale, this results in the explosion of the ion core due to the uncompensated Coulomb forces. This gives rise to a finite energy of ions.

The details of the exploding ions dynamics crucially depend on the initial particle density profile of the ions. It can be shown (see Appendix B.3) that a sphere having initially uniform ion charge density distribution inside radius R_0 will expand while preserving the uniformity of the distribution. This process is demonstrated in Fig. 3.2a. The resulting energy spectrum shown in Fig. 3.2b is rather broad and monotonically increases with increase of energy ε until it reaches the cut-off value ε_{max}. The values in Fig. 3.2 are given in the dimensionless variables and the spectra in Fig. 3.2b are normed to unity.

The situation is different in a physically more sensible case of explosion of

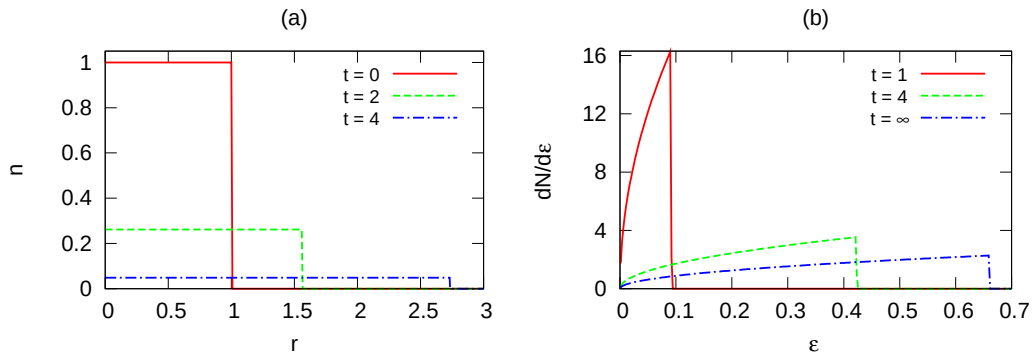

Figure 3.2: (Color) (a) Charge density dynamics of an exploding charged sphere with initially uniform charge distribution; (b) energy spectrum, normed to unity, of the exploding uniformly distributed charged sphere.

a charged sphere having initially inhomogeneous charge density distribution. It is anticipated that for laser-heated targets their density is inhomogeneous, due to pre-expansion of the target after its interaction with the laser pre-pulse. As it was reported in [76] (and mentioned in certain previous papers), the inhomogeneous initial charge distribution results in formation of, generally, multiple shock structures, i.e., structures of vanishing thickness and charge density approaching infinity. In the case of linearly decreasing charge density, a single shock forms. For a nonlinear but monotonic density profile, double shock arises. In a more general non-monotonic charge density, multiple shocks are produced. The case resulting with the double shocks seems the most realistic. The shocks dynamics for the single- and double shocks cases is analyzed in detail in the semi-analytical paper [77].

Formation of the double shocks is explained as follows. Let the initial density profile be described, as an example, by a Gaussian function:

$$n(r, t = 0) = n_0 \exp\Big[- \Big(\frac{r}{R_0}\Big)^2 \Big]. \tag{3.5}$$

This profile is shown in Fig. 3.3a by the purple line. The charge distribution

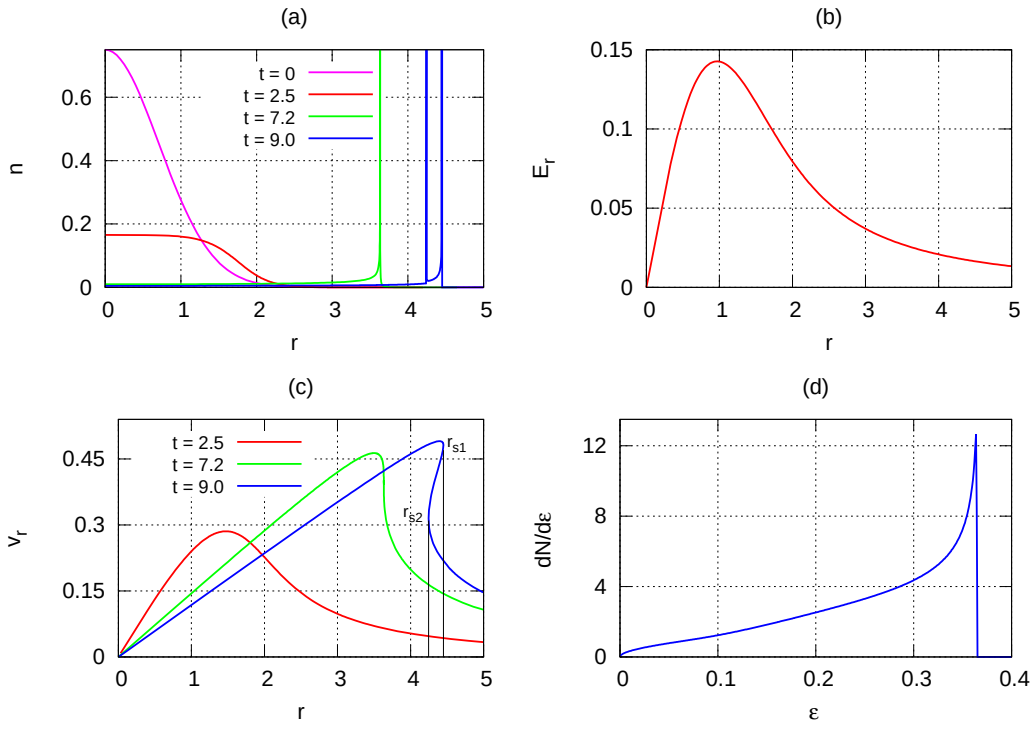

Figure 3.3: (Color) Dynamics of Coulomb explosion of a charged sphere having Gaussian density profile at $t = 0$. (a) Charge density evolution; (b) electrostatic field at $t = 0$; (c) ions in the phase space; (d) ions spectrum at $t = 60$.

(3.5) gives rise to a certain dependence of the radial electric field E_r directed outward. The electrostatic field can be calculated by the Gauss theorem (3.4) and is shown in Fig. 3.3b. The field is non-monotonic, with a maximum at a certain radius inside the charged ball. This is in contrast to the case of a monotonic initial charge density profile for which the field is maximum at the boundary of the ball. The field certainly depends on time but due to its $\sim 1/r_p^2(t)$ dependence on $r_p(t)$, where $r_p(t)$ is the distance from the origin of every given charged particle, it essentially goes to zero after the ball radius increases a few times. Thus, the field gives a kick to all the particles and then vanishes very fast. At $t = 0$, all the charged particles have zero velocity $v_r = 0$. Due to the non-monotonic field distribution, the particles in the vicinity of the field maximum are accelerated by a considerably higher force

than those located far from the maximum. In particular, the particles from the vicinity of the field maximum acquire a larger velocity than those which originally have a larger radius. This is shown by Fig. 3.3c, red line. For this reason, they start to overtake the larger radius particles. Eventually, at time t_s, certain particles having different velocities align at some radius r_{s1} (cf. Fig. 3.3c, green line) which leads to the formation of an instantaneous density peak (i.e, a shock) at r_{s1}, as demonstrated by Fig. 3.3a, green line. At $t > t_s$, the faster particles surpass the slower ones. This leads to the appearance of two points, located at radii r_{s1} and r_{s2}, where the local density of particles is high (mathematically, it approaches infinity). In this way, the single shock splits into two which continue moving outward. This process is depicted in Fig. 3.3a,c, blue line.

The described collisionless shock formation process is essentially kinetic since it involves particle multi-flows inside the expanding ball. For this reason, this process cannot be properly described by hydrodynamic codes.

In Fig. 3.3c, blue line, the most of the particles are bounded between the two shocks. The shocks travel with different velocity. Positions of the shocks as functions of time are given in Fig. 3.4a. It is shown in the approximate theoretical analysis in Ref. [77] that the velocity difference between the two shocks increases as $\ln(t)$ at large t. This is a slow dependence. Furthermore, most of the particles in between the shocks are grouped near the outer one. This gives rise to a much better monoenergeticity of the resulting ions. The spectrum of the exploded charged sphere with Gaussian density profile at $t = 60$ is given in Fig. 3.3d. At this time, the spectrum approaches its asymptotic functional dependence. Although the maximum value of ε is approximately two times smaller than in the case of a uniform charge density profile, much more particles have energy close to ε_{max}. The approaching of the maximum

energy ε_{max} to the asymptotic value is demonstrated by Fig. 3.4b.

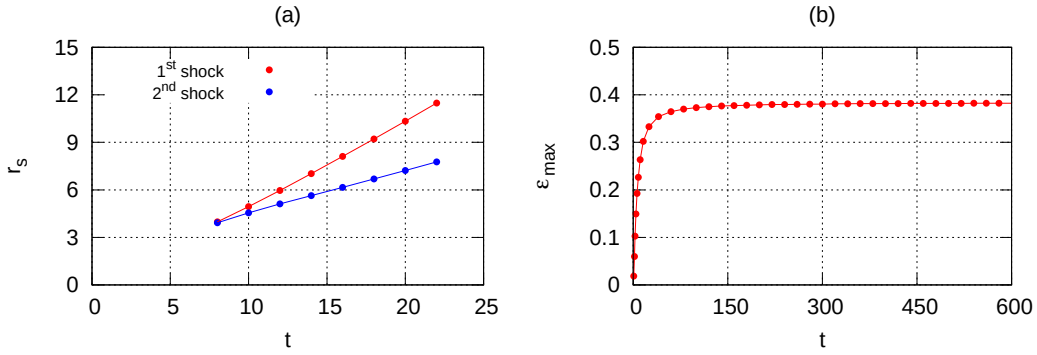

Figure 3.4: (Color) Details of the Gaussian charged sphere explosion. (a) Radii of the shocks vs. time; (b) Maximum acquired energy vs. time.

Let us make an estimate of the maximum energy, in MeV, which can be acquired by the ions in a typical experiment. Having in mind interaction of laser with spherical atomic clusters, let us assign $R = 40\,\mathrm{nm}$ (cf. [162]). Clusters usually have a metal charge density. For a rough estimation, let $n = 250\,n_{cr}$, where n_{cr} is electron critical density. For laser wavelength $\lambda \sim 0.8\,\mu\mathrm{m}$, $250\,n_{cr}$ corresponds to $\sim 2.8 \cdot 10^{23}\,\mathrm{cm}^{-3}$. Let the target be a fully ionized hydrogen cluster. Then the quantity $\varepsilon_0 = M\omega_L^2 R^2/2$ can be calculated and gives $\varepsilon_0 \approx 4\,\mathrm{MeV}$. This gives maximum energy approximately 2.7 MeV for a uniform cluster and 1.5 MeV for the one with a Gaussian initial density profile.

3.4 Charge-separation-driven explosion of a single-species target

A complete evacuation of electrons from a plasma target can depend on a large laser intensity. In the example given at the end of the previous section, the unit of electric field $E_0 = 4\pi enR$ corresponds to the dimensionless laser amplitude

$a = eE_0/m\omega_\lambda c = 2\pi(n/n_{cr})(R/\lambda) \approx 60$. This makes the laser intensity $I \sim 10^{22}\,\mathrm{W/cm^2}$ a minimum requirement for such an experiment. In this way, it makes sense to examine the plasma expansion for smaller intensities.

A smaller laser intensity results in an incomplete electron evacuation. After the laser heating process, the smaller-energy electrons remain inside the plasma core. It is known [163] that the electrons, after the interaction with the laser, possess a complicated velocity distribution function which can be approximated by a two-temperature Maxwellian distribution, with temperatures T_h of hot electrons and T_c of cold ones. Ignoring the inevitable asymmetry resulting from the laser direction, one can adopt this distribution function in the spherically symmetrical problem. In many studies, including recent ones [140, 141, 145, 147, 152, 161], one of the temperatures is ignored altogether. This Thesis follows this approach, considering only a single-temperature case. A more realistic case will be analyzed in a future work.

Let us start the discussion from the case of explosion of uniformly distributed spherical plasma, i.e., plasma with charge density profile given by

$$n_{i,e}(r, t = 0) = \pm n_0 \cdot \begin{cases} 1, \text{ if } r \leq 1, \\ 0, \text{ otherwise }, \end{cases} \tag{3.6}$$

where plus sign stands for ions and minus – for electrons. At $t = 0$, all the ions are motionless and electrons have Maxwellian velocity distribution with a dimensionless temperature $T = T_e/T_0$. The same problem formulation was also considered in [152]. Dynamics of charge density of the electrons and ions as a function of time is shown in Fig. 3.5a for the case of $T = 0.05$. One can easily verify that the potential difference between the center of a completely evacuated spherical plasma and infinity for the case of uniform charge distribution is $\Delta\phi = \varepsilon_0/Ze$ and thus the case of $T = 0.05$ corresponds

to the electron temperature being equal, for $Z = 1$, to 5% of the maximum energy which can be acquired by an electron in the electrostatic field of the fully evacuated ion core. In Fig. 3.5a, the initial charge density of electrons is

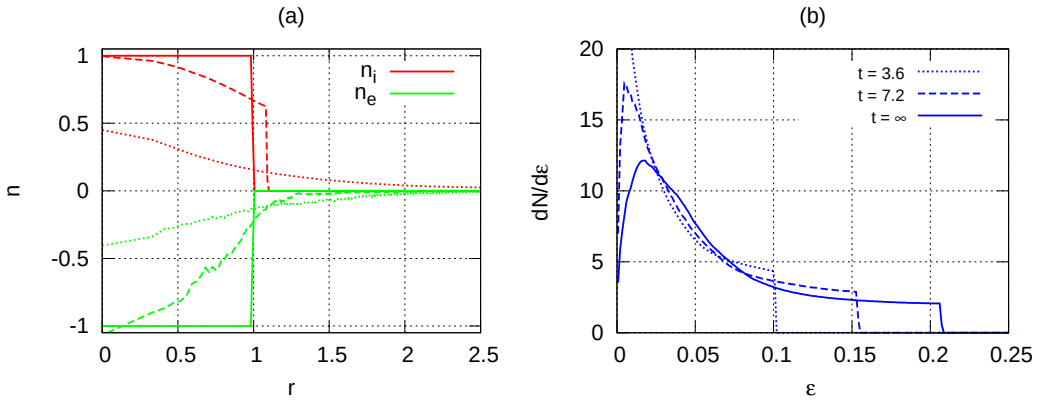

Figure 3.5: (Color) Dynamics of charge-separation driven plasma explosion: (a) charge density of electron and ion components: $t = 0$ (solid lines), $t = 1.2$ (dashed lines), $t = 6$ (dotted lines); (b) evolution of the ion spectrum. Electrons initial temperature $T = 0.05$.

shown by the solid lines. On a short time scale, the electrons, which are not initially at thermodynamical equilibrium, start to move unless the built-up positive charge slows them down and pulls them back. In this way, a certain dynamic equilibrium sets up. At a longer time scale, the built-up charge separation field starts to move the ions as shown by the dashed lines in Fig. 3.5a. This process goes on (dotted lines in Fig. 3.5a) and asymptotically continues to infinity in the approached quasi-neutral regime.

The energy spectrum of the resulting ions is demonstrated in Fig. 3.5b and is qualitatively different from the one shown in Fig. 3.2b. The presence of electrons slows down all the ions and especially those from the bulk of the plasma which now form a local maximum at the lower part of the energy scale. The transformation of the CE spectrum to that of $T \to 0$ limit, with decrease of the temperature, is illustrated in Fig. 3.6a. The cutoff energy ε_{max} is smaller in the finite temperature case than in that of CE, due to the smaller values

of electric field. The ε_{max} is given in Fig. 3.6b and it monotonically increases from 0 for small T to 2/3, CE value, for $T \gg 1$.

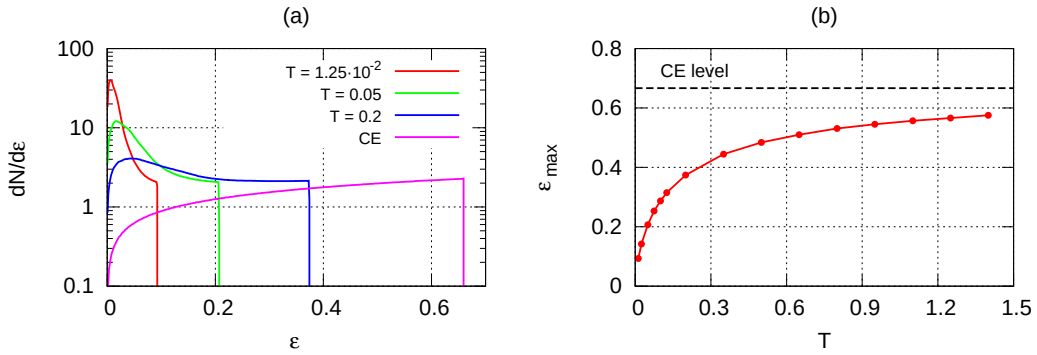

Figure 3.6: (Color). Temperature dependence of asymptotic ion spectrum shape (a) and cutoff energy ε_{max} (b).

The spectrum at $T \to 0$ can be analyzed in more detail. Physically, one can suppose that the $T \to 0$ case can be described analytically with the help of the quasi-neutral approximation which has an analytical solution [143, 144, 145]. The solution given in [143] is a self-similar one, i.e., has the same dependence of distribution function on velocity as on coordinates and thus requires an initial Gaussian density profile for the Maxwellian velocity distribution. The paper [144] (as well as [145]) presents a solution to the Cauchy problem but the symmetry of the solution still requires a Gaussian charge density profile if the velocity distribution function is Maxwellian. The spectrum of quasi-neutral expansion of a Gaussian density profile, according to [144], can be described by formula

$$\mathrm{d}N_{qn}/\mathrm{d}\varepsilon \sim \sqrt{\varepsilon}\exp(-\varepsilon/T_e). \tag{3.7}$$

It is unclear how severe deviations of the quasi-neutral spectrum (3.7) can be in a case of non-Gaussian initial particle density distribution. Figure 3.7a shows the asymptotic spectra of plasma explosion with $T = 10^{-4}$ and uniform

(3.6), Gaussian (3.5) or exponential:

$$n(r, t = 0) = n_0 \exp\big[- \frac{r}{R_0}\big] \tag{3.8}$$

initial density profiles. For reference, a quasi-neutral spectrum (3.7) is given by the dashed line. The uniform density profile is an example of a sharper, than the Gaussian one, plasma boundary whereas the exponential profile is an example of a slower density decrease. The quasi-neutral spectrum lies close to the solid lines in Fig. 3.7a, with very small deviations for the exponent profile and somewhat larger deviations for the uniform one. Therefore, it is safe to use the quasi-neutral expression (3.7) for any smooth initial charge density profile for the small electron temperatures if the required accuracy of the spectrum calculation is within few percents.

Eq. (3.7) does not have a cut-off energy but rather smoothly goes to zero at $\varepsilon \to \infty$. This apparent paradox is caused by the approximation of quasi-neutrality for which high-energy electrons from the Maxwellian tail escape the plasma, and the ions have to follow them to fulfill the quasi-neutrality condition. In reality, of course, there should always be a cut-off energy which, however, is much larger than the local maxima in Fig. 3.7a.

Another important question is the maximum temperature of electrons which still allows one to use the quasi-neutral expression for the spectrum. As follows from Fig. 3.7b, even for the temperature $T = 1.25 \cdot 10^{-2}$, one of the cases shown in Fig. 3.6a, which is already somewhat close to the CE case, the quasi-neutral expression describes the low-energy part of spectrum with a good accuracy. To describe the mismatch between the charge-separation and

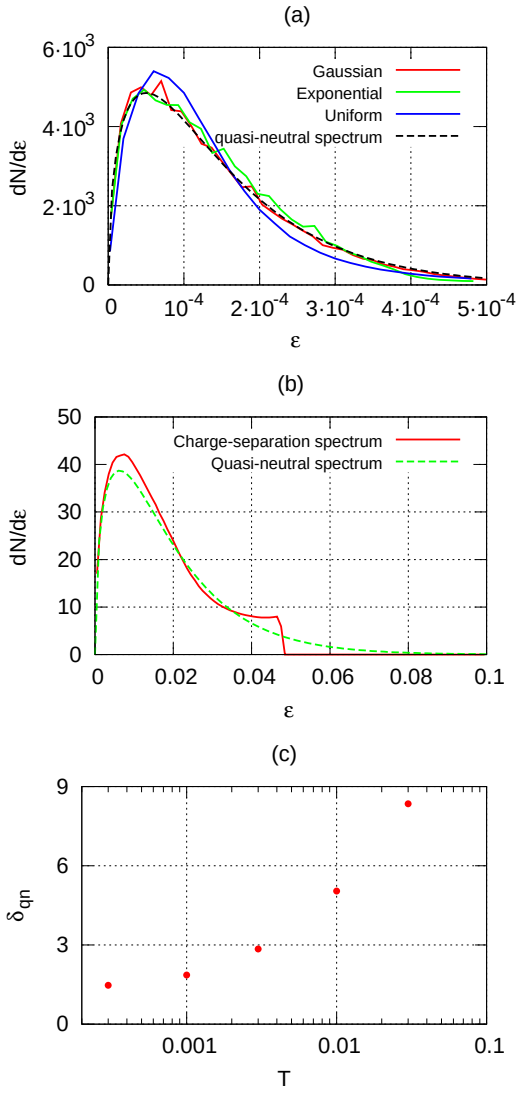

Figure 3.7: (Color). (a) Spectra of plasmas having different initial density profiles and $T = 10^{-4}$. (b) Charge-separation and quasi-neutral spectra for $T = 0.0125$, Gaussian initial density profile. (c) Quantity δ_{qn}, defined in the text, vs. T, for Gaussian initial charge density profile.

quasi-neutral spectra, a quantity

$$\delta_{qn} = \frac{1}{2}\int_0^\infty \Big|\frac{\mathrm{d}N}{\mathrm{d}\varepsilon} - \frac{\mathrm{d}N_{qn}}{\mathrm{d}\varepsilon}\Big|\mathrm{d}\varepsilon \tag{3.9}$$

can be analyzed, where $\mathrm{d}N/\mathrm{d}\varepsilon$ is the spectrum resulting in the numerical calculation. Since the spectra $\mathrm{d}N/\mathrm{d}\varepsilon$ and $\mathrm{d}N_{qn}/\mathrm{d}\varepsilon$ are supposed to be normed to unity, δ_{qn} can take values from 0 to 1. The value $\delta_{qn} = 0$ correspond to the absolute matching of the two spectra and $\delta_{qn} = 1$ corresponds to the absolute mismatch between them. It seems reasonable to have an acceptable value of δ_{qn} within few percents. Figure 3.7c shows the dependence $\delta_{qn}(T)$. For smaller temperatures, δ_{qn} decreases slower due to higher noise of the code at such temperatures. As follows from Fig. 3.7c, the quasi-neutral spectrum gives a good approximation for temperatures $T \lesssim 10^{-2}$ or, equivalently, Debye radius $r_D \lesssim \frac{1}{15}R$.

Let us discuss the expansion of a non-uniform plasma in more detail. As was shown in Sec. 3.3, the non-uniform expansion results in the shock formation. Figure 3.8a shows the creation of a double shock in a plasma with an initially Gaussian charge density profile and electron temperature $T = 1.25\cdot 10^{-2}$. Compared to the CE case, the double shock is formed at a later time point ($t_s \approx 7.2$ for CE case and $t_s \approx 17$ for $T = 1.25 \cdot 10^{-2}$). The mechanism of the shocks creation remains the same as in the CE case with the difference that, due to the partially neutralized ions, all the processes are slower. The moment of shock formation vs. T is depicted in Fig. 3.8b.

The asymptotic spectrum of the inhomogeneous plasma explosion is affected by the finite T in approximately the same way as that of uniform plasma. The sample spectra for different T are depicted in Fig. 3.9a. For a small enough temperature of electrons, the spectrum is nonuniform, with

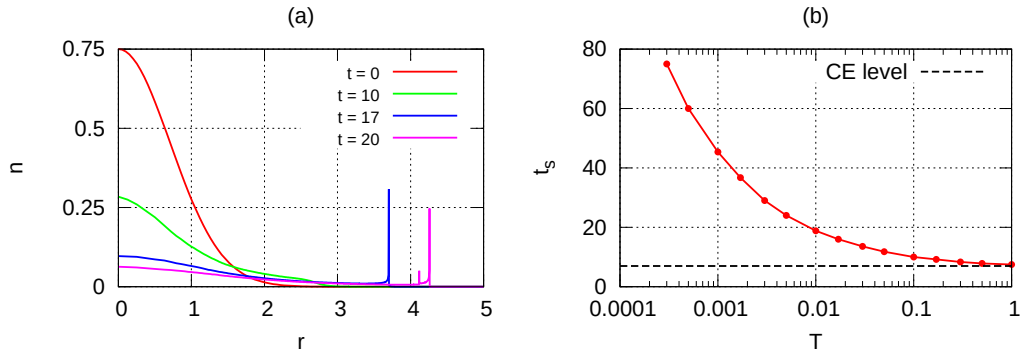

Figure 3.8: (Color). Shock formation in the case of a finite electron temperature: (a) $\rho(r)$ for different moments of time and $T = 1.25{\cdot}10^{-2}$; (b) dependence $t_s(T)$ for a plasma with Gaussian initial density profile.

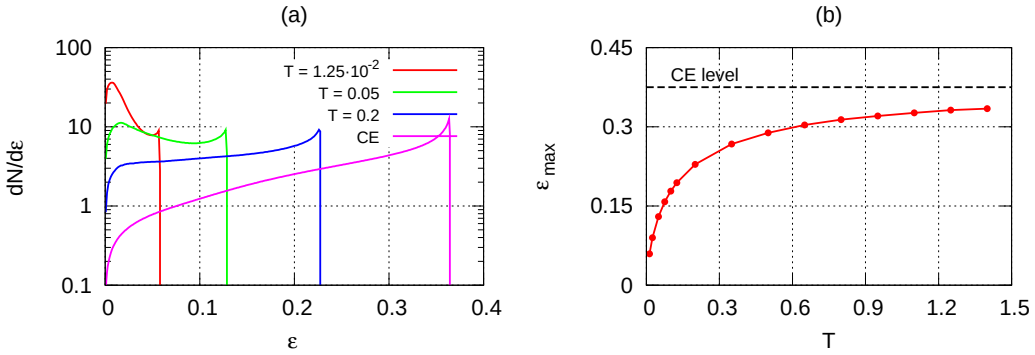

Figure 3.9: (Color). Asymptotic spectra of ions from explosion of a plasma with initial Gaussian density profile and different electron temperatures (a); dependence $\varepsilon_{max}(T)$ for a plasma with Gaussian initial density profile (b).

two local maxima, the first in the region of smaller energies, and the second, due to the shock formation, in the vicinity of the cut-off energy. The cut-off energy as a function of T is given in Fig. 3.9b.

3.5 Two-species plasma explosion

The ion spectrum from the inhomogeneous plasma explosion, shown in Fig. 3.3d, possesses better monoenergeticity than those of a homogeneous plasma (Fig. 3.2b), but is still far from being monoenergetic. It is known for more than forty years [74, 153] that in the case of explosion of a plasma composed

of heavy ions and an impurity of light ions, the latter can acquire a good monoenergetic energetic energy spectrum. However, it is not obvious whether the monoenergetic properties of the light species will remain for the case of a non-negligible admixture of light ions and a finite electron temperature. In this Section[1], an explosion of a two ionic species plasma into vacuum is studied. The mechanism of monoenergetic spectrum formation is discussed and the results of multi-parameter simulations of spherical plasma expansion for different electron temperatures T, relative total light ion charge $\rho_0 = Zn_0/Z_1 n_0^{(1)}$ and kinematic parameter $\mu = M_1 Z/MZ_1$ which defines the relative acceleration rate of the light ions with regard to heavy ion acceleration rate, are demonstrated. In the above notation, index "1" stands for the heavy species and "0" for the light ones.

In Fig. 3.10a, the evolution of the density of light ions is shown. When the spherical plasma is exploding, light ions, which are more mobile, overtake heavy ions, propagate ahead of them and finally gather into a thin shell. This is because the peripheral light ions, which are initially accelerated by the strong radial linearly increasing electric field ($\propto r$ for high electron temperature $T \sim 1$), finally get into the decreasing electric field ($\propto r^{-2}$), where acceleration stops (see Fig.3.10b). The details of this process are illustrated by the phase space plots given in Fig. 3.10c. For a certain set of parameters (typically, ρ_0 less than few tens percent and T larger than several percent) the shell formation is accompanied by multi-flows near the expansion front (c.f. insert in Fig. 3.10c). If light ions exhibit multi-flows, the density peak in the thin light ion shell comes to a singularity $n \propto (1 - r/r_{max})^{-1/2}$ similar to that for CE of a single ion species in an inhomogeneous plasma. The particles accumulated in the shell have radial velocities close to each other and the phase space curves, espe-

[1]The main part of this Section was previously published in [81] and [82].

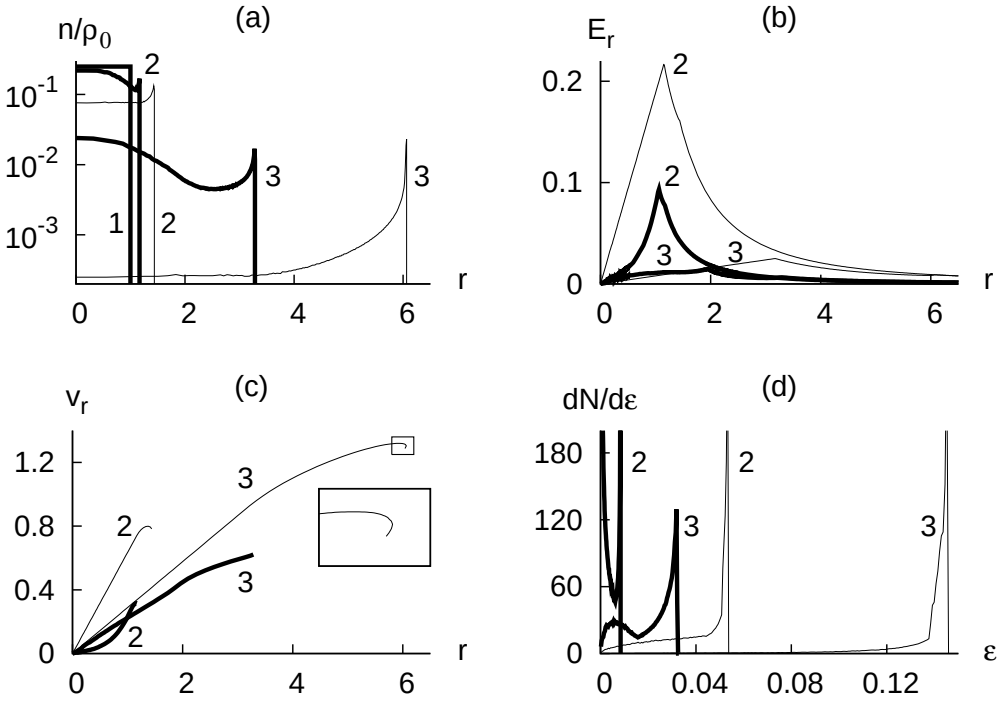

Figure 3.10: Dynamics of the light plasma component for $\mu = 3$ and $\rho_0 = 0.33$: light ions charge density (a), electric field distribution (b), phase space plots (c), energy spectra (d). 1: $t = 0$, 2: $t = 1$, 3: $t = 5$. Thin curves correspond to Coulomb explosion regime ($T \to \infty$) and thick curves correspond to $T = 0.05$.

cially for the Coulomb explosion regime ($T \gg 1$), are flattening near the light ion front with time thus providing a quasi-monoenergetic spectrum. A small fraction of quasi-monoenergetic particles from the vicinity $dv/dr = 0$ forms a peak fine structure of the light ions spectrum as shown in Fig. 3.10d. The energy cutoff of the spectrum is singular, $dN/d\varepsilon \propto (\varepsilon_{max} - \varepsilon)^{-1/2}$. Formation of the density and spectrum singularities is reminiscent of a single species plasma with an inhomogeneous truncated density profile, discussed above, where also overtaking of ions results in a two flow regime with a singularity that arises at the edge of the plasma.

The force of the Coulomb piston acting on the light ions depends on the number of evacuated electrons and thus on their initial temperature. With decreasing electron temperature, fewer electrons leave plasma. The electrons

trapped within the plasma suppress the electric field (c.f. thick and thin curves in Fig. 3.10b) which slows the plasma explosion and leads to the maximum energy of the light ions decreasing with decreasing of T. However, a remarkable feature of the two ion species plasma explosion is the maintenance of monochromaticity for the given number of ions for modest electron temperatures (c.f. thick and thin curves in Fig. 3.10d).

With electron temperature change in a wide range, the spectrum of light ions experiences a dramatic transformation. For small temperatures ($T \to 0$) the spectrum is monotonically decaying with negligible spike at its high-energy end, ε_{max}. With increasing temperature, the spectrum becomes non-monotonic with a minimum (when T is on the order of 1 – 2%). With further temperature increase the spectrum flattens in the main domain and finally becomes monotonic with a sharp increase near the energy cutoff ($T \lesssim 1$). Thus, for dimensionless electron temperatures exceeding several percents, the light ion spectrum for a two ion species plasma explosion demonstrates a well-pronounced monochromatic feature. The energy and spectral width of the monoenergetic light ions depends on three controlling parameters, T, ρ_0, and μ. Below several illustrative examples of the dependencies on these parameters are presented.

The energy spectrum of the exploding plasma is characterized by three main parameters: the energy cutoff, ε_{max}, the relative width of the quasi-monoenergetic spectrum, $\Delta\varepsilon/\varepsilon_{max}$, and the relative number of monoenergetic particles, $\Delta N/N$ (in the energy interval $\Delta\varepsilon$). For definiteness, let us introduce a spectrum width which is the $\Delta\varepsilon$ where the monoenergetic spectral contour line is twice as large as the average spectral level, $N/\overline{\varepsilon}$, where N is the total number of particles, $\overline{\varepsilon} = \int_0^{\varepsilon_{max}} (dN/d\varepsilon)d\varepsilon$, and $\Delta N = \int_{\varepsilon_{max}-\Delta\varepsilon}^{\varepsilon_{max}} (dN/d\varepsilon)d\varepsilon$ is the number of monoenergetic particles. The typical light ion spectra of the

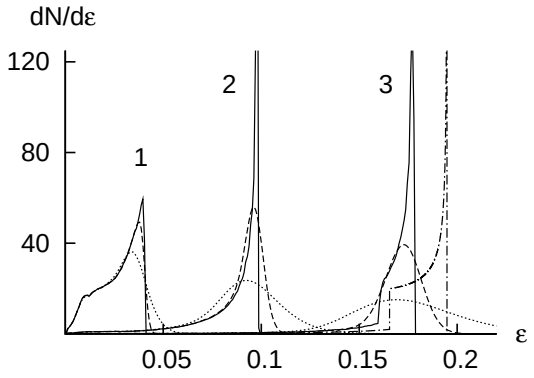

Figure 3.11: Asymptotic light ions spectra for $\rho_0 = 0.33$, $\mu = 3$: $T = 0.05$ (1), $T = 0.3$ (2), and $T \gg 1$, CE regime (3). Solid lines show the spectra of a single plasma, dashed lines show average spectra of multiple spherical plasma targets having $\pm$ 3% radius dispersion, dotted lines – spectra of the targets having $\pm$ 10% radius dispersion. The dash-dotted line shows the theoretical asymptotical spectrum of Coulomb explosion with $\rho \to 0$ and $t \to \infty$.

exploding plasma at a late time moment, for different temperatures, are shown in Fig. 3.11 by solid lines. Figure 3.11 reveals the strong dependence of ε_{max} and spectrum shape on the electron temperature. For example, for $T = 0.3$ and CE regime the spectra in Fig. 3.11 have singularities at the energy cutoff, whereas for $T = 0.05$ the spectrum is finite because of the absence of multi flows. Note that even for the single flow regime the light ion spectrum can be quasi-monoenergetic if the electron temperature is at the level $T \gtrsim 0.1 - 0.2$.

In a real experiment there is always a natural spread of the cluster sizes. Let us suppose that cluster radii are distributed according to the Gaussian law: $\propto \exp\left[-\left((R - R_0)/\Delta R\right)^2\right]$, where R_0 is the clusters average radius and ΔR is the radius spread. Asymptotic light ion spectra for $T = 0.05$, $T = 0.3$ and CE regime for $\Delta R/R_0 = 3\%$ and 10% are given in Fig. 3.11 by the, correspondingly, dashed and dotted lines. The spectrum slightly broadens for the small temperature case and becomes much broader for the high temperature and especially CE cases.

To understand the resulting spectra, below an analytical solution of plasma

explosion for an impurity of light ions ($\rho \ll 1$) in the Coulomb explosion regime is presented. In this case the light ions move in the field [77, 156]:

$$E(t,r) = \begin{cases} r(1-u^2)^3/3\,, & r < (1-u^2)^{-1}\,, \\ r^{-2}/3\,, & r \geq (1-u^2)^{-1}\,, \end{cases} \tag{3.10}$$

where $t = \sqrt{6}\int\limits_0^u \mathrm{d}\xi/(1-\xi^2)^2$.

The distribution function of the radial velocity of the cold light ions can be calculated as [77]

$$F(t,r,v_r) = \frac{1}{r^2}\int_0^\infty \mathrm{d}h\, h^2\, n_0(h)\, \delta(r-R)\, \delta(v_r - U)\,, \tag{3.11}$$

where the functions $R = R(t,h)$ and $U = U(t,h)$ are the solutions to the following equations:

$$R_t = U,\;\; U_t = w(t,R)/R^2,\;\; R\,|_{t=0} = h,\, U\,|_{t=0} = 0, \tag{3.12}$$

$w(t,r) = (Ze/M)r^2 E(t,r)$. In Eq. (3.12), the field E is given by Eq. (3.10). The Eqs. (3.10) – (3.12) allow one to obtain all the light ion characteristics including the energy spectrum. The asymptotic spectrum of the light ions corresponding to this solution is shown in Fig. 3.11 by the dash-dotted line. This spectrum is close to the one obtained in the numerical simulation so long as ρ is not too large. It is therefore concluded that the theory given above is applicable for $\rho \lesssim 20\%$. The dependence of the cutoff energy (in physical units) on the kinematic parameter following from Eqs. (3.10) – (3.12) is defined by a simple approximated formula

$$\varepsilon_{max} \approx \frac{3}{2}\frac{Z_1 e Q_1}{R}\big[\mu - 1/3\big]\frac{M}{M_1}, \tag{3.13}$$

where Q_1 is the total charge of the heavy component.

The formula (3.13) can be generalized to the case of a finite temperature comparable to the Coulomb energy of the ion core in a qualitative manner. An estimation of the total charge of electrons inside the ion core is $Q_e \sim Q_1 \cdot (R/(R+\lambda_D))^3$. The negative electron charge partly compensates the charge Q_1 in (3.13), thus giving $Q_1 - Q_e$ as an effective accelerating charge. Therefore, for large finite temperatures the formula (3.13) may be written as

$$\varepsilon_{max} \approx \frac{3}{2}\frac{Z_1 e Q_1}{R}\Big(1 - \big(\frac{1}{1+\sqrt{T/2}}\big)^3\Big)\big[\mu - 1/3\big]\frac{M}{M_1}. \qquad (3.14)$$

The effective charge concept corresponds to approximately the same shape of spectrum. Lines 2 and 3 in Fig. 3.11 clearly demonstrate that this is the case for large enough temperatures. If the temperature decreases, one has to use the results of numerical calculations.

Let us now discuss the mechanism of narrow spectrum formation in more detail for the case of Coulomb explosion of a plasma with an impurity of light ions. If $\mu \to \infty$ (immobile heavy ions) the light ions spectrum is broad because of the significant potential difference between center and boundary of the heavy core. The light ions from the boundary appear much slower than those from the center in this case. If the heavy ions can move (finite μ), this affects only those light ions which have not left the heavy core. This results in reduced acceleration of the inner light ions and better monoenergeticity. If μ is too low, $(\mu - 1 \ll 1)$, only a small fraction of them is able to leave the core although being monoenergetic. When the light particles are accelerated inside the heavy core, their spectrum is broad, $dN/d\varepsilon \sim \sqrt{\varepsilon}$. In this way, a modest $\mu \sim 5$ leads to a considerable number of monoenergetic particles. This is illustrated by the case of μ=3 shown in Figs. 3.10, 3.11 that can be applied,

for example, to a mixture of carbon and hydrogen, $C^{+4}H^{+1}$. Such ionization states can be obtained from interaction of a carbohydrate cluster with a laser having intensity of 10^{18} W/cm^2 or higher. The cluster radius in this case may be on the order of 20 nm to fall into temperature regimes discussed. The r^2 dependence of the number of particles per dr is another reason for high numbers of monoenergetic particles.

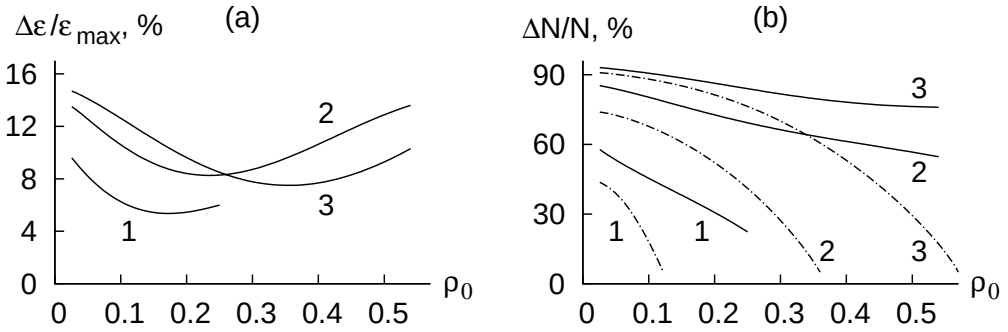

Figure 3.12: (a) The asymptotic spectrum width vs. ρ_0; (b) the number of monoenergetic particles (solid lines) and the number of particles participating in multi flows (dash-dotted lines) vs. ρ_0. $\mu = 3$, $T = 0.05$ (1), $T = 0.3$ (2), and $T \gg 1$, CE regime (3).

The dependencies $\Delta\varepsilon/\varepsilon_{max}$ and $\Delta N/N$ on the relative charge ratio ρ_0 for different electron temperatures can be discussed in more detail. As was pointed out above, for small ρ_0, light particles experience multi-flows. The size of the multi-flow sheath is universal in this case and does not depend on ρ_0 for $\rho_0 \ll 1$. With increasing light ion density, the self-field of the formed ion shell somewhat equalizes the total accelerating field and this leads to reduction of overtaking of the front particles by the back ones. Correspondingly, the multi-flow sheath decreases, leading to an improvement in the spectrum. At some ρ_0, when the total light ion charge is comparable in magnitude to the heavy ion charge, the expansion becomes a single flow. At the same time the spectrum loses monochromaticity with a decreasing of the number of monoenergetic

particles. For CE, multi-flow does not arise for $\rho_0 \gtrsim 0.4$ (cf. [156] where the single-flow regime for a bi-layered spherical plasma was restricted to the $\rho_0 \gtrsim 0.38$) and for smaller ρ_0 with finite temperature. This is illustrated in Fig. 3.12. The number of particles participating in multi flows is shown in Fig. 3.12b. The remarkable feature is that for a wide range of electron temperatures $0.04 < T < \infty$ the spectra of light ions are (1) narrow and (2) contain a considerable fraction or majority of the particles. It is also noted that for a wide range of electron temperatures the cutoff energy weakly changes (within 10 – 20%) with change of ρ in the range $0 \geq \rho_0 \gtrsim 1$.

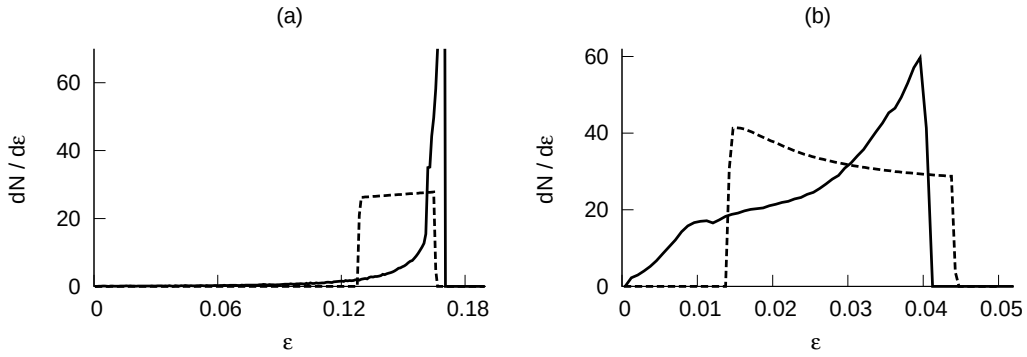

Figure 3.13: Asymptotic spectra of homogeneous (solid lines) and heterogeneous (dashed lines) compositions of the targets. $\mu = 3$, $\rho_0 = 0.33$. (a) Coulomb explosion regime; (b) $T = 0.05$.

The target structuring is another important parameter which can affect the resulting spectrum of light ions. As was mentioned above, a heterogeneous target ([79, 156]) should provide a high energy of the light ions because the light particles are initially located in the narrow domain near the maximum electric field. The small thickness of the layer is a factor of good monoenergeticity. For example, if $\rho_0 = 1/3$, $\mu = 3$ and mass densities of the species are approximately equal to each other, the thickness of the light ions layer is only 3-4% of the cluster radius. However, as follows from Fig.3.13, a homogeneous target with the same ρ_0 does provides an even better particle monoenergeticity and has

approximately the same energy for both CE and thermal-like regimes. It is obvious that the manufacture of homogeneous micro-targets is simpler that offers an advantage of their practical use.

3.6 Conclusion

In this Chapter, the problem of explosion of a spherical plasma composed of one or two ionic species, motionless at $t = 0$ and hot single-temperature electrons, was solved numerically with the help of specially developed gridless particle code. The code was designed with the capability of describing the evolution of an initial 3D particle velocity distribution under the conditions of spatial spherical symmetry. The code was tested on the problems having analytical solutions and has demonstrated to give the matching results.

Using the example of Coulomb explosion, the limiting case of plasma explosion with electron temperature $T_e \to \infty$, it was shown that the kinetic effects determine the formation of collisionless shocks in the case of inhomogeneous initial particle density profile of plasma. The energy spectra and dynamics of shocks was presented and discussed.

For the finite temperature of electrons, the spectra of resulting ions were obtained for the wide range of temperatures $0 \lesssim T_e \leq \infty$. It was shown that for finite temperatures, the spectra of ions become quantitatively and qualitatively different from those of the CE regime. For explosion of inhomogeneous plasmas, the collisionless shocks still exist but appear at later times compared to the Coulomb explosion. In the limit $T_e \to 0$, the ion spectrum almost does not depend on the particle density profile and can be described by a simple analytical expression.

Explosion of plasmas composed of two ionic species was shown to be able

to serve as a source of monoenergetic ions, with monochromaticity holding within a wide range of electron temperatures, from few percents of the plasma Coulomb energy up to values much higher than the Coulomb energy. As in the case of a single ionic species plasma, monoenergetic ions participate in multi flows that can not be studied within the hydrodynamic approach and require kinetic description. A further study has demonstrated an optimum light ion concentration at levels of up to few tens of percent for the best spectrum monochromaticity. The number of monoenergetic ions can be as high as 70-80% of the total light ions. Changing of spherical plasmas radii, their radial distribution, light ions concentration, kinematic parameter and laser intensity allows one to control the monoenergeticity and cutoff energy of the light ions. This could be a way for optimization of laser triggered nuclear reactions in, for expample, a cluster gas.

The 1D model presented here can be improved by having a two-temperature velocity distribution function of electrons which is much more realistic. A complete study would require 3D electromagnetic simulations with laser and ionization physics included. This goal is currently beyond the present study but can be fulfilled in the future.

Appendix A

Electron acceleration

A.1 Charged particle in a plane electromagnetic wave

The motion of charged particles in a relativistically strong plane electromagnetic wave is one of a few problems where the solution can be found exactly. Its solution can be found in a number of textbooks (see, for example, [164]). Here is another derivation.

Let the particle of charge q and mass m be at rest at time $t = 0$:

$$\begin{aligned} \vec{r}(0) &= 0, \\ \vec{p}(0) &= 0, \end{aligned} \tag{A.1}$$

where $\vec{r}$ and $\vec{p}$ are, correspondingly, particle coordinate and momentum. Let this particle move in a plane polarized plane electromagnetic wave, which, written in CGS units, has form:

$$\begin{aligned} \vec{E}(\vec{r},t) &= E_0 \cdot (0,\, \cos(kx - \omega t + \varphi_0),\, 0), \\ \vec{B}(\vec{r},t) &= E_0 \cdot (0,\, 0,\, \cos(kx - \omega t + \varphi_0)), \end{aligned} \tag{A.2}$$

where E_0 is the wave amplitude, ω is the wave frequency, $k = \omega/c$, c is the speed of light, and φ_0 is the initial phase of the wave.

In the absence of radiation losses, the particle equation of motion is

$$\begin{aligned} \frac{\mathrm{d}\vec{p}}{\mathrm{d}t} &= q\Big(\vec{E} + \frac{1}{c}[\vec{v} \times B]\Big), \\ \frac{\mathrm{d}\vec{r}}{\mathrm{d}t} &= \frac{\vec{p}}{m\sqrt{1 + (\vec{p}/mc)^2}}, \end{aligned} \tag{A.3}$$

where $\vec{v} = \vec{p}/(m\sqrt{1 + (\vec{p}/mc)^2})$ is the particle velocity.

To solve equation (A.3), let us introduce vector potential $\vec{A}$:

$$\nabla \times \vec{A} = \vec{B}. \tag{A.4}$$

In the absence of electrostatic fields, which is the case for the plane electromagnetic wave, the vector potential defines also the electric component of the field:

$$\vec{E} = -\frac{1}{c}\frac{\partial \vec{A}}{\partial t}. \tag{A.5}$$

Substituting (A.5) into the first equation of (A.3), one gets

$$\frac{\mathrm{d}\vec{p}}{\mathrm{d}t} = q\Big(-\frac{1}{c}\frac{\partial \vec{A}}{\partial t} + \frac{1}{c}[\vec{v} \times (\nabla \times \vec{A})]\Big). \tag{A.6}$$

Using vector identity

$$\vec{v} \times \mathrm{rot}(\vec{A}) = \nabla \cdot (\vec{A} \cdot \vec{v}) - (\vec{v} \cdot \nabla)\vec{A}, \tag{A.7}$$

one can rewrite (A.6) in the following form:

$$\frac{\mathrm{d}\vec{p}}{\mathrm{d}t} = -\frac{q}{c}\Big(\frac{\partial \vec{A}}{\partial t} + (\vec{v} \cdot \nabla)\vec{A} - \nabla(\vec{A} \cdot \vec{v})\Big) = -\frac{q}{c}\Big(\frac{\mathrm{d}\vec{A}}{\mathrm{d}t} - \nabla(\vec{A} \cdot \vec{v})\Big), \tag{A.8}$$

or, that is equivalent,

$$\frac{\mathrm{d}}{\mathrm{d}t}\Big(\vec{p}+\frac{q}{c}\vec{A}\Big)=\frac{q}{c}\nabla(\vec{A}\cdot\vec{v}). \tag{A.9}$$

Equation (A.9) is the general equation of motion of a charged particle in an electromagnetic field defined by vector potential $\vec{A}$. To proceed further, let us note that as both $\vec{E}$ and $\vec{B}$ have a simple form given by (A.2), the vector potential of the plane wave also depends only on the quantity $kx-\omega t$:

$$\vec{A}=\frac{E_0}{k}\cdot(0,\,\sin(kx-\omega t+\varphi_0),\,0). \tag{A.10}$$

For this reason,

$$\frac{\partial}{\partial y}(\vec{v}\cdot\vec{A})=\frac{\partial}{\partial z}(\vec{v}\cdot\vec{A})=0. \tag{A.11}$$

Substituting (A.11) into (A.9), one gets

$$\frac{\mathrm{d}}{\mathrm{d}t}\Big(\vec{p}+\frac{q}{c}\vec{A}\Big)_y=\frac{\mathrm{d}}{\mathrm{d}t}\Big(\vec{p}+\frac{q}{c}\vec{A}\Big)_z=0, \tag{A.12}$$

or, more generally,

$$\frac{\mathrm{d}}{\mathrm{d}t}\Big(\vec{p}+\frac{q}{c}\vec{A}\Big)_\perp=0, \tag{A.13}$$

where $\perp$ sign means a component in the direction perpendicular to $\hat{x}$. Equation (A.13) defines the first integral of particle motion in a plane electromagnetic wave.

Let us now form a scalar product of the first equation in (A.3) with $\vec{v}$:

$$\frac{\mathrm{d}\vec{p}}{\mathrm{d}t}\cdot\vec{v}=q\Big(\vec{E}+\frac{1}{c}[\vec{v}\times B]\Big)\cdot\vec{v}. \tag{A.14}$$

It is easy to see that $[\vec{v}\times B]\cdot\vec{v}=0$ because $\vec{v}\times B$ is perpendicular to $\vec{v}$.

Therefore, Eq. (A.14) turns into

$$\frac{\mathrm{d}\vec{p}}{\mathrm{d}t}\cdot\vec{v}=q\vec{E}\cdot\vec{v}. \tag{A.15}$$

To evaluate the left part of Eq. (A.15), let's differentiate the square of particle total energy $\varepsilon^2=(\gamma mc^2)^2=p^2c^2+m^2c^4$, where $\gamma=\sqrt{1+(\vec{p}/mc)^2}$ is the particle relativistic factor:

$$\frac{\mathrm{d}\varepsilon^2}{\mathrm{d}t}=2\vec{p}c^2\cdot\frac{\mathrm{d}\vec{p}}{\mathrm{d}t}=2\gamma mc^2\vec{v}\cdot\frac{\mathrm{d}\vec{p}}{\mathrm{d}t}=2\varepsilon\frac{\mathrm{d}\vec{p}}{\mathrm{d}t}\cdot\vec{v}. \tag{A.16}$$

On the other hand,

$$\frac{\mathrm{d}\varepsilon^2}{\mathrm{d}t}=2\varepsilon\frac{\mathrm{d}\varepsilon}{\mathrm{d}t}. \tag{A.17}$$

Combining together Eqs. (A.16) and (A.17), one gets

$$\frac{\mathrm{d}\vec{p}}{\mathrm{d}t}\cdot\vec{v}=\frac{\mathrm{d}\varepsilon}{\mathrm{d}t}. \tag{A.18}$$

In this way, Eq. (A.15) reads

$$q\vec{E}\cdot\vec{v}=\frac{\mathrm{d}\varepsilon}{\mathrm{d}t}. \tag{A.19}$$

Returning back to Eq. (A.9), one finds that

$$\frac{\mathrm{d}}{\mathrm{d}t}\Big(\vec{p}+\frac{q}{c}\vec{A}\Big)_x=\frac{q}{c}\frac{\partial}{\partial x}(\vec{A}\cdot\vec{v})=\frac{q}{c}\frac{\partial\vec{A}}{\partial x}\cdot\vec{v}. \tag{A.20}$$

However, denoting $kx-\omega t=\xi$, it is easy to find that

$$\frac{\partial\vec{A}}{\partial x}=\frac{\mathrm{d}\vec{A}}{\mathrm{d}\xi}\frac{\partial\xi}{\partial x}=\frac{\omega}{c}\frac{\mathrm{d}\vec{A}}{\mathrm{d}\xi}=\frac{1}{c}\Big(-\frac{\partial\xi}{\partial t}\Big)\frac{\mathrm{d}\vec{A}}{\mathrm{d}\xi}=-\frac{1}{c}\frac{\partial\vec{A}}{\partial t}=\vec{E}. \tag{A.21}$$

Substituting of Eqs. (A.21) and (A.19) into (A.20) gives

$$\frac{\mathrm{d}}{\mathrm{d}t}\Big(\vec{p}+\frac{q}{c}\vec{A}\Big)_x = \frac{q}{c}\vec{E}\cdot\vec{v} = \frac{1}{c}\frac{\mathrm{d}\varepsilon}{\mathrm{d}t}. \tag{A.22}$$

Note that the fact that $\vec{A}$ is the vector potential of a plane wave was directly used in Eq. (A.21). Equation (A.10) suggests another useful property of the plane wave vector potential: $A_x = 0$. Substituting this into one gets

$$\frac{\mathrm{d}}{\mathrm{d}t}\Big(\frac{\varepsilon}{c} - p_x\Big) = 0, \tag{A.23}$$

or

$$\frac{\mathrm{d}}{\mathrm{d}t}\Big(\gamma(1-\frac{v_x}{c})\Big) = 0. \tag{A.24}$$

Equation (A.24) is the second integral of particle motion.

The integrals of motion (A.13) and (A.24) define important properties of the particle motion. Recalling that the particle is subject to the initial conditions (A.1) at $t = 0$, one can immediately obtain from the first integral:

$$\vec{p}_\perp = \frac{q}{c}\big(\vec{A}_0 - \vec{A}\big)_\perp, \tag{A.25}$$

where $\vec{A}_0$ is the vector potential at the particle position at $t = 0$. The second integral, combined with particle initial conditions (A.1) results in

$$\gamma(1-\frac{v_x}{c}) = 1. \tag{A.26}$$

After a simple algebra, one can get from (A.26) the following

$$p_x + mc = \gamma mc, \tag{A.27}$$

or

$$p_x^2 + 2mcp_x + m^2c^2 = \frac{\varepsilon^2}{c^2} = m^2c^2 + p^2 = m^2c^2 + p_x^2 + p_y^2 + p_z^2, \qquad \text{(A.28)}$$

which results in

$$p_x = \frac{1}{2mc}(p_y^2 + p_z^2). \qquad \text{(A.29)}$$

Equations (A.25) and (A.29) express direct dependence of the particle momentum on the field vector potential. In their derivation, the particular behavior of the field (i.e., its being a plane wave) was used twice: in Eqs. (A.11) and (A.21). Of course, Eq. (A.25) contains dependence on the particle position in its right hand side which can be obtained only after solving the second equation in (A.3). However, some important conclusions can be drawn even from the limited information enclosed in Eqs. (A.25) and (A.29). To do it, let us transfer to the dimensionless coordinates $\vec{\tilde{p}}$ and ξ:

$$\vec{\tilde{p}} = \frac{\vec{p}}{mc} \qquad \text{(A.30)}$$

and $kx - \omega t = \xi$, as before in Eq. (A.21). Making transformation to the dimensionless coordinates in Eqs. (A.25) and (A.29) and substituting Eq. (A.10) into (A.25), one can obtain:

$$\begin{aligned} \tilde{p}_x &= \frac{\tilde{p}_y^2}{2}, \\ \tilde{p}_y &= a_0[\sin(\varphi_0) - \sin(\xi + \varphi_0)], \\ \tilde{p}_z &= 0, \end{aligned} \qquad \text{(A.31)}$$

where

$$a_0 = \frac{qE_0}{m\omega c} \qquad \text{(A.32)}$$

is the dimensionless field parameter. One can see from Eq. (A.31) that as ξ changes, the quantity $\tilde{p}_y$ changes between $a_0[\sin(\varphi_0) - 1]$ and $a_0[\sin(\varphi_0) + 1]$, i.e., it is proportional to a_0, whereas $\tilde{p}_x$ is proportional $a_0^2/2$. In this way, the parameter a_0 defines the behavior of particle dynamics: if $a_0 \ll 1$ the motion is nonrelativistic, with $p_x \ll p_y$, i.e., predominantly in the transverse direction. When $a_0 \gtrsim 1$, the motion becomes relativistic, with momenta being relativistic in both transverse and longitudinal directions. If $a_0 \gg 1$, the motion is ultrarelativistic, with $p_x \gg p_y \gg mc$. $a_0 \approx 1$ for the intensity $I \approx 10^{18}\,\mathrm{W/cm^2}$ of a light having wavelength $\lambda \approx 1\,\mu\mathrm{m}$.

As the particle velocity is always smaller than speed of light, the quantity $\xi = kx(t) - \omega t$ monotonically decreases, although in a complicated nonlinear way. However, because ξ enters momenta (A.31) as an argument of a trigonometric function, the momenta are periodical in ξ and, as a consequence of monotonic dependence $\xi(t)$, are periodical in time. Therefore, particle γ-factor $\gamma = \sqrt{1 + \tilde{p}_x^2 + \tilde{p}_x^2 + \tilde{p}_x^2}$ is also periodical in time, with

$$\begin{aligned} \min(\gamma) =& 1 \qquad (\text{for } \xi = 2\pi n), \\ \max(\gamma) =& \sqrt{1 + a_0^2(1+\sin\varphi_0)^2 + \frac{a_0^4(1+\sin\varphi_0)^4}{4}} = \\ & 1 + \frac{a_0^2}{2}(1+\sin\varphi_0)^2 \qquad (\text{for } \xi = 2\pi n - \frac{\pi}{2} - \varphi_0), \end{aligned} \tag{A.33}$$

where n is an integer number. In an ultrarelativistic regime ($a_0 \gg 1$),

$$\max(\gamma) \propto a_0^2. \tag{A.34}$$

Let us now integrate the second equation in (A.3) to find the particle trajectory. It is also convenient to work in the dimensionless spatial coordinates

and time here:

$$\begin{aligned}\vec{\tilde{r}} &= \frac{\vec{r}}{\lambda} = \frac{k\vec{r}}{2\pi},\\ \tilde{t} &= \frac{\omega t}{2\pi}.\end{aligned} \tag{A.35}$$

In the dimensionless coordinates,

$$\xi = 2\pi(\tilde{x} - \tilde{t}), \tag{A.36}$$

and the second equation of (A.3) has form

$$\frac{\mathrm{d}\tilde{x}}{\mathrm{d}\tilde{t}} = \frac{\tilde{p}_x}{\gamma} = \frac{a_0^2[\sin\varphi_0 - \sin(\xi+\varphi_0)]^2/2}{1 + a_0^2[\sin\varphi_0 - \sin(\xi+\varphi_0)]^2/2}, \tag{A.37}$$

$$\frac{\mathrm{d}\tilde{y}}{\mathrm{d}\tilde{t}} = \frac{\tilde{p}_y}{\gamma} = \frac{a_0[\sin\varphi_0 - \sin(\xi+\varphi_0)]}{1 + a_0^2[\sin\varphi_0 - \sin(\xi+\varphi_0)]^2/2}, \tag{A.38}$$

$$\frac{\mathrm{d}\tilde{z}}{\mathrm{d}\tilde{t}} = 0. \tag{A.39}$$

To solve Eq. (A.37), let us note that

$$\frac{\mathrm{d}\xi}{\mathrm{d}\tilde{t}} = \frac{\partial\xi}{\partial\tilde{t}} + \frac{\partial\xi}{\partial\tilde{x}}\frac{\mathrm{d}\tilde{x}}{\mathrm{d}\tilde{t}} = 2\pi\Big(\frac{\mathrm{d}\tilde{x}}{\mathrm{d}\tilde{t}} - 1\Big). \tag{A.40}$$

Substituting (A.37) into (A.40), one gets

$$\begin{aligned}\frac{\mathrm{d}\xi}{\mathrm{d}\tilde{t}} =& 2\pi\Big(\frac{a_0[\sin\varphi_0 - \sin(\xi+\varphi_0)]}{1 + a_0^2[\sin\varphi_0 - \sin(\xi+\varphi_0)]^2/2} - 1\Big) =\\ & - 2\pi\frac{1}{1 + a_0^2[\sin\varphi_0 - \sin(\xi+\varphi_0)]^2/2}.\end{aligned} \tag{A.41}$$

Equation (A.41) can be integrated using method of separation of variables:

$$-\frac{1}{2\pi}\int_0^{\xi}\Big(1 + \frac{a^2}{2}[\sin\varphi_0 - \sin(\xi+\varphi_0)]^2\Big)\mathrm{d}\xi = \tilde{t}, \tag{A.42}$$

or, evaluating the integral in the left hand side,

$$-\frac{1}{2\pi}\Big\{\xi[1+\frac{a_0^2}{4}(1+2\sin^2\varphi_0)]-\frac{3}{8}a_0^2\sin(2\varphi_0)+ \\ a_0^2\sin\varphi_0\cos(\xi+\varphi_0)-\frac{a_0^2}{8}\sin[2(\xi+\varphi_0)]\Big\}=\tilde{t}. \tag{A.43}$$

Substituting $\tilde{x}=\tilde{t}+\xi/(2\pi)$ (cf. (A.36)), one can obtain a similar relation between $\tilde{x}$ and ξ:

$$\tilde{x}=-\frac{1}{2\pi}\Big\{\frac{a_0^2}{4}\xi(1+2\sin^2\varphi_0)-\frac{3}{8}a_0^2\sin(2\varphi_0)+ \\ a_0^2\sin\varphi_0\cos(\xi+\varphi_0)-\frac{a_0^2}{8}\sin[2(\xi+\varphi_0)]\Big\}. \tag{A.44}$$

To solve Eq. (A.38), let us note that as $\mathrm{d}\tilde{y}/\mathrm{d}\tilde{t}$ is a function of only ξ and $\tilde{t}$ can be represented, according to Eq. (A.43), as a function of ξ, $\tilde{y}$ is also a function of ξ. Therefore,

$$\frac{\mathrm{d}\tilde{y}}{\mathrm{d}\tilde{t}}=\frac{\mathrm{d}\tilde{y}}{\mathrm{d}\xi}\frac{\mathrm{d}\xi}{\mathrm{d}\tilde{t}}, \tag{A.45}$$

and

$$\frac{\mathrm{d}\tilde{y}}{\mathrm{d}\xi}=\frac{\mathrm{d}\tilde{y}/\mathrm{d}\tilde{t}}{\mathrm{d}\xi/\mathrm{d}\tilde{t}}. \tag{A.46}$$

Substituting Eqs. (A.38) and (A.41) into (A.46), one gets an easily integrable equation:

$$\frac{\mathrm{d}\tilde{y}}{\mathrm{d}\xi}=-\frac{a_0}{2\pi}[\sin\varphi_0-\sin(\xi+\varphi_0)], \tag{A.47}$$

which has the following solution for the boundary condition $y_{\xi=0}=0$:

$$\tilde{y}=-\frac{a_0}{2\pi}[\xi\sin\varphi_0-\cos\varphi_0+\cos(\xi+\varphi_0)]. \tag{A.48}$$

Finally, the last equation of motion, Eq. (A.39) gives a trivial solution

$$z=0. \tag{A.49}$$

Equations (A.31), (A.44), (A.48) and (A.49) give the dimensionless coordinates of the particle in the phase space as functions of ξ given by Eq. (A.36). However, as the dimensionless time $\tilde{t}$ is also a function of ξ (A.43), ξ can be considered as a parameter:

$$\begin{aligned}
\tilde{t}(\xi) =& -\frac{1}{2\pi}\Big\{\xi[1+\frac{a_0^2}{4}(1+2\sin^2\varphi_0)] - \frac{3}{8}a_0^2\sin(2\varphi_0) + \\
& a_0^2\sin\varphi_0\cos(\xi+\varphi_0) - \frac{a_0^2}{8}\sin[2(\xi+\varphi_0)]\Big\}, \\
\tilde{x}(\xi) =& -\frac{1}{2\pi}\Big\{\frac{a_0^2}{4}\xi(1+2\sin^2\varphi_0) - \frac{3}{8}a_0^2\sin(2\varphi_0) + \\
& a_0^2\sin\varphi_0\cos(\xi+\varphi_0) - \frac{a_0^2}{8}\sin[2(\xi+\varphi_0)]\Big\}, \\
\tilde{y}(\xi) =& -\frac{a_0}{2\pi}[\xi\sin\varphi_0 - \cos\varphi_0 + \cos(\xi+\varphi_0)], \\
\tilde{z}(\xi) =& 0, \\
\tilde{p}_x(\xi) =& \frac{a_0^2}{2}[\sin(\varphi_0) - \sin(\xi+\varphi_0)]^2, \\
\tilde{p}_y(\xi) =& a_0[\sin(\varphi_0) - \sin(\xi+\varphi_0)], \\
\tilde{p}_z(\xi) =& 0.
\end{aligned} \tag{A.50}$$

Equations (A.50) represent the solution, given in the parametric form, to the problem of charged particle motion in a plane polarized plane electromagnetic wave.

An example of particle trajectory and γ-factor for $a = 1$ and $\varphi = 0,\ \pi/6,\ \pi/2$ is given in Fig. A.1. Note that the period of γ-factor oscillations in the laboratory system is not equal to the wave period.

A.2 Ponderomotive force

The ponderomotive force is a nonlinear force arising from dependence of amplitude of an oscillatory field on coordinate. For the expressions derived below

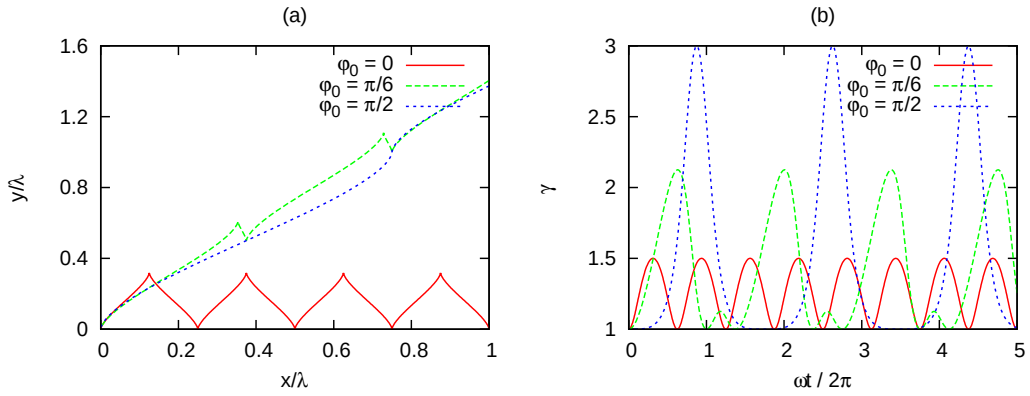

Figure A.1: (Color) Particle trajectory (a) and $\gamma(t)$ (b) for $a = 1$ and $\varphi = 0,\ \pi/6,\ \pi/2$.

to give correct results, the amplitude of oscillations has to be much smaller than the characteristic distance of the field amplitude change.

Here, the derivation is carried out for the simplest case of slow quasi-static field oscillations ($\vec{B} = 0$) and non-relativistic particle motion. A similar derivation for a more general case of small but nonzero $\vec{B}$ can be found in Ref. [165].

Equations of motion of a non-relativistic particle in an oscillating electric field are

$$\begin{aligned} \frac{\mathrm{d}\vec{r}}{\mathrm{d}t} &= \vec{v}, \\ \frac{\mathrm{d}\vec{v}}{\mathrm{d}t} &= \frac{q}{m}\vec{E}. \end{aligned} \tag{A.51}$$

The electric field $\vec{E}$ is supposed to oscillate with a frequency ω:

$$\vec{E} = \vec{E}_s \cos(\omega t), \tag{A.52}$$

where

$$\vec{E}_s = \vec{E}_0 + \vec{E}_1(\vec{r}). \tag{A.53}$$

$\vec{E}_0$ in Eq. (A.53) is supposed to be a constant and $\vec{E}_1$ a slow function of coordinate.

In the zeroth order, $\vec{E} = \vec{E}_0$, and equations of motion have solution

$$\begin{aligned} \delta\vec{v}_0 &= \frac{q}{m\omega}\vec{E}_0 \sin(\omega t), \\ \delta\vec{r}_0 &= \frac{q}{m\omega^2}\vec{E}_0 \cos(\omega t), \end{aligned} \tag{A.54}$$

where $\delta\vec{v}_0$ and $\delta\vec{r}_0$ are deviations of the velocity and coordinate from the zero field values.

In the first order, the field amplitude $\vec{E}_s$ can be written as

$$\vec{E}_s = \vec{E}_0 + \delta\vec{r}_0 \cdot \nabla\vec{E}_1. \tag{A.55}$$

Substituting Eqs. (A.55) and (A.54) into (A.51) one can get

$$\frac{\mathrm{d}\vec{v}}{\mathrm{d}t} = \frac{q}{m}\Big(\vec{E}_0 - \frac{q}{m\omega^2}\vec{E}_0 \cdot \nabla\vec{E}_1 \cos(\omega t)\Big)\cos(\omega t). \tag{A.56}$$

Let us now average Eq. (A.56) over one oscillation period:

$$\left\langle \frac{\mathrm{d}p}{\mathrm{d}t} \right\rangle = -\frac{q^2}{m\omega^2}\left\langle \vec{E}_0 \cdot \nabla\vec{E}_1 \cos^2(\omega t) \right\rangle = -\frac{q^2}{2m\omega^2}\left(\vec{E}_0 \cdot \nabla\vec{E}_s\right), \tag{A.57}$$

where $\vec{p} = m\vec{v}$ and angle brackets denote averaging over one oscillation period. Using vector identity $\vec{E} \cdot \nabla\vec{E} = \nabla(\vec{E}^2)/2 - \vec{E} \times \nabla \times \vec{E}$ and $\nabla \times \vec{E} \approx 0$ for the quasi-static field considered, and setting $\vec{E}_0 \approx \vec{E}_s$ one can rewrite Eq. (A.57) in a more conventional form

$$\vec{F}_p = -\frac{q^2}{4m\omega^2}\nabla\left(\vec{E}_s^2\right) = -\frac{q^2}{2m\omega^2}\nabla\left\langle \vec{E}^2 \right\rangle, \tag{A.58}$$

where $\vec{F}_p = \langle \mathrm{d}p/\mathrm{d}t \rangle$ is the ponderomotive force. Eq. (A.58) holds in a more general case of non-relativistic particle motion in an oscillating electromagnetic field with slow-varying amplitude.

An expression for a relativistic motion can also be derived. Such derivation is performed in, for example, Refs. [60, 166]. The corresponding expression for the relativistic ponderomotive force reads

$$\vec{F}_p = -\frac{q^2}{2\langle\gamma\rangle mc^2}\nabla\left\langle\vec{A}^2\right\rangle, \tag{A.59}$$

where $\langle\gamma\rangle$ is the oscillation period averaged γ-factor of the particle and $\vec{A}$ is the field vector potential. It can be seen that in the non-relativistic limit $\langle\gamma\rangle \to 1$ the Eqs. (A.59) and (A.58) coincide.

A.3 Stratton-Chu integrals

Stratton-Chu integrals have originally appeared in the paper [109] in 1939. The authors of [109] have derived an integral electromagnetic field representation being exact solution to the Maxwell equations. The idea was to use this representation in problems of diffraction of electromagnetic waves. It was not until appearance of fast computers, however, when the integrals could be used in practice. The authors of [109] themselves were unable to calculate the integrals exactly in their example of diffraction of electromagnetic waves on a rectangular slit and had to use paraxial approximation. On a fast computer, however, the integrals can be calculated numerically.

Although the derivation given in [109] is clear, here the integrals will be re-derived, with some steps, omitted in [109], shown explicitly. As the integrals are applied in vacuum in this Thesis, the derivation will also be done for vacuum fields $\vec{E}$ and $\vec{B}$. Unlike [109], the derivation here will be done in CGS units.

Let the emitting surface be A, and the observer is located at point $\vec{r_0} =$

(x_0, y_0, z_0). The A is supposed to be a closed surface, with $\vec{r_0}$ being inside it. Let S be the surface of volume V bounded by A, from one side, and a small sphere of radius δr around $\vec{r_0}$, from the other side.

Let $\vec{P}(\vec{r})$ and $\vec{Q}(\vec{r})$ be vector functions, twice smooth inside V and on its surface. Then, by divergence theorem,

$$\int_V \nabla \cdot (\vec{P} \times \nabla \times \vec{Q}) \mathrm{d}V = \oint_S (\vec{P} \times \nabla \times \vec{Q}) \cdot \mathrm{d}\vec{S}, \tag{A.60}$$

where $\mathrm{d}\vec{S}$ is the vector of length $\mathrm{d}S$ looking outside of the volume. Using the vector identity [167]

$$\nabla \cdot (\vec{A} \times \vec{B}) = \vec{B} \cdot (\nabla \times \vec{A}) - \vec{B} \cdot (\nabla \times \vec{A}) \tag{A.61}$$

in the left side of (A.60), one can obtain

$$\int_V \Big((\nabla \times \vec{Q}) \cdot (\nabla \times \vec{P}) - \vec{P} \cdot (\nabla \times \nabla \times \vec{Q}) \Big) \mathrm{d}V = \oint_S (\vec{P} \times \nabla \times \vec{Q}) \cdot \mathrm{d}\vec{S}. \tag{A.62}$$

It is noted in [109] that if $\vec{P} = \vec{Q} = \vec{E}$, (A.62) is equivalent to the Poynting theorem. As $\vec{P}$ and $\vec{Q}$ are arbitrary they can be exchanged in (A.62):

$$\int_V \Big((\nabla \times \vec{P}) \cdot (\nabla \times \vec{Q}) - \vec{Q} \cdot (\nabla \times \nabla \times \vec{P}) \Big) \mathrm{d}V = \oint_S (\vec{Q} \times \nabla \times \vec{P}) \cdot \mathrm{d}\vec{S}. \tag{A.63}$$

Subtracting now (A.63) from (A.62), one gets:

$$\int_V \Big(\vec{Q} \cdot (\nabla \times \nabla \times \vec{P}) - \vec{P} \cdot (\nabla \times \nabla \times \vec{Q}) \Big) \mathrm{d}V = \oint_S (\vec{P} \times \nabla \times \vec{Q} - \vec{Q} \times \nabla \times \vec{P}) \cdot \mathrm{d}\vec{S}. \tag{A.64}$$

Equation (A.64) is the vector analog of the Green's theorem [168] and is the basic formula for the derivation of Stratton-Chu integrals.

Let us now apply fields equations to the identity (A.64). In vacuum, the field equations read

$$\begin{aligned} \nabla \times \vec{E} &= -\frac{1}{c}\frac{\partial \vec{B}}{\partial t}, \\ \nabla \times \vec{B} &= \frac{1}{c}\frac{\partial \vec{E}}{\partial t}. \end{aligned} \tag{A.65}$$

Taking rotation of both parts of equations in (A.65), one can get wave equations:

$$\begin{aligned} \nabla \times \nabla \times \vec{E} + \frac{1}{c^2}\frac{\partial^2 \vec{E}}{\partial t^2} &= 0, \\ \nabla \times \nabla \times \vec{B} + \frac{1}{c^2}\frac{\partial^2 \vec{B}}{\partial t^2} &= 0, \end{aligned} \tag{A.66}$$

which, in the frequency domain, have form

$$\begin{aligned} \nabla \times \nabla \times \vec{E} - k^2 \vec{E} &= 0, \\ \nabla \times \nabla \times \vec{B} - k^2 \vec{E} &= 0, \end{aligned} \tag{A.67}$$

where $k = \omega/c$, ω being the frequency of the wave mode.

Let us now set in (A.64) $\vec{P} = \vec{E}$ and $\vec{Q} = \psi \cdot \vec{a}$, where $\psi = e^{ikr}/r$, $r = |\vec{r}|$, $\vec{r} = (x - x_0,\, y - y_0,\, z - z_0)$, $(x,\, y,\, z)$ being the point on the surface S, and $\vec{a}$ is a unit vector having some arbitrary direction. As $\vec{a}$ does not depend on $\vec{r}$, then, using vector identities [167]

$$\begin{aligned} &\nabla \times (f\vec{A}) = f\nabla \times \vec{A} + \nabla f \cdot \vec{A}, \\ &\nabla \times (\vec{A} \times \vec{B}) = \vec{A}(\nabla \cdot \vec{B}) - \vec{B}(\nabla \cdot \vec{A}) + (\vec{B} \cdot \nabla)\vec{A} - (\vec{A} \cdot \nabla)\vec{B}, \end{aligned} \tag{A.68}$$

one can get

$$\begin{aligned}
&\nabla \times \vec{Q} = \nabla \times (\psi \cdot \vec{a}) = \nabla\psi \times \vec{a} \\
&\nabla \times \nabla \times \vec{Q} = \nabla \times \nabla \times (\psi \cdot \vec{a}) = \nabla \times (\nabla\psi \times \vec{a}) = \\
&\qquad -\nabla^2\psi\vec{a} + (\vec{a} \cdot \nabla)\nabla\psi = -\nabla^2\Big(\frac{e^{ikr}}{r}\Big)\vec{a} + (\vec{a} \cdot \nabla)\nabla\psi.
\end{aligned} \tag{A.69}$$

It is easy to see that $\nabla^2(e^{ikr}/r) = -k^2 e^{ikr}/r$. Indeed,

$$\begin{aligned}
&\nabla^2\Big(\frac{e^{ikr}}{r}\Big) = \frac{1}{r} \cdot \nabla^2 e^{ikr} + 2\nabla\frac{1}{r} \cdot \nabla e^{ikr} + e^{ikr}\nabla^2\frac{1}{r}, \\
&\nabla e^{ikr} = ik\, e^{ikr}\nabla r, \\
&\nabla^2 e^{ikr} = ik\, e^{ikr}\nabla^2 r - k^2(\nabla r)^2 e^{ikr}, \\
&\nabla\frac{1}{r} = -\frac{\nabla r}{r^2}, \\
&\nabla^2\frac{1}{r} = -\frac{1}{r^2}\nabla^2 r + \frac{2}{r^3}(\nabla r)^2.
\end{aligned} \tag{A.70}$$

Substituting derivatives of r:

$$\begin{aligned}
&\nabla r = \frac{\vec{r}}{r}, \\
&(\nabla r)^2 = 1, \\
&\nabla^2 r = \frac{3r - r^2/r}{r^2} = \frac{2}{r}
\end{aligned} \tag{A.71}$$

into Eq. (A.70), one can get

$$\begin{aligned}
\nabla^2\Big(\frac{e^{ikr}}{r}\Big) = \frac{1}{r} \cdot \big[ik\, e^{ikr}\nabla^2 r - k^2(\nabla r)^2 e^{ikr}\big] - \\
2\frac{\nabla r}{r^2} \cdot ik\, e^{ikr}\nabla r + e^{ikr} \cdot \Big[\frac{2(\nabla r)^2}{r^3} - \frac{\nabla^2 r}{r^2}\Big] = \\
\frac{e^{ikr}}{r}\Big(\frac{2ik}{r} - \frac{2}{r^2} + \frac{2}{r^2} - \frac{2ik}{r} - k^2\Big) = -k^2\frac{e^{ikr}}{r}.
\end{aligned} \tag{A.72}$$

Noting that for a constant $\vec{a}$, $(\vec{a} \cdot \nabla)\nabla\psi = \nabla(\vec{a} \cdot \nabla\psi)$, substituting Eq. (A.72) into Eq. (A.69) and using the first equation in (A.67), one can write

all the terms from left and right sides of Eq. (A.64):

$$\begin{aligned}
&\vec{P} = \vec{E},\\
&\nabla \times \nabla \times \vec{P} = \nabla \times \nabla \times \vec{P} = k^2 \vec{E},\\
&\vec{Q} = \vec{a}\psi,\\
&\nabla \times \nabla \times \vec{Q} = \vec{a} k^2 \, \psi + \nabla(\vec{a} \cdot \nabla\psi),\\
&\vec{P} \times \nabla \times \vec{Q} = \vec{E} \times \nabla \times \vec{a} \cdot \psi,\\
&\vec{Q} \times \nabla \times \vec{P} = \psi \times \nabla \times \vec{E}.
\end{aligned} \tag{A.73}$$

Let us now substitute relations (A.73) into (A.64).

$$\begin{aligned}
\int_V \Big(\cancel{\psi \vec{a} \cdot k^2 \vec{E}} - \cancel{\vec{E} \cdot \vec{a} k^2 \psi} - \vec{E} \cdot \nabla(\vec{a} \cdot \psi)\Big) \mathrm{d}V = \\
\oint_S \Big(\vec{E} \times (\nabla\psi \times \vec{a}) - ik\psi \, \vec{a} \times \vec{B}\Big) \cdot \vec{n} \, \mathrm{d}S,
\end{aligned} \tag{A.74}$$

where $\vec{n}$ is the unit vector looking outside of V. In the right hand side of (A.74), Maxwell equation $\nabla \times \vec{E} = ik \, \vec{B}$ was used. Due to the equality

$$\vec{E} \cdot \nabla f = \nabla(\vec{E} \cdot f) - f \cancelto{0}{\nabla \cdot \vec{E}} = \nabla(\vec{E} \cdot f), \tag{A.75}$$

the left hand side of (A.74) can be transformed as follows:

$$\begin{aligned}
-\int_V \Big(\vec{E} \cdot \nabla(\vec{a} \cdot \nabla\psi)\Big) \mathrm{d}V = -\int_V \nabla\Big(\vec{E} \cdot (\vec{a} \cdot \nabla\psi)\Big) \mathrm{d}V = \\
-\oint_S \Big(\vec{E} \cdot (\vec{a} \cdot \nabla\psi)\Big) \cdot \vec{n} \, \mathrm{d}S = -\oint_S (\vec{a} \cdot \nabla\psi)(\vec{E} \cdot \vec{n}) \, \mathrm{d}S = \\
-\oint_S \vec{a} \cdot \Big((\vec{E} \cdot \vec{n}) \cdot \nabla\psi\Big) \, \mathrm{d}S.
\end{aligned} \tag{A.76}$$

Let us now transform the right hand side of (A.74). First, let us note that

$$\vec{E} \times (\nabla\psi \times \vec{a}) = \nabla\psi \cdot (\vec{E} \cdot \vec{a}) - \vec{a} \cdot (\vec{E} \cdot \nabla\psi). \tag{A.77}$$

In this way,

$$\begin{aligned}
&\oint_S \Big(\vec{E} \times (\nabla\psi \times \vec{a})\Big) \cdot \vec{n}\,\mathrm{d}S = \\
&\oint_S \Big((\nabla\psi \cdot \vec{n})(\vec{E} \cdot \vec{a}) - \vec{a} \cdot (\vec{E} \cdot \nabla\psi) \cdot \vec{n}\Big)\mathrm{d}S = \\
&\oint_S \Big(\vec{a} \cdot \vec{E}(\nabla\psi \cdot \vec{n}) - \vec{a} \cdot (\vec{E} \cdot \nabla\psi) \cdot \vec{n}\Big)\mathrm{d}S = \\
&\oint_S \vec{a} \cdot \Big(\vec{E}(\nabla\psi \cdot \vec{n}) - \vec{n}(\vec{E} \cdot \nabla\psi)\Big)\mathrm{d}S = \\
&\oint_S \vec{a} \cdot \Big(\nabla\psi \times (\vec{E} \times \vec{n})\Big)\mathrm{d}S.
\end{aligned} \tag{A.78}$$

Finally, due to equality $\vec{A} \cdot (\vec{B} \times C) = (\vec{A} \times \vec{B}) \cdot \vec{C}$ [167],

$$\oint_S ik\,\psi(\vec{a} \times \vec{B}) \cdot \vec{n}\,\mathrm{d}S = ik \oint_S \vec{a} \cdot (\vec{B} \times \vec{n})\psi\,\mathrm{d}S. \tag{A.79}$$

Substituting equations (A.76), (A.78) and (A.79) into (A.74), one can obtain the following relation:

$$\oint_S \vec{a} \cdot \Big((\vec{E} \cdot \vec{n}) \cdot \nabla\psi + \nabla\psi \times (\vec{E} \times \vec{n}) - ik\psi(\vec{B} \times \vec{n})\Big)\mathrm{d}S = 0. \tag{A.80}$$

As the vector $\vec{a}$ was supposed to have arbitrary direction, the following vector equation should hold:

$$\oint_S \Big((\vec{E} \cdot \vec{n}) \cdot \nabla\psi + (\vec{n} \times \vec{E}) \times \nabla\psi + ik\psi(\vec{n} \times \vec{B})\Big)\mathrm{d}S = 0. \tag{A.81}$$

Let us recall now that S is composed of A, the outer surface, and that of a sphere of radius δr around the observation point r_0. Let this sphere surface be $A_{\delta r}$. Let us now calculate the part of integral (A.81) over the surface $A_{\delta r}$ for $\delta r \to 0$. As the surface area of the sphere is $4\pi\delta r^2$ and $\psi(r) = \exp(ikr)/r \sim 1/r$, the contribution to the integral of the term $ik\psi(\vec{n} \times \vec{B})$ is zero. On the

other hand,

$$\nabla\psi = \frac{\nabla e^{ikr}}{r} + e^{ikr}\nabla\frac{1}{r} = \nabla r\big(\frac{ik\,e^{ikr}}{r} - \frac{e^{ikr}}{r^2}\big) = \vec{n}\,\frac{e^{ikr}}{r}(ik - \frac{1}{r}). \tag{A.82}$$

For this reason,

$$\begin{aligned}(\vec{E}\cdot\vec{n})\cdot\nabla\psi + (\vec{n}\times\vec{E})\times\nabla\psi = \\ (ik - \frac{1}{\delta r})\frac{e^{ik\delta r}}{\delta r}\Big((\vec{n}\cdot\vec{E})\cdot\vec{n} + (\vec{n}\times\vec{E})\times\vec{n}\Big).\end{aligned} \tag{A.83}$$

Now, it's easy to see that $(\vec{n}\cdot\vec{E})\cdot\vec{n} + (\vec{n}\times\vec{E})\times\vec{n} = \vec{E}$. Indeed, if $(\vec{n}\cdot\vec{E})\cdot\vec{n} + (\vec{n}\times\vec{E})\times\vec{n} = \vec{F}$ then, as this can be easily verified, $\vec{n}\cdot\vec{F} = \vec{n}\cdot\vec{E}$ and $\vec{n}\times\vec{F} = \vec{n}\times\vec{E}$. For this reason, vector $\vec{A} = \vec{F} - \vec{E}$ is both parallel and perpendicular to $\vec{n}$ and therefore is zero. In this way,

$$\begin{aligned}\oint_{S_{\delta r}}\Big((\vec{E}\cdot\vec{n})\cdot\nabla\psi + (\vec{n}\times\vec{E})\times\nabla\psi\Big)\mathrm{d}S = \\ \oint_{S_{\delta r}}\vec{E}\cdot(ik - \frac{1}{\delta r})\cdot\frac{e^{ik\delta r}}{\delta r}\,\mathrm{d}S \underset{\delta r\to 0}{\longrightarrow} -\vec{E}(\vec{r}_0)\frac{\oint_{S_{\delta r}}\mathrm{d}S}{\delta_r^2} = -4\pi\vec{E}(\vec{r}_0).\end{aligned} \tag{A.84}$$

Substituting (A.84) into Eq. (A.81) one obtains the first Stratton-Chu integral for the continuous source on surface A:

$$\vec{E}(\vec{r}_0) = \frac{1}{4\pi}\oint_A\Big((\vec{n}\cdot\vec{E})\nabla\psi + (\vec{n}\times\vec{E})\times\nabla\psi + ik\psi(\vec{n}\times\vec{B})\Big)\mathrm{d}S. \tag{A.85}$$

Equation (A.85) gives an integral representation of the Fourier component with frequency $\omega = kc$ of the electric field component at the point $\vec{r}$. If the fields on the surface depend on time through $e^{i\omega t}$, then (A.85) holds in the time domain as well.

Taking $\vec{P} = \vec{B}$ in (A.64) and repeating the steps shown above gives the

second Stratton-Chu integral, for the field $\vec{B}$:

$$\vec{B}(\vec{r_0}) = \frac{1}{4\pi}\oint_A \Big(-(\vec{n}\cdot\vec{B})\nabla\psi - (\vec{n}\times\vec{B})\times\nabla\psi + ik\psi(\vec{n}\times\vec{E})\Big)\mathrm{d}S. \quad \text{(A.86)}$$

The integrals (A.85) and (A.86) are the solutions to the Maxwell equations provided the fields $\vec{E}$ and $\vec{B}$ are continuous on the integration surface A. This statement is generalized in [109] where it is shown that if the tangential components of the fields $\vec{E}$ and $\vec{B}$ suffer a discontinuity on a contour C and the fields are continuous everywhere else on the A then the following expression is the solution to the Maxwell equations:

$$\begin{aligned}
\vec{E}(\vec{r_0}) = \frac{1}{4\pi}\oint_{A'} [ik(\vec{n}\times\vec{B}_s)\psi + (\vec{n}\times\vec{E}_s)\times\nabla\psi + \\
(\vec{n}\cdot\vec{E}_s)\nabla\psi]\mathrm{d}S + \frac{1}{4\pi ik}\oint_C \nabla\psi(\vec{B}_l\cdot\mathrm{d}\vec{l}), \\
\vec{B}(\vec{r_0}) = \frac{1}{4\pi}\oint_{A'} [ik(\vec{E}_s\times\vec{n})\psi + (\vec{n}\times\vec{B}_s)\times\nabla\psi + \\
(\vec{n}\cdot\vec{B}_s)\nabla\psi]\mathrm{d}S - \frac{1}{4\pi ik}\oint_C \nabla\psi(\vec{E}_l\cdot\mathrm{d}\vec{l}),
\end{aligned} \quad \text{(A.87)}$$

where $\vec{E}_s$, $\vec{B}_s$ are field values on the surface A' and $\vec{E}_l$, $\vec{B}_l$ are difference between those to the right and to the left of the contour C. Equation (A.87) gives the complete set of Stratton-Chu integrals.

Appendix B

Plasma expansion

B.1 Self-similar expansion of isothermal 1D planar plasma into vacuum

At time $t = 0$, the planar plasma is supposed to occupy the half of the space. At $t > 0$ the hot electrons try to escape plasma and thus create a nonzero electrostatic field which slows them down and pushes ions from plasma. Let x be the space coordinate. The hydrodynamic equations describing evolution of particle density n_i of ions and their velocity v_i are

$$\begin{aligned} &\frac{\partial n_i}{\partial t} + \frac{\partial}{\partial x}(n_i v_i) = 0, \\ &\frac{\partial v_i}{\partial t} + v_i \frac{\partial v_i}{\partial x} = -\frac{Ze}{m_i}\frac{\partial \Phi}{\partial x}. \end{aligned} \tag{B.1}$$

In Eq. (B.1), the first equation is the continuity equation and the second one is the equation of motion. Ze is the charge of ions, m_i their mass and Φ is the electrostatic potential. The hydrodynamic closure is provided by the conditions of hydrodynamic equilibrium, resulting in Boltzmann relation for

electron particle density,

$$n_e = n_0 \exp\left(e\Phi/T_e\right), \tag{B.2}$$

quasi-neutrality,

$$n_e = Z n_i, \tag{B.3}$$

and isothermality,

$$T_e = const, \tag{B.4}$$

where T_e is the electron temperature.

To find out the dynamics of expansion, one, in principle, needs to solve Cauchy problem with differential equations given by Eq. (B.1) and the appropriate boundary conditions. This is a complicated problem to solve. It was found, however [70], that Eq. (B.1) admits a self-similar solution. To obtain such a solution one supposes that at large times all the hydrodynamic parameters depend on t and x only via combination x/t. In this way, a new variable ξ, called self-similar variable, is introduced:

$$\xi = \frac{1}{c_s}\frac{x}{t}, \tag{B.5}$$

where c_s is speed of sound in plasma, which, for the cold ions, is

$$c_s = \sqrt{\frac{ZT_e}{m_i}}. \tag{B.6}$$

Introducing also normalized variables

$$\begin{aligned} u &= \frac{v_i}{c_s}, \\ \phi &= \frac{e\Phi}{T_e}, \end{aligned} \tag{B.7}$$

one can rewrite the continuity equation as

$$-\frac{x}{c_s t^2}\frac{\mathrm{d}n_i}{\mathrm{d}\xi}+\frac{1}{c_s t}\frac{\mathrm{d}}{\mathrm{d}\xi}(n_i v_i)=0, \tag{B.8}$$

or

$$-\xi\frac{\mathrm{d}n_i}{\mathrm{d}\xi}+\frac{\mathrm{d}}{\mathrm{d}\xi}(n_i u)=0. \tag{B.9}$$

In the same way, the equation of motion of plasma becomes

$$(u-\xi)\frac{\mathrm{d}u}{\mathrm{d}\xi}=-\frac{\mathrm{d}\phi}{\mathrm{d}\xi}. \tag{B.10}$$

Using Eq. (B.2), the following equation is easily obtained:

$$\frac{1}{n_i}\frac{\mathrm{d}n_i}{\mathrm{d}\xi}=\frac{\mathrm{d}\phi}{\mathrm{d}\xi}. \tag{B.11}$$

Introducing variable $\nu = \ln n_i$ and substituting (B.11) into (B.10), one can derive from Eqs. (B.8), (B.10) the following closed system of equations:

$$\begin{aligned}(u-\xi)\frac{\mathrm{d}u}{\mathrm{d}\xi}&=-\frac{\mathrm{d}\nu}{\mathrm{d}\xi},\\ (u-\xi)\frac{\mathrm{d}\nu}{\mathrm{d}\xi}&=-\frac{\mathrm{d}u}{\mathrm{d}\xi}.\end{aligned} \tag{B.12}$$

Substituting $\mathrm{d}\nu/\mathrm{d}\xi$ from the first equation in (B.12) into the second one, an expression for u is obtained:

$$(u-\xi)^2=1. \tag{B.13}$$

A detailed analysis carried out in [70] has shown that the negative root should

be dismissed, and thus the only valid solution is

$$u = \xi + 1. \tag{B.14}$$

Substituting Eq. (B.14) into (B.12) and using boundary condition $n_i(-1) = n_0$, one can get the solution for ν:

$$\nu = -\xi + 1. \tag{B.15}$$

Returning back to the physical variables, the self-similar solution to the hydrodynamical equations in isothermal equilibrium case is

$$\begin{aligned} n_i(x,t) &= n_0 \exp\left(-\frac{x}{c_s t} + 1\right), \\ v_i(x,t) &= c_s + \frac{x}{t}. \end{aligned} \tag{B.16}$$

B.2 Equations of r and v_r of a particle in a central field

In this Section, the equation for r and v_r of a particle in a central field are derived which are needed for understanding work of the electrostatic spherical 1D code used in Chapter 3. For simplicity, the derivation is carried out in a plane XY; the equations of motion in an arbitrary plane can be obtained by using the corresponding rotation and appear to have exactly the same form.

Let there be a central force F_r. Equation of motion of a particle under

action of this force in the Cartesian coordinates are

$$\begin{aligned}
\frac{\mathrm{d}x}{\mathrm{d}t} &= v_x, \\
\frac{\mathrm{d}y}{\mathrm{d}t} &= v_y, \\
m\frac{\mathrm{d}v_x}{\mathrm{d}t} &= F_x = \frac{x}{r}F_r(r), \\
m\frac{\mathrm{d}v_y}{\mathrm{d}t} &= F_y = \frac{y}{r}F_r(r),
\end{aligned} \tag{B.17}$$

where

$$r = \sqrt{x^2 + y^2}. \tag{B.18}$$

Let the angle between $\vec{r}$ and OX axis be α and the one between $\vec{r}$ and $\vec{v}$ be β (see Fig. B.1). Then the angle between $\vec{v}$ and OX axis is $\alpha + \beta$. In this way,

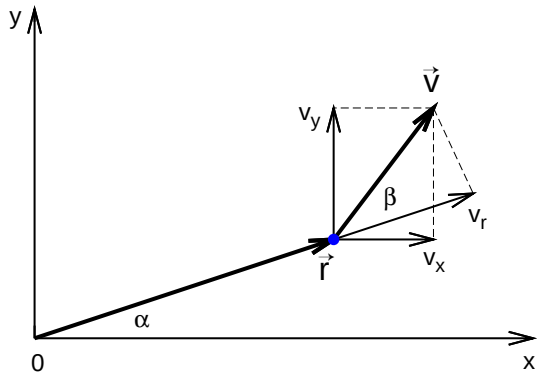

Figure B.1: Geometry of particle position and velocity.

$$\begin{aligned}
v_x &= v\cos(\alpha+\beta) = v(\cos\alpha\cos\beta - \sin\alpha\sin\beta), \\
v_y &= v\sin(\alpha+\beta) = v(\sin\alpha\cos\beta + \cos\alpha\sin\beta).
\end{aligned} \tag{B.19}$$

Therefore, a quantinity $v_x \cos\alpha + v_y \sin\alpha$ is

$$\begin{aligned} & v_x \cos\alpha + v_y \sin\alpha = \\ & v\cos\alpha(\cos\alpha\cos\beta - \sin\alpha\sin\beta) + \\ & v\sin\alpha(\sin\alpha\cos\beta + \cos\alpha\sin\beta) = \\ & v[\cos^2\alpha\cos\beta - \sin\alpha\sin\beta\cos\alpha + \\ & \sin^2\alpha\cos\beta + \sin\alpha\sin\beta\cos\alpha] = \\ & v\cos\beta(\cos^2\alpha + \sin^2\alpha) = v\cos\beta = v_r. \end{aligned} \tag{B.20}$$

I.e.,

$$v_r = v_x \cos\alpha + v_y \sin\alpha. \tag{B.21}$$

Thus,

$$\begin{aligned} & \frac{\mathrm{d}r}{\mathrm{d}t} = \frac{\mathrm{d}}{\mathrm{d}t}\sqrt{x^2+y^2} = \frac{1}{r}\Big(x\frac{\mathrm{d}x}{\mathrm{d}t} + y\frac{\mathrm{d}y}{\mathrm{d}t}\Big) = \\ & \frac{x}{r}v_x + \frac{y}{r}v_y = v_x\cos\alpha + v_y\sin\alpha = v_r, \end{aligned} \tag{B.22}$$

or

$$\frac{\mathrm{d}r}{\mathrm{d}t} = v_r. \tag{B.23}$$

Let us find now equation for v_r:

$$\begin{aligned} & \frac{\mathrm{d}v_r}{\mathrm{d}t} = \frac{\mathrm{d}}{\mathrm{d}t}\Big(\frac{x}{r}v_x + \frac{y}{r}v_y\Big) = \frac{\mathrm{d}}{\mathrm{d}t}\frac{xv_x + yv_y}{r} = \\ & \frac{r\mathrm{d}(xv_x)/\mathrm{d}t - v_r x v_x + r\mathrm{d}(yv_y)/\mathrm{d}t - v_r y v_y}{r^2} = \\ & \frac{r(v_x^2 + x\dot{v}_x) - v_r x v_x + r(v_y^2 + y\dot{v}_y) - v_r y v_y}{r^2} = \\ & \frac{1}{r}\cdot\big(v_x^2 + v_y^2 + x\dot{v}_x + y\dot{v}_y\big) - \frac{v_r}{r^2}(xv_x + yv_y). \end{aligned} \tag{B.24}$$

The 3-rd and 4-th terms in Eq. (B.24) are easily recognizable:

$$\frac{1}{r}(x\dot{v}_x + y\dot{v}_y) = \frac{1}{mr^2}(x^2F_r + y^2F_r) = \frac{F_r}{m}. \tag{B.25}$$

The remaining terms in Eq. (B.24) can be evaluated as

$$\frac{v_x^2 + v_y^2}{r} - \frac{x v_x v_r + y v_y v_r}{r^2} = \frac{v^2}{r} - \frac{v_r^2}{r} = \frac{v^2 \sin^2 \beta}{r}, \tag{B.26}$$

where Eq. (B.21) was used to simplify $(x v_x + y v_y)/r$. If one substitutes the expression for the square of angular momentum

$$l^2 = m^2 r^2 v^2 \sin^2 \beta \tag{B.27}$$

into the right hand side of Eq. (B.26), he easily gets

$$\frac{v_x^2 + v_y^2}{r} - \frac{x v_x v_r + y v_y v_r}{r^2} = \frac{1}{r^3}\Big(\frac{l}{m}\Big)^2. \tag{B.28}$$

This equation defines so-called pseudo-force acting on the particle. It appears from transformation into the spherical coordinates and presents even if the interaction potential is zero. Substituting Eqs. (B.28) and (B.25) into Eq. (B.24) one finally obtains

$$\frac{\mathrm{d}v_r}{\mathrm{d}t} = \frac{1}{m} F_r + \frac{1}{r^3}\Big(\frac{l}{m}\Big)^2. \tag{B.29}$$

Equations (B.23) and (B.29) define the evolution of phase space coordinates r and v_r of the particle in time.

B.3 Coulomb explosion of a uniformly charged sphere

A uniformly charged sphere of radius R has the following dependence of charge density on the radius r at $t = 0$:

$$\rho(r,0) = \begin{cases} \rho_0 \text{ if } r \le R, \\ 0 \text{ otherwise.} \end{cases} \tag{B.30}$$

It is supposed that the explosion dynamics is collisionless and governed by the Vlasov equation. The characteristics of the Vlasov equation in the case of zero initial temperature of particles are

$$\begin{aligned} \frac{\mathrm{d}r}{\mathrm{d}t} &= v_r, \\ \frac{\mathrm{d}v_r}{\mathrm{d}t} &= \frac{q}{M} E_r(r,t). \end{aligned} \tag{B.31}$$

The electrostatic field E_r can be evaluated by the Gauss theorem:

$$E_r(r,t) = Q_{enc}/r^2. \tag{B.32}$$

If there are no multi-flows, i.e., if for any two characteristics having coordinates $r_1(t)$ and $r_2(t)$,

$$\begin{aligned} r_1(t) > r_2(t) \Leftrightarrow r_1(0) > r_2(0), \\ r_1(t) < r_2(t) \Leftrightarrow r_1(0) < r_2(0) \end{aligned} \tag{B.33}$$

for any t, then the value of Q_{enc} is just the one at $t = 0$:

$$Q_{enc} = \frac{4\pi}{3} n_0 r_0^3, \tag{B.34}$$

where r_0 is the starting position of the given characteristic. In the following discussion, the absence of multi-flows will be supposed a priori and justified later after the solution is found.

Denoting $K = qQ_{enc}/M$, Eqs. (B.31), (B.32) can be rewritten as

$$\frac{\mathrm{d}^2 r}{\mathrm{d}t^2} = \frac{K}{r^2}. \tag{B.35}$$

Multiplying both sides of Eq. (B.35) by $\mathrm{d}r/\mathrm{d}t$, one gets

$$\frac{1}{2}\frac{\mathrm{d}}{\mathrm{d}t}\Big(\frac{\mathrm{d}r}{\mathrm{d}t}\Big)^2 = \frac{\mathrm{d}r}{\mathrm{d}t}\frac{K}{r^2} = -\frac{\mathrm{d}}{\mathrm{d}t}\frac{K}{r}. \tag{B.36}$$

Integrating of Eq. (B.36) once by time gives

$$\Big(\frac{\mathrm{d}r}{\mathrm{d}t}\Big)^2 = 2K\Big(\frac{1}{r_0} - \frac{1}{r}\Big), \tag{B.37}$$

or

$$\frac{\mathrm{d}r}{\mathrm{d}t} = 2K\sqrt{\frac{1}{r_0} - \frac{1}{r}}. \tag{B.38}$$

Eq. (B.38) is an equation with separating variables and can be integrated:

$$\int_{r_0}^{r} \mathrm{d}r \sqrt{\frac{r}{r - r_0}} = \sqrt{\frac{2K}{r_0}} \int_0^t \mathrm{d}t. \tag{B.39}$$

The integral on the left hand side of Eq. (B.39) evaluates to

$$\int_{r_0}^{r} \mathrm{d}r \sqrt{\frac{r}{r - r_0}} = \frac{1}{4}\Big(2\sqrt{r(r - r_0)} - r_0 \log\big[\frac{r_0}{(\sqrt{r - r_0} + \sqrt{r})^2}\big]\Big). \tag{B.40}$$

Thus, the dependence $r(t)$ for every characteristic of Vlasov equation is given

by implicit formula

$$\frac{1}{4}\Big(2\sqrt{r(r-r_0)} - r_0 \log\big[\frac{r_0}{(\sqrt{r-r_0}+\sqrt{r})^2}\big]\Big) = \sqrt{\frac{2K}{r_0}}t. \tag{B.41}$$

The solution (B.41) can be written in parametric form. Choosing s as a parameter and transforming to the dimensionless coordinates with the same units as in Chapter 3, the solution to the equation (B.35) is

$$\begin{aligned} &r(s,h) = s + h, \\ &t(s,h) = \frac{1}{h\sqrt{6}}\Big(\sqrt{s(s+h)} - h\log\big[\frac{h}{(\sqrt{s}+\sqrt{s+h})^2}\big]\Big), \\ &h,\ s \geq 0, \end{aligned} \tag{B.42}$$

where $h = r_0/R$ is the dimensionless starting position of the characteristic. The complete solution to (B.31) also needs a dependence $v_r(t)$ which, however, is currently of no interest. The parametric dependencies (B.42) are shown graphically in Fig. B.2.

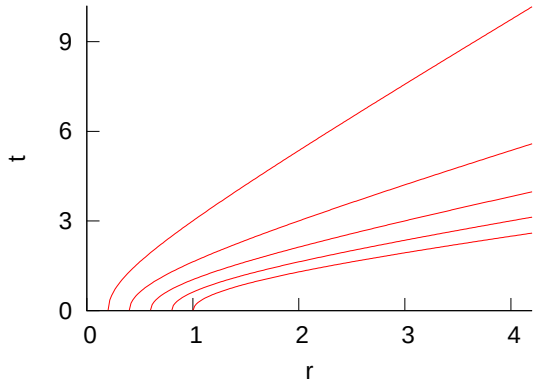

Figure B.2: Projections of the family of characteristics onto the r, t plane.

The curves in Fig. B.2 never cross. Therefore, the condition (B.33) which is satisfied at $t = +0$ (due to the monotonic increase of E_r inside the sphere), is never violated later. In other words, characteristics start at $r = h$ in the

state of absence of multi-flows and thus their trajectories should coincide with the curves in Fig. B.2 unless multi-flows start. Since the curves never cross, the multi-flows never appear for the density profile (B.30), and Eq. (B.42) represents a correct solution.

Analytical inverting of Eq. (B.41) is a difficult task. It can, however, be done numerically. The result of numerical inversion proves the following. If Δh_1 and Δh_2 are distances between starting points of any two pairs of characteristics and Δr_1, Δr_2 are the corresponding distances at $t > 0$ then the following relation holds:

$$\frac{\Delta r_2}{\Delta r_1} = \frac{\Delta h_2}{\Delta h_1}. \tag{B.43}$$

In other words, if the density of characteristics projections onto the r axis is constant at $t = 0$, it is constant at $t > 0$. Every characteristic follows an element $\mathrm{d}r\mathrm{d}v_r$ containing $\mathrm{d}N = f(t = 0)\mathrm{d}r\mathrm{d}v_r$ particles. However, the constant density of characteristics projections onto the r axis correspond to the constant charge density, since $n(t = 0) = n_0$ inside the sphere. For this reason, the charge density profile function preserves its uniform dependence on coordinates, with the value of density being

$$n_0\big(t(s)\big) = n_0 \cdot \frac{r^3(s,1)}{R^3}, \tag{B.44}$$

where $r(s,1)$ is the coordinate of the boundary of the sphere given by Eq. (B.42), with $h = 1$.

Bibliography

[1] E. M. McMillan, "The origin of cosmic rays", *Phys. Rev.* **79**, 498 (1950).

[2] Y. W. Chan, "Ultra-intense laser radiation as a possible energy booster for relativistic charged particle", *Phys. Lett.* **35A**, 305 (1971).

[3] D. Strickland and G. Mourou, "Compression of amplified chirped optical pulses", *Opt. Comm.* **56**, 219 (1985).

[4] G. Mourou and D. Umstadter, "Development and applications of compact high-intensity lasers", *Phys. Fluids B* **4**, 2315 (1992).

[5] M. D. Perry and G. Mourou, "Terawatt to petawatt subpicosecond lasers", *Science* **264**, 917 (1994).

[6] M. D. Perry, D. Pennington, B. C. Stuart, G. Tietbohl, J. A. Britten, C. Brown, S. Herman, B. Golick, M. Kartz, J. Miller, H. T. Powell, M. Vergino, and V. Yanovsky, "Petawatt laser pulses", *Opt. Lett.* **24**, 160 (1999).

[7] T. Tajima, G. Mourou, "Zettawatt-exawatt lasers and their applications in ultrastrong-field physics", *Phys. Rev. ST AB* **5**, 031301 (2002).

[8] S.-W. Bahk, P. Rousseau, T. A. Planchon, V. Chvykov, G. Kalintchenko, A. Maksimchuk, G. A. Mourou, and V. Yanovsky, "Generation and char-

acterization of the highest laser intensities ($10^{22}\,\mathrm{W/cm^2}$)", *Opt. Lett.* **29**, 2837 (2004).

[9] Ed Gerstner, "Laser physics: Extreme light", *Nature* **446**, 16 (2007).

[10] M. Tabak, J. Hammer, M. E. Glinsky, W. L. Kruer, S. C. Wilks, J. Woodworth, E. M. Campbell, and M. D. Perry, "Ignition and high gain with ultrapowerful lasers", *Phys. Plasmas* **1**, 1626 (1994).

[11] M. Tabak, D. S. Clark, S. P. Hatchett, M. H. Key, B. F. Lasinski, R. A. Snavely, S. C. Wilks, R. P. J. Town, R. Stephens, E. M. Campbell, R. Kodama, K. Mima, and K. A. Tanaka, "Review of progress in Fast Ignition", *Phys. Plasmas* **12**, 057305 (2005).

[12] Y. Sentoku, K. Mima, T. Taguchi, S. Miyamoto, Y. Kishimoto, "Particle simulation on x-ray emissions from ultra-intense laser produced plasmas", *Phys. Plasmas* **5**, 4366 (1998).

[13] P. A. Norreys, M. Santala, E. Clark, M. Zepf, I. Watts, F. N. Beg, K. Krushelnick, M. Tatarakis, A. E. Dangor, X. Fang, P. Graham, T. McCanny, R. P. Singhal, and K. W. D. Ledingham, "Observation of a highly directional gamma-ray beam from ultrashort, ultraintense laser pulse interactions with solids", *Phys. Plasmas* **6**, 2150 (1998).

[14] D.A Jaroszynski, R. Bingham, E. Brunetti, B. Ersfeld, J. Gallacher, B. van der Geer, R. Issac, S.P. Jamison, D. Jones, M. de Loos, A. Lyachev, V. Pavlov, A. Reitsma, Y. Saveliev, G. Vieux and S.M. Wiggins, "Radiation sources based on laserplasma interactions", *Phil. Trans. R. Soc. A* **364**, 689 (2006).

[15] K. Nakajima, "Compact X-ray sources: Towards a table-top free-electron laser", *Nature* **4**, 92 (1998).

[16] P. Burns, N. H. Drewell and J. McKeown, "The measurement, control, and validation of critical parameters in an electron beam sterilization facility", *Nucl. Inst. Met. B* **113**, 96 (1996).

[17] D.I. Martin, I.Margaritescu, E.Cirstea, I.Togoe, D.Ighigeanu, M.R. Nemtanua, C.Oproiu, N.Iacob, "Application of accelerated electron beam and microwave irradiation to biological waste treatment", *Vacuum* **77**, 501 (2005).

[18] V. Yu. Bychenkov, V. T. Tikhonchuk, and S. V. Tolokonnikov, "Nuclear reactions triggered by laser-accelerated high-energy ions", *JETP* **88**, 1137 (1999).

[19] T. Ditmire, J. Zweiback, V. P. Yanovsky, T. E. Cowan, G. Hays, and K. B. Wharton, "Nuclear fusion from explosions of femtosecond laser-heated deuterium clusters", *Nature* **398**, 489 (1999).

[20] J. Zweiback, R. A. Smith, T. E. Cowan, G. Hays, K. B. Wharton, V. P. Yanovsky, and T. Ditmire, "Nuclear Fusion Driven by Coulomb Explosions of Large Deuterium Clusters", *Phys. Rev. Lett.* **84**, 2634 (2000).

[21] I. Last and J. Jortner, "Nuclear Fusion induced by Coulomb Explosion of Heteronuclear Clusters", *Phys. Rev. Lett.* **87**, 033401 (2001).

[22] G. Grillon, Ph. Balcou, J.- P. Chambaret, D. Hulin, J. Martino, S. Moustaizis, L. Notebaert, M. Pittman, Th. Pussieux, A. Rousse, J-Ph. Rousseau, S. Sebban, O. Sublemontier, and M. Schmidt, "Deuterium-Deuterium Fusion Dynamics in Low-Density Molecular-Cluster Jets Irradiated by Intense Ultrafast Laser Pulses", *Phys. Rev. Lett.* **89**, 065005 (2002).

[23] K. W. D. Ledingham, P. McKenna, R. P. Singha, "Applications for Nuclear Phenomena Generated by Ultra-Intense Lasers", *Science* **300**, 1107 (2003).

[24] S. Ter-Avetisyan, M. Schnürer, D. Hilscher, and U. Jahnke, "Fusion neutron yield from a laser-irradiated heavy-water spray", *Phys. Plasmas* **12**, 012702 (2005).

[25] I. Last and J. Jortner, "Tabletop Nucleosynthesis Driven by Cluster Coulomb Explosion", *Phys. Rev. Lett.* **97**, 173401 (2006).

[26] J. A. Cobble, R. P. Johnson, T. E. Cowan, and N. Renard-Le Galloudec, "High resolution laser-driven proton radiography", *J. Appl. Phys.* **92**, 1775 (2002).

[27] F. P. Boody, R. Höpfl, H. Hora and J. C. Kelly, "Laser-driven ion source for reduced-cost implantation of metal ions for strong reduction of dry friction and increased durability", *Las. Part. Beams*, **14**, 443 (1996).

[28] V. Yu. Bychenkov, W. Rozmus, A. Maksimchuk, D. Umstadter and C. E. Capjack, "Fast Ignitor Concept with Light Ions", *Plasma Phys. Rep.* **27**, 1017 (2001).

[29] M. Roth, T. E. Cowan, M. H. Key, S. P. Hatchett, C. Brown, W. Fountain, J. Johnson, D. M. Pennington, R. A. Snavely, S. C. Wilks, K. Yasuike, H. Ruhl, F. Pegoraro, S. V. Bulanov, E. M. Campbell, M. D. Perry, and H. Powell, "Fast Ignition by Intense Laser-Accelerated Proton Beams", *Phys. Rev. Lett.* **86**, 436 (2001).

[30] M. Temporal, J. J. Honrubia, and S. Atzeni, "Numerical study of fast ignition of ablatively imploded deuteriumtritium fusion capsules by ultra-intense proton beams", *Phys. Plasmas* **9**, 3098 (2002).

[31] M. Temporal, "Fast ignition of a compressed inertial confinement fusion hemispherical capsule by two proton beams", *Phys. Plasmas* **13**, 122704 (2006).

[32] M. H. Key, "Status of and prospects for the fast ignition inertial fusion concept", *Phys. Plasmas* **14**, 055502 (2007).

[33] K. W. D. Ledingham, P. McKenna, T. McCanny, S. Shimizu, J. M. Yang, L. Robson, J. Zweit, J. M. Gillies, J. Bailey, G. N. Chimon, R. J. Clarke, D. Neely, P. A. Norreys, J. L. Collier, R. P. Singhal, M. S. Wei, S. P. D. Mangles, P. Nilson, K. Krushelnick and M. Zepf, "High power laser production of short-lived isotopes for positron emission tomography", *J. Phys. D* **37**, 2341 (2004).

[34] E. Fourkal, B. Shahine, M. Ding, J. Li, T. Tajima, and C.-M. Ma, "Particle in cell simulation of laser-accelerated proton beams for radiation therapy", *Med. Phys.* **29**, 2788 (2002).

[35] S. Bulanov and V. Khoroshkov, "Feasibility of Using Laser Ion Accelerators in Proton Therapy", *Plasma Phys. Rep.* **28**, 453 (2002).

[36] K. W. D. Ledingham, W. Galster, and R. Sauerbrey, "Laser-driven proton oncology – a unique new cancer therapy?", *Brit. J. Radiol.* **80**, 855 (2007).

[37] J. H. Eberly, A. Sleeper, "Trajectory and mass shift of a classical electron in a radiation pulse", *Phys. Rev.* **176**, 1570 (1968).

[38] R. B. Palmer, "Interaction of relativistic particles and free electromagnetic waves in the presence of a static helical magnet", *J. Appl. Phys.* **43**, 3014 (1972).

[39] E. D. Courant, C. Pellegrini, and W. Zakowicz, "High-energy inverse free-electron-laser accelerator", *Phys. Rev. A* **32**, 2813 (1985).

[40] E. Esarey, P. Sprangle, J. Krall, and A. Ting, "Overview of Plasma-Based Accelerator Concepts", *IEEE Trans. Plasma Sci.* **24**, 252 (1996).

[41] T. Tajima and J. M. Dawson, "Laser electron acceleration", *Phys. Rev. Lett.* **43**, 267 (1979).

[42] T. Katsouleas and J. M. Dawson, "Unlimited electron acceleration in laser-driven plasma waves", *Phys. Rev. Lett.* **51**, 392 (1983).

[43] C. Joshi, W. B. Mori, T. Katsouleas, J. M. Dawson, J. M. Kindel, and D. M. Forslund, "Ultrahigh gradient particle acceleration by intense laser-driven plasma density waves", *Nature* **311**, 525 (1984).

[44] C. E. Clayton, K. A. Marsh, A. Dyson, M. Everett, A. Lal, W. P. Leemans, R. Williams, and C. Joshi, "Ultrahigh-gradient acceleration of injected electrons by laser-excited relativistic electron plasma waves", *Phys. Rev. Lett.* **70**, 37 (1993).

[45] P. Sprangle, E. Esarey, A. Ting, and G. Joyce, Laser wakefield acceleration and relativistic optical guiding, *Appl. Phys. Lett.* **53**, 2146 (1988).

[46] P. Sprangle, E. Esarey, J. Krall, and G. Joyce, Propagation and guiding of intense laser pulses in plasmas, *Phys. Rev. Lett.* **69**, 2200 (1992).

[47] S. V. Bulanov, F. Pegoraro, A. M. Pukhov, and A. S. Sakharov, "Transverse-Wake Wave Breaking", *Phys. Rev. Lett.* **78**, 4205 (1997).

[48] A. Modena, Z. Najmudin, A. E. Dangor, C. E. Clayton, K. A. Marsh, C. Joshi, V. Malka, C. B. Darrow, C. Danson, D. Neely, and F.

N. Walsh, "Electron acceleration from the wavebreaking of relativistic plasma waves", *Nature* **377**, 606 (1995).

[49] V. Malka, S. Fritzler, E. Lefebvre, M.-M. Aleonard, F. Burgy, J.-P. Chambaret, J.-F. Chemin, K. Krushelnick, G. Malka, S. P. D. Mangles, Z. Najmudin, M. Pittman, J.-P. Rousseau, J.-N. Scheurer, B. Walton, A. E. Dangor, "Electron Acceleration by a Wake Field Forced by an Intense Ultrashort Laser Pulse", *Science* **298**, 1596 (2002).

[50] A. Pukhov, "Strong field interaction of laser radiation", *Rep. Prog. Phys.* **65**, R1 (2003).

[51] S. P. D. Mangles, C. D. Murphy, Z. Najmudin, A. G. R. Thomas, J. L. Collier, A. E. Dangor, E. J. Divall, P. S. Foster, J. G. Gallacher, C. J. Hooker, D. A. Jaroszynski, A. J. Langley, W. B. Mori, P. A. Norreys, F. S. Tsung, R. Viskup, B. R. Walton, and K. Krushelnick, "Monoenergetic beams of relativistic electrons from intense laserplasma interactions", *Nature* **431**, 535 (2004).

[52] C. G. R. Geddes, Cs. Toth, J. van Tilborg, E. Esarey, C. B. Schroeder, D. Bruhwiler, C. Nieter, J. Cary and W. P. Leemans, "High-quality electron beams from a laser wakefield accelerator using plasma-channel guiding", *Nature* **431**, 538 (2004).

[53] J. Faure, Y. Glinec, A. Pukhov, S. Kiselev, S. Gordienko, E. Lefebvre, J.-P. Rousseau, F. Burgy, and V. Malka, "A laserplasma accelerator producing monoenergetic electron beams", *Nature* **431**, 541 (2004).

[54] W. P. Leemans, B. Nagler, A. J. Gonsalves, Cs. Tóth, K. Nakamura, C. G. R. Geddes, E. Esarey, C. B. Schroeder and S. M. Hooker, "GeV

electron beams from a centimetre-scale accelerator", *Nat. Phys.* **2**, 696 (2006).

[55] J. R. Fontana, R. H. Pantell, "A high-energy, laser accelerator for electrons using the inverse Cherenkov effect", *J. Appl. Phys.* **54**, 4285 (1983).

[56] P. Sprangle, E. Esarey, and J. Krall, "Laser driven electron acceleration in vacuum, gases, and plasmas", *Phys. Plasmas* **3**, 2183 (1996).

[57] C. J. McKinstrie and E. A. Startsev, "Electron acceleration by a laser pulse in a plasma", *Phys. Rev E* **54**, R1070 (1996).

[58] M. O. Scully, M. S. Zubairy, "Simple laser accelerator: optics and particle dynamics", *Phys. Rev. A* **44**, 2656 (1991).

[59] F. V. Hartemann, S. H. Fochs, G. P. Le Sage, N. C. Luhmann, Jr., J. G. Woodworth, M. D. Perry, Y. J. Chen, A. K. Kerman, "Nonlinear ponderomotive scattering of relativistic electrons by an intense laser field at focus", *Phys. Rev. E* **51**, 4833 (1995).

[60] B. Quesnel and P. Mora, "Theory and simulation of the interaction of ultraintense laser pulses with electrons in vacuum", *Phys. Rev. E* **58**, 3719 (1998).

[61] S. V. Stupakov, M. S. Zolotorev, "Ponderomotive Laser Acceleration and Focusing in Vacuum for Generation of Attosecond Electron Bunches", *Phys. Rev. Lett.* **86**, 5274 (2001).

[62] Y. I. Salamin, C. H. Keitel, "Electron Acceleration by a Tightly Focused Laser Beam", *Phys. Rev. Lett.* **88**, 095005 (2002).

[63] K. I. Popov, V. Yu. Bychenkov, W. Rozmus, and R. D. Sydora, "Electron vacuum acceleration by a tightly focused laser pulse", *Phys. Plasmas* **15**, 013108 (2008).

[64] E. Esarey, P. Sprangle, J. Krall, "Laser acceleration of electrons in vacuum", *Phys. Rev. E* **52**, 5443 (1995).

[65] W. Yu, V. Bychenkov, Y. Sentoku, M.Y. Yu, Z. M. Sheng, and K. Mima, "Electron Acceleration by a Short Relativistic Laser Pulse at the Front of Solid Targets", *Phys. Rev. Lett.* **85**, 570 (2000).

[66] S. X. Hu and A. F. Starace, "GeV Electrons from Ultraintense Laser Interaction with Highly Charged Ions", *Phys. Rev. Lett.* **88**, 245003 (2002).

[67] S. X. Hu and A. F. Starace, "Laser acceleration of electrons to giga-electron-volt energies using highly charged ions", *Phys. Rev. E* **73**, 066502 (2006).

[68] K. I. Popov, V. Yu. Bychenkov, W. Rozmus, R. D. Sydora, and S. S. Bulanov, "Vacuum electron acceleration by tightly focused laser pulses with nanoscale targets", *Phys. Plasmas* **16**, 053106 (2009).

[69] Z. Huang, G. Stupakov, and M. Zolotorev, "Calculation and optimization of laser acceleration in vacuum", *PHYS. Rev. STAB* **7**, 011302 (2004).

[70] A. V. Gurevich, L. V. Pariskaya, L. P. Pitaevsky, "Self-sinilar motion of rarefied plasma", *Sov. Phys. JETP* **22**, 449 (1966).

[71] F. S. Felber, R. Decoste, "Fast expansions of laser-heated plasmas", *Phys. Fluids* **21**, 530 (1978).

[72] A. Gurevich, D. Anderson, and H. Wilhelmsson, "Ion acceleration in an expanding rarefied plasma with non-Maxwellian electrons", *Phys. Rev. Lett.* **42**, 769 (1979).

[73] A. V. Gurevich, A. P. Mescherkin, "Ion acceleration in spherical plasma expansion", *Sov. J. Plasma Phys.* **9**, 556 (1983).

[74] A. V. Gurevich, L. V. Pariskaya, L. P. Pitaevsky, "Ion acceleration upon expansion of rarefied plasma", *Sov. Phys. JETP* **36**, 449 (1973).

[75] V. Yu. Bychenkov, V. N. Novikov, D. Batani, V. T. Tikhonchuk, S. G. Bochkarev, "Ion acceleration in expanding multispecies plasmas", *Phys. Plasmas* **11**, 3242 (2004).

[76] A. E. Kaplan, B. Y. Dubetsky, P. L. Shkolnikov, "Shock Shells in Coulomb Explosions of Nanoclusters", *Phys. Rev. Lett.* **91**, 143401 (2003).

[77] V. F. Kovalev, K. I. Popov, V. Yu. Bychenkov, and W. Rozmus, "Laser triggered Coulomb explosion of nanoscale symmetric targets", *Phys. Plasmas* **14**, 053103 (2007).

[78] S. C. Wilks, A. B. Langdon, T. E. Cowan, M. Roth, M. Singh, S. Hatchett, M. H. Key, D. Pennington, A. MacKinnon, and R. A. Snavely, "Energetic proton generation in ultra-intense lasersolid interactions", *Phys. Plasmas* **8**, 542 (2001).

[79] T. Zh. Esirkepov, S. V. Bulanov, K. Nishihara, T. Tajima, F. Pegoraro, V. S. Khoroshkov, K. Mima, H. Daido, Y. Kato, Y. Kitagawa, K. Nagai, and S. Sakabe, "Proposed Double-Layer Target for the Generation of High-Quality Laser-Accelerated Ion Beams", *Phys. Rev. Letters* **89**, 175003 (2002).

[80] C. Jungreuthmayer, L. Ramunno, J. Zanghellini, and T. Brabec, "Intense VUV laser cluster interaction in the strong coupling regime", *J. Phys. B At. Mol. Opt. Phys.* **38**, 3029 (2005).

[81] K. I. Popov, V. Yu. Bychenkov, W. Rozmus, V. F. Kovalev, and R. D. Sydora, "Mono-energetic ions from collisionless expansion of spherical multi-species clusters", *Laser and Part. Beams* **27**, 321 (2009).

[82] K. I. Popov, V. Yu. Bychenkov, I. A. Andriyash, R. D. Sydora, and W. Rozmus, "Expansion of two-ion-species spherical plasmas as a source of mono-energetic ions", *J. Plasma and Fus. Research* **8** (2009), in press.

[83] T. W. B. Kibble, "Mutual refraction of electrons and photons", *Phys. Rev.* **150**, 1060 (1966).

[84] E. S. Sarachik and G. T. Schappert, "Classical theory of the scattering of intense laser radiation by free electron", *Phys. Rev. D* **1**, 2738 (1970).

[85] J. X. Wang, W. Scheid, M. Hoelss, and Y. K. Ho, "Comment on 'Vacuum electron acceleration by coherent dipole radiation' ", *Phys. Rev. E* **65**, 028501 (2002).

[86] A. L. Troha and F. V. Hartemann, "Reply to "Comment on 'Vacuum electron acceleration by coherent dipole radiation' " ", *Phys. Rev. E* **65**, 028502 (2002).

[87] R. B. Palmer, "An introduction to acceleration mechanisms", SLAC-PUB-4320 (1987); in *Frontiers of Particle Beam*, edited by M. Month and S. Turner (Springer-Verlag, New York, 1988), pp. 607 – 635.

[88] T. Plettner, R. L. Byer, E. Colby, B. Cowan, C. M. S. Sears, J. E. Spencer, and R. H. Siemann, "Visible-Laser Acceleration of Relativis-

tic Electrons in a Semi-Infinite Vacuum", *Phys. Rev. Lett.* **95**, 134801 (2005).

[89] G. Malka, E. Lefebvre, and J. L. Miquel, "Experimental Observation of Electrons Accelerated in Vacuum to Relativistic Energies by a High-Intensity Laser", *Phys. Rev. Lett.* **78**, 3314 (1997).

[90] Kirk T. McDonald, "Comment on 'Experimental Observation of Electrons Accelerated in Vacuum to Relativistic Energies by a High-Intensity Laser' ", *Phys. Rev. Lett.* **80**, 1350 (1998).

[91] H. A. H. Boot and R. B. R.-S.-Harvie, "Charged particles in a non-uniform radio-frequency field", *Nature* **180**, 1187 (1957).

[92] D. Bauer, P. Mulser, and W.-H. Steeb, "Relativistic ponderomotive force, uphill acceleration and transition to chaos", *Phys. Rev. Lett.* **75**, 4622 (1995).

[93] M. Lax, W. Louisell, and W. McKnight, "From Maxwell to paraxial wave optics", *Phys. Rev. A* **11**, 1365 (1975).

[94] S. Masuda, M. Kando, H. Kotaki, and K. Nakajima, "Suppression of electron scattering by the longitudinal components of tightly focused laser fields", *Phys. Plasmas* **12**, 013102 (2005).

[95] J. L. Chaloupka and D. D. Meyerhofer, "Observation of Electron Trapping in an Intense Laser Beam", *Phys. Rev. Lett.* **83**, 4538 (1999).

[96] Q. M. Lu, Y. Cheng, Z. Z. Xu, S. Wang, "Electron acceleration by a laser pulse in vacuum", *Phys. Plasmas BC* **5**, 825 (1998).

[97] G. D. Tsakiris, C. Gahn and V. K. Tripathi, "Laser induced electron acceleration in the presence of static electric and magnetic fields in a plasma", *Phys. Plasmas* **7**, 3017 (2000).

[98] P. X. Wang, Y. K. Ho, X. Q. Yuan, Q. Kong, N. Cao, L. Shao, A. M. Sessler, E. Esarey, E. Moshkovich, Y. Nishida, N. Yugami, H. Ito, J. X. Wang, and S. Scheid, "Characteristics of laser-driven electron acceleration in vacuum", *J. Appl. Phys* **91**, 856 (2002).

[99] J. Pang, Y. K. Ho, X. Q. Yuan, N. Cao, Q. Kong, P. X. Wang, L. Shao, E. H. Esarey, and A. M. Sessler, "Subluminous phase velocity of a focused laser beam and vacuum laser acceleration", *Phys. Rev. E* **66**, 066501 (2002).

[100] Y. I. Salamin, G. R. Mocken, and C. H. Keitel, "Electron scattering and acceleration by a tightly focused laser beam", *Phys. Rev. STAB* **5**, 101301 (2002).

[101] L. W. Davis, "Theory of electromagnetic beams", *Phys. Rev. A* **19**, 1177 (1979).

[102] C. A. Brau, "Modern problems in classical electrodynamics" *Oxford university press* (2004), pp. 445 – 446.

[103] *Ibid.*, pp. 447 – 449.

[104] L. Cicchitelli, H. Hora, and R. Postle, "Longitudinal field components for laser beams in vacuum", *Phys. Rev. A* **41**, 3727 (1990).

[105] S. G. Bochkarev and V. Yu. Bychenkov, "Acceleration of electrons by tightly focused femtosecond laser pulses", *Quantum Electronics* **37**, 273 (2007).

[106] P. Varga and P. Török, "Focusing of electromagnetic waves by paraboloid mirrors. I. Theory", *J. Opt. Soc. Am. A* **17**, 2081 (2000).

[107] P. Varga and P. Török, "Focusing of electromagnetic waves by paraboloid mirrors. II. Numerical results", *J. Opt. Soc. Am. A* **17**, 2090 (2000).

[108] S.-W. Bahk, P. Rousseau, T. A. Planchon, V. Chvykov, G. Kalintchenko, A. Maksimchuk, G. A. Mourou, V. Yanovsky, "Characterization of focal field formed by a large numerical aperture paraboloidal mirror and generation of ultra-high intensity (10^{22} W/cm^2)", *Appl. Phys. B* **80**, 823 (2005).

[109] J. A. Stratton and L. J. Chu, "Diffraction theory of electromagnetic waves", *Phys. Rev.* **56**, 99 (1939).

[110] G. A. Korn, T. M. Korn, "Mathematical handbook for scientists and engineers", p. 17.3-3, McGraw-Hill book company (1968).

[111] D. J. Griffiths, "Introduction to electrodynamics", 3-rd edition, Prentice hall (1999), pp. 331 – 333.

[112] M. Abramowitz and I. A. Stegun (ed.), "Handbook of Mathematical Functions with Formulas, Graphs, and Mathematical Tables", 10th printing (Washington, D.C.: U.S. Dept. of Commerce, 1972), p. 896.

[113] D. V. Romanov, V. Yu. Bychenkov, W. Rozmus, C. E. Capjack, and R. Fedosejevs, "Self-Organization of a Plasma due to 3D Evolution of the Weibel Instability", *Phys. Rev. Lett.* **93**, 215004 (2004).

[114] *Ibid.* [110], p. 10.2-4.

[115] R. Hazeltine, F. Waelbroeck, "The framework of plasma physics" (Perseus book, Reading, Massachusetts, 1998), p. 175.

[116] K.S. Yee, "Numerical solution of initial boundary value problems involving Maxwell's equations in isotropic media", *IEEE Trans. Antennas Propag.* **AP-14**, 302 (1966).

[117] J. Boris, "Relativistic plasma simulation-optimizatioon of a hybrid code", in *Proceedings of the Fourth Conference on Numerical Simulation of Plasmas*, edited by J. P. Boris and R. A. Shanny (Naval Research Laboratory, Washington, D.C., 1970), pp. 367.

[118] C. Birdsall and A. Langdon, "Plasma Physics Via Computer Simulation" (McGraw-Hill, Inc., New York, 1985), pp. 356359.

[119] *Ibid.* pp. 308 – 310.

[120] V. A. Vshivkov, K. V. Vshivkov and G. I. Dudnikova, "Algorithms of solution of a problem of interaction between a laser pulse with a plasma", *Comp. Tech.* **6**, 47 (2001), *in Russian.*

[121] G. Mur, "Absorbing boundary conditions for the finite-difference approximation of the time-domain electromagnetic-field equations", *IEEE Trans. on Electr. Comp.* **EMC-23**, 377 (1981).

[122] A. Taflove, S. C. Hagnes, "Computational electrodynamics: the finite-difference time-domain method" (Artech House, 2000), pp. 194 – 224.

[123] N. Naumova, I. Sokolov, J. Nees, A. Maksimchuk, V. Yanovsky, and G. Mourou, "Attosecond Electron Bunches", *Phys. Rev. Lett.* **93**, 195003 (2004).

[124] Y.-Y. Ma, Y.-T. Li, X.-H. Yuan, M. Chen, H.-C. Wu, J. Zheng, and J. Zhang, "Dense quasi-monoenergetic attosecond electron bunches from

laser interaction with wire and slice targets", *Phys. Plasmas* **13**, 110702 (2006).

[125] Y. Tian, W. Yu, P. Lu, H. Xu, V. Senecha, A. Lei, B. Shen, and X. Wang, "Generation of periodic ultrashort electron bunches and strongly asymmetric ion Coulomb explosion in nanometer foils interacting with ultra-intense laser pulse ", *Phys. Plasmas* **15**, 053104 (2008).

[126] T. Ditmire, T. Donnelly, A. M. Rubenchik, R. W. Falcone, and M. D. Perry, "Interaction of intense laser pulses with atomic clusters", *Phys. Rev. A* **53**, 3379 (1995).

[127] I. Last and J. Jortner, "Electron and nuclear dynamics of molecular clusters in ultraintense laser fields", Parts I – IV, *J. Chem. Phys.* **120**, 1336; *J. Chem. Phys.* **121**, 1348, 3030, 8329 (2004).

[128] L. M. Wickens, J. E. Allen, and P. T. Rumsby, "Ion emission from the laser-produced plasmas with two electron temperatures", *Phys. Rev. Lett.* **41**, 243 (1978).

[129] B. Bezzerides, D. W. Forslund, and E. L. Lindman, "Existence of rarefaction shocks in a laser-plasma corona", *Phys. Fluids* **21**, 2179 (1978).

[130] L. M. Wickens and J. E. Allen, "Free expansion of a plasma with two electron temperatures", *J. Plasma Phys.* **22**, 167 (1979).

[131] P. Mora, R. Pellat, "Self-similar expansion of a plasma into vacuum", *Phys. Fluids* **22**, 2300 (1979).

[132] L. M. Wickens, J. E. Allen, "Ion emission from laser-produced, multi-ion species, two-electron temperature plasmas", *Phys. Fluids* **24**, 1894 (1981).

[133] M. A. True, J. R. Albritton, and E. A. Williams, "Fast ion production by suprathermal electrons in laser fusion plasmas", *Phys. Fluids* **24**, 1885 (1981).

[134] Ch. Sack, H. Schamel, "Nonlinear dynamics in expanding plasmas", *Phys. Lett.* **110A**, 206 (1985).

[135] Ch. Sack, H. Schamel, "Plasma expansion into vacuum – a hydrodynamic approach", *Phys. Reports* **156**, 311 (1987).

[136] M. K. Srivastava, B. K. Sinha, and S. V. Lawanda, "Ion front and ablation in a freely expanding two-ion, two-temperature, noncollisional plasma", *Phys. Fluids* **31**, 394 (1988).

[137] J. Denavit, "Collisionless plasma expansion into vacuum", *Phys. Fluids* **22**, 1384 (1979).

[138] J. E. Crow, P. L. Auer, J. E. Allen, "The expansion of a plasma into a vacuum", *J. Plasma Phys.* **14**, 65 (1975).

[139] Yu. I. Chutov, A. Yu. Kravchenko, "Expansion of a plasma bunch into vacuum", *Sov. J. Plasma Phys.* **6**, 151 (1980).

[140] P. Mora, "Plasma Expansion into a Vacuum", *Phys. Rev. Letters* **90**, 185002 (2003).

[141] M. Murakami and M. M. Basko, "Self-similar expansion of finite-size non-quasi-neutral plasmas into vacuum: Relation to the problem of ion acceleration", *Phis. Plasmas* **13**, 012105 (2006).

[142] G. Manfredi, S. Mola, and M. R. Feix, "Rescaling methods and plasma expansions into vacuum", *Phys. Fluids B* **5**, 388 (1993).

[143] D. S. Dorozhkina, V. E. Semenov, "Exact solution of vlasov equation for quasineutral expansion of plasma bunch into vacuum", *Phys. Rev. Letters* **81**, 2691 (1998).

[144] V. F. Kovalev, V. Yu. Bychenkov, and V. T. Tikhonchuk, "Particle dynamics during adiabatic expansion of a plasma bunch", *JETP* **95**, 226 (2002).

[145] V. F. Kovalev and V. Yu. Bychenkov, "Analytic solutions to the Vlasov equations for expanding plasmas", *Phys. Rev. Letters* **90**, 185004 (2003).

[146] V. F. Kovalev and V. Yu. Bychenkov, "Analytical models of laser-triggered ion acceleration", *Laser Phys.* **16**, 237 (2006).

[147] V. F. Kovalev and V. Yu. Bychenkov, "Kinetic description of the Coulomb explosion of a spherically symmetric cluster", *JETP* **101**, 212 (2005).

[148] M. Eloy, R. Azambuja, J. T. Mendonca, R. Bingham, "Interaction of ultrashort high-intensity laser pulses with atomic clusters", *Phys. Plasmas* **8**, 1084 (2001).

[149] K. Nishihara, H. Amitani, M. Murakami, S. V. Bulanov and T. Zh. Esirkepov, "High energy ions generated by laser driven Coulomb explosion of cluster", *Nucl. Instrum. Methods Phys. Res. A* **464**, 98 (2001).

[150] F. Peano, R. A. Fonseca, and L. O. Silva, "Dynamics and control of shock shells in the Coulomb explosion of very large deuterium clusters", *Phys. Rev. Lett.* **94**, 033401 (2005).

[151] F. Peano, R. A. Fonseca, J. L. Martins, and L. O. Silva, "Controlled shock shells and intracluster fusion reactions in the explosion of large clusters", *Phys. Rev. A* **73**, 053202 (2006).

[152] F. Peano, F. Peinetti, R. Mulas, G. Coppa, and L. O. Silva, "Kinetics of the collisionless expansion of spherical nanoplasmas", *Phys. Rev. Lett.* **96**, 175002 (2006).

[153] R. Decoste, B. H. Ripin, "High-energy ion expansion in laser-plasma interactions", *Phys. Rev. Lett.* **40**, 34 (1978).

[154] A. P. L. Robinson, A. R. Bell, and R. J. Kingham, "Effect of target composition on proton energy spectra in ultraintense laser-solid interactions", *Phys. Rev. Lett.* **96**, 035005 (2006).

[155] B. J. Albright, L. Yin, B. M. Hegelich, Kevin J. Bowers, T. J. T. Kwan, and J. C. Fernández, "Theory of laser acceleration of light-ion beams from interaction of ultrahigh-intensity lasers with layered targets", *Phys. Rev. Lett.* **97**, 115002 (2006).

[156] V. F. Kovalev, V. Yu. Bychenkov, and K. Mima, "Quasimonoenergetic ion bunches from exploding microstructured targets", *Phys. Plasmas* **14**, 103110 (2007).

[157] I. Last and J. Jortner, "Ultrafast high-energy dynamics of thin spherical shells of light ions in the Coulomb explosion of heteroclusters", *Phys. Rev. A* **71**, 063204 (2005).

[158] S. Ter-Avetisyan, M. Schnürer, P. V. Nickles, M. Kalashnikov, E. Risse, T. Sokollik, W. Sandner, A. Andreev, and V. Tikhonchuk, "Quasi-monoenergetic deuteron bursts produced by ultraintense laser pulses", *Phys. Rev. Lett.* **96**, 145006 (2006).

[159] A. V. Brantov, V. T. Tikhonchuk, O. Klimo, D. V. Romanov, S. Ter-Avetisyan, M. Schnürer, T. Sokolik, and P. V. Nickes, "Quasi-monoenergetic ion acceleration from a homogeneous composite target by an intense laser pulse", *Phys. Plasmas* **13**, 122705 (2006).

[160] I. Andriyash, V. Yu. Bychenkov, and V. F. Kovalev, "Coulomb explosion of a cluster with a complex ion composition", *JETP Lett.* **87**, 720 (2008).

[161] M. Murakami and M. Tanaka, "Nanocluster explosions and quasimonoenergetic spectra by homogeneously distributed impurity ions", *Phys. Plasmas*, **15**, 082702 (2008).

[162] F. Dorchies, F. Blasco, T. Caillaud, J. Stevefelt, C. Stenz, A. S. Boldarev, and V. A. Gasilov, "Spatial distribution of cluster size and density in supersonic jets as targets for intense laser pulses", *Phys. Rev. A* **68**, 023201 (2003).

[163] B. N. Breizman, A. V. Arefiev, and M. V. Fomytskyi, "Nonlinear physics of laser-irradiated microclusters", *Phys. Plasmas* **12**, 056706 (2005).

[164] *Ibid.* [102], pp. 208 – 213.

[165] F. F. Chen, "Introduction to plasma physics and controlled fusion, vol. 1, Plasma physics", second edition, Plenum press, New York (1984), pp. 305 – 307.

[166] E. A. Startsev and C. J. McKinstrie, "Multiple scale derivation of the relativistic ponderomotive force", *Phys. Rev. E* **55**, 7527 (1997).

[167] J. D. Huba, "NRL plasma formulary", NRL/PU/6790-02-450 (2002), p. 4.

[168] *Ibid.* [102], pp. 171 – 176.